SOLPS-ITER modelling of ASDEX Upgrade L-mode detachment

Haosheng WU

Supervisors
Prof. Roberto ZANINO
Prof. Fabio SUBBA

Doctoral Examination Committee:
Prof. A.B. , Referee, University of….
Prof. C.D. , Referee, University of…
Prof. E.F. , Referee, University of….
Prof. G.H. , Referee, University of…
Prof. I.J. , Referee, University of….

I hereby declare that, the contents and organisation of this dissertation constitute my own original work and does not compromise in any way the rights of third parties, including those relating to the security of personal data.

………………………………....
Haosheng WU
Turin, April 29, 2020

Summary

Recently, the ITER Organization started developing, distributing, and maintaining SOLPS-ITER as the state-of-the-art numerical tool for edge plasma modelling. In order to be confident about SOLPS-ITER prediction results about detachment for future tokamak devices e.g. the EU-DEMO and DTT, SOLPS-ITER modelling of ASDEX Upgrade L-mode detachment is performed.

We first examine the backward compatibility of SOLPS-ITER with SOLPS5.0 and produce a basic test of new physics/numerics improvements/additions in SOLPS-ITER without considering the effect of drifts. SOLPS-ITER simulation results match well SOLPS5.0 results. The remaining differences might be from the ion energy source. An upstream density scan, covering the full range from attached to detached conditions produces closely matching results (~10% differences). This suggests that the physics/numerics improvements/additions in SOLPS-ITER did not introduce unwanted effects.

Then, SOLPS-ITER modelling results of three detachment states (the onset of detachment, the fluctuating detachment state and the complete detachment state) of ASDEX Upgrade are validated against experimental data including electron density n_e and electron temperature T_e profiles at outer mid-plane, particle flux Γ_{ion} and electron temperature T_e profiles at inner and outer targets, electron density in inner divertor volume and neutral flux density at dome and pump locations. Modelling results show that the discrepancies of particle flux Γ_{ion} in previous SOLPS5.0 study at inner target are reduced [63]. However, the discrepancies of particle flux Γ_{ion} at outer target in the onset of detachment and fluctuating detachment state still exist. For the complete detachment state, SOLPS-ITER modelling results match well with experimental data. In the future, the modelling of ASDEX Upgrade impurity seeding L-mode discharge will be studied.

Acknowledgment

In the past four years, I am very grateful to everyone who has helped me.

First, I would like to express my warmest heartiest and deepest gratitude to Prof. Roberto Zanino and Prof. Fabio Subba, who are my supervisors. Prof. Zanino gave me the opportunity to study at Politecnico di Torino, guided my research and help me not only in my study but also in my life. I remember the first time of our discussion, he taught me that "Before you begin to model, you must have an expectation about your results, otherwise you will lost and forget what you are doing." This sentence always guides me in my whole Phd life. Prof. Subba, I don't know how can I express my gratitude to him. When I met problems about research, he always asked me to sit behind him and then taught me how to solve hand by hand, not a solution but a method. When he reviewed my papers and thesis, he always examined word for word. When I met problems in life, he always consoled and help me. It is a great luck for me to meet my supervisors.

Second, I want to express my heartfelt thanks to Dr. Marco Wischmeier, for his help not only in study but also in living during my visit at Max-Planck-Institut für Plasmaphysik, Garching, Germany. Every time when I asked him questions, he always guided me step be step until I got the correct answer. Without his support, I could not have finishd my thesis.

I would like to thank Pan Ou, Ferdinand Hitzler and everyone in PBP group in IPP, Garching, David Coster and Xavier Bonnin for their useful discussion, especially about drifts modelling. I would like to thank Roberto Bonifetto, Antonio Froio, Mattia Cagnoli, Giuseppe Francesco Nallo, Andrea Zappatore and everyone in NEMO group for their help in my life. I would like to thank my friend Tiger, Mengmeng Liu and all of my friends for their accompany that make my Ph.D life full of happiness.

Finally, my thanks would go to my father and mother for their support during my twelve years' study.

Contents

List of Tables

List of Figures

Chapter 1

Introduction

1.1 Nuclear fusion and Tokamak

Since humankind entered into the time of the Industrial Revolution, the utilization of energy changed dramatically. From steam engine to nuclear power plant, the way of taking advantage of energy has promoted the development of our society. The potentially most effective way to fundamentally solve energy problem is nuclear fusion energy due to the ultimate fuel which is abundant in the sea water. Nuclear fusion [1] is a nuclear reaction in which two or more atomic nucleis combine to form one or more different atomic nucleis and subatomic particles (neutrons or protons), in the reaction process, a huge energy is released as kinetic energy of produced particles. The nuclear fusion reactions related to the hydrogenic isotopes (hydrogen, deuterium and tritium) are the following:

$$D + T \rightarrow \ _{2}^{4}He + n + 17.6 \ \text{MeV} \tag{1.1}$$

$$D + D \rightarrow T + \ _{1}^{1}H + 4.0 \ \text{MeV} \tag{1.2}$$

$$D + D \rightarrow \ _{2}^{3}He + n + 3.3 \ \text{MeV} \tag{1.3}$$

$$D + \ _{2}^{3}He \rightarrow \ _{2}^{4}He + \ _{1}^{1}H + 18.3 \ \text{MeV} \tag{1.4}$$
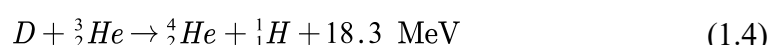
The reaction rates for hydrogenic isotopes of nuclear fusion reactions are in Figure 1.1. The DT reaction, equation (1.1), is the easiest fusion reaction to obtain and is selected for future nuclear fusion reactors. Tritium does not exist in nature but can be produced through neutrons impact on Lithium particles, the producing process is called Tritium breeding.

$$_{3}^{7}Li + n \rightarrow \ _{2}^{4}He + T + n - 2.5 \ \text{MeV} \tag{1.5}$$

$$_{3}^{6}Li + n \rightarrow \ _{2}^{4}He + T + 4.8 \ \text{MeV} \tag{1.6}$$
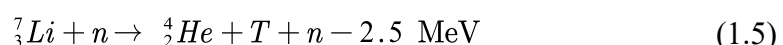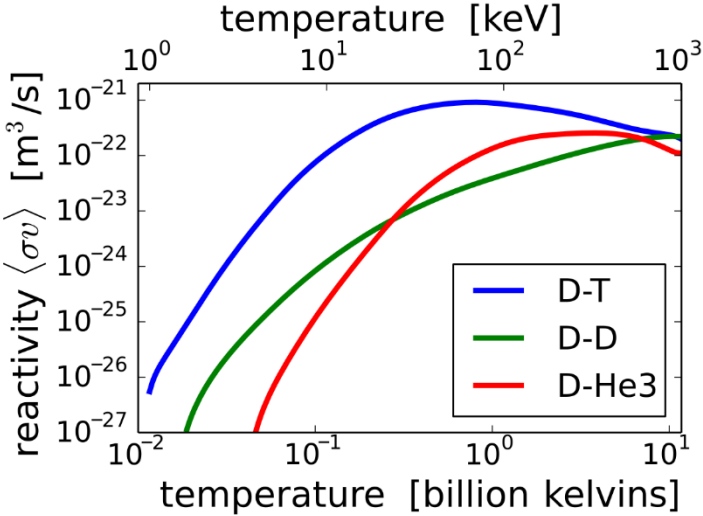
Figure 1.1 Nuclear reaction rates of hydrogenic isotopes [2].

Nuclear fusion reactions require nucleis close to each other enough ($< 10^{-15}$ m). Thus, high temperature (at least ~10keV) is required to overcome their Coulomb potential. At such high temperature, the particles constitute "plasma"[3], which is the fourth state of matter like solid, liquid and gas. Thus, plasma is the research objective in this study. Considering power loss, in order to ignite nuclear fusion DT reaction, the Lawson criterion [4]:

$$nT\tau_E > 3 \times 10^{21} \ \mathrm{m^{-3} keVs} \tag{1.7}$$

should be satisfied, where n is plasma density, T is plasma temperature and τ_E is energy confinement time.

There are two ways to realize nuclear fusion reaction under laboratory conditions: Inertial Confinement Fusion (ICF) and Magnetic Confinement Fusion (MCF). The basic idea of ICF is using laser to create high pressure and high temperature that decreases the volume of fuel in a tiny time that increases the density of the fuel to meet the Lawson criterion. For MCF, the main idea is using magnetic field to confine hot plasma, which has a high temperature, so that the nuclear fusion reaction can happen.

Until now, for all types of MCF devices, Tokamak, whose name is from a Russian word "Токамáк", is the most promising device to realise commercial application of nuclear fusion energy. The schematic diagram of Tokamak is shown in Figure 1.2. The toroidal magnetic field $\vec{B}_\Phi$ is created by the toroidal field coils, the poloidal filed $\vec{B}_\theta$ is provided by the toroidal plasma current. The total magnetic field $\vec{B}$ is helical. The main components of a Tokamak device are magnetic coils, vacuum vessel, heating systems, divertor, diagnostic systems. The high temperature plasma is confined by magnetic field in the vacuum vessel.

For a tokamak device, the safety factor q [5] is defined as:

$$q \approx \frac{rB_{\Phi}}{RB_{\theta}} \qquad (1.8)$$

where R is the major radius and r is the minor radius of the torus. Pitch angle is defined as $\theta_{pitch} \approx \frac{B_{\theta}}{B_{\phi}} \approx \frac{B_{\theta}}{B_{total}}$, the typical value is about 0.1 in tokamak devices. For tokamak design, the safety factor $q \geqslant 2$ is to ensure the stability of confined plasma [6].
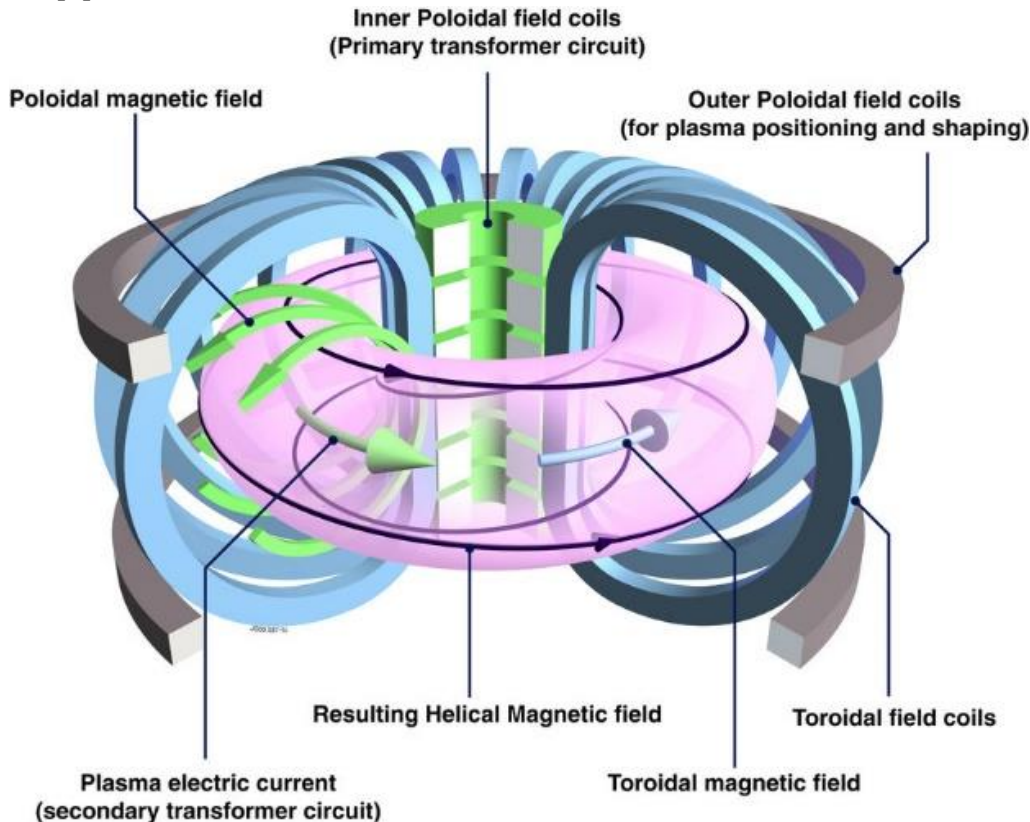
Figure 1.2 Schematic diagram of a Tokamak device. Source: Eurofusion.

Existing main Tokamak devices for nuclear fusion research are: ASDEX Upgrade (AUG) [7] in Germany, Joint European Tours (JET) [8] in United Kingdom, TCV [9] in Switzerland, DIII-D [10] in America, JT-60SA [11] in Japan, EAST [12] and HL-2M [13] in China. There are also future Tokamak devices under design or construction: ITER [14] in France, CFETR [15] in China, DTT [16] in Italy and the EU-DEMO [17].

1.2 Scrape-Off Layer and Divertor configuration

In a tokamak device, toroidal plasma can directly contact with the first wall of vacuum vessel. The high temperature plasma can corrode, even melt, the materials of the vacuum vessel that results in the production of impurities, e.g. Carbon or Tungsten. When the DT reaction happens, the impurity of Helium is produced. If the impurities are not removed from the core plasma, the tokamak device can not

discharge normally. In order to solve this problem, the limiter and divertor configurations are proposed which are shown in Figure 1.3.
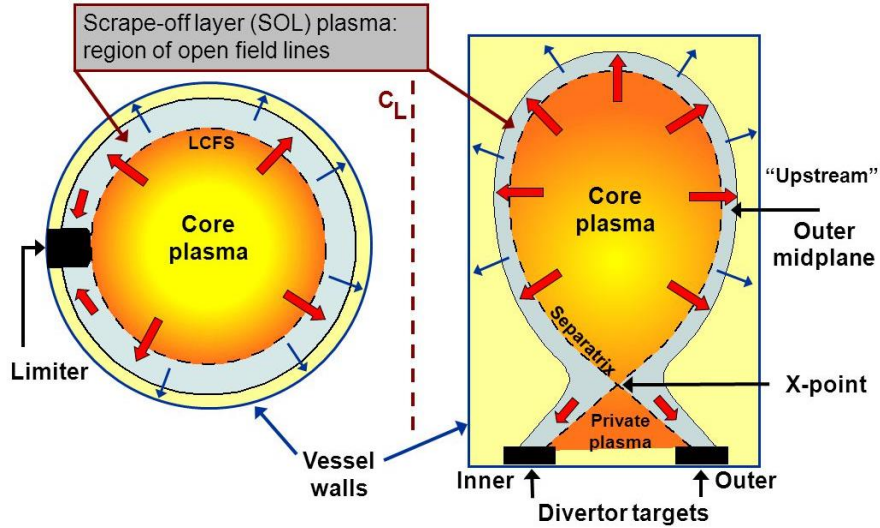
Figure 1.3 Limiter and divertor configurations [18].

The limiter is defined as a material structure inserted into the plasma. Then the plasma is conventionally divided into two regions: the core plasma and the Scrape-Off Layer (SOL) plasma. The edge of the limiter defines the Last Closed Flux Surface (LCFS). In the core plasma region, the magnetic field lines do not contct with any material structure. The region where the magnetic field lines are open is called "Scrape-Off Layer" (SOL). The parallel transport of the plasma along magnetic field line is stronger than the perpendicular (cross-field) transport. The high temperature plasma is directly contact only with the limiter material surfaces. Instead, the vessel walls avoid contact with high temperature matter.

The divertor configuration is obtained by adding an additional toroidal current. The additional poloidal magnetic field combining with the one produced by the plasma current creates a poloidal-field null point, called X-point. This surface across the X-point is called separatrix. There is still the SOL region in divertor configuration similar to the limiter configuration. The ASDEX Upgrade tokamak divertor is shown in Figure 1.4.
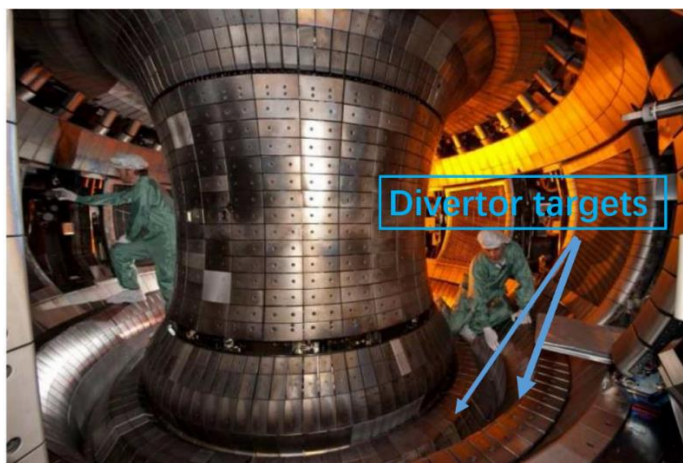
Figure 1.4 The divertor of ASDEX Upgrade. Source: IPP.

In divertor configuration, the contact area between plasma and divertor targets is far from the core plasma. Impurities transport along open magnetic field lines in the SOL towards the divertor targets and do not pollute (ideally) the core plasma. Heat and particle fluxes deposit only onto the divertor targets. This helps improving energy confinement and pumping efficiency.

There are several confinement modes in tokamak discharges. Two typical confinement modes are: the low-confinement mode (L-mode) and the high-confinement mode (H-mode). Figure 1.5 shows the plasma pressure profiles along minor radius and the corresponding confinement modes. The low pressure profiles is corresponding to the L-mode. H-mode is observed in experiments [20] when the heating power increases above a threshold. Typically, in H-mode, an Edge Transport Barrier (ETB) develops, which increases the stored energy of plasma [21][22]. The transition from L-mode to H-mode is unclear now. In this study, we focus on ASDEX Upgrade L-mode discharges.
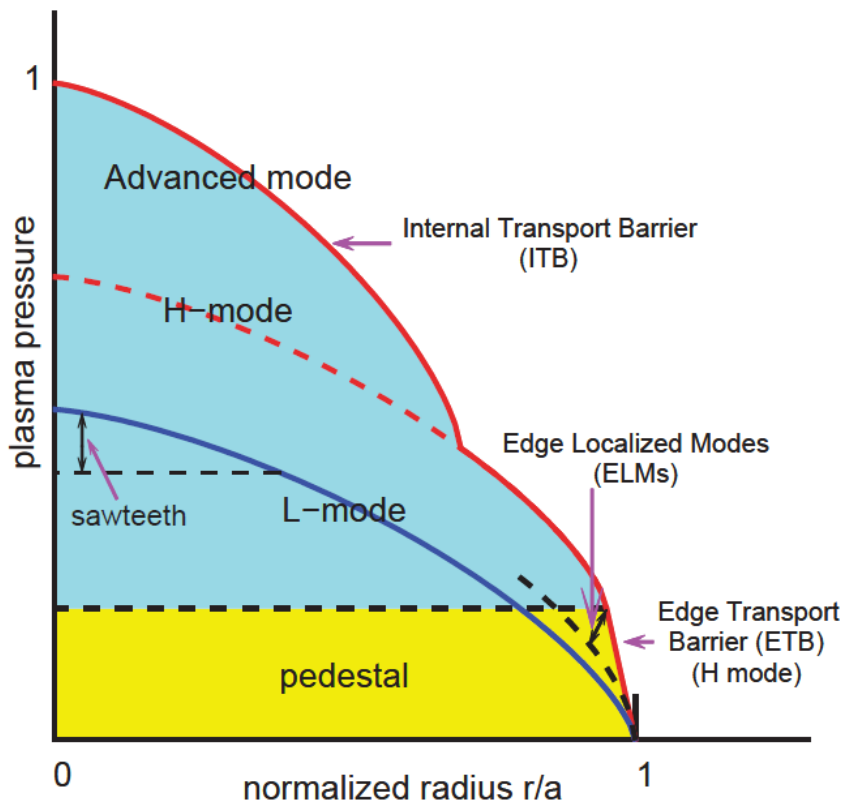
Figure 1.5 Plasma pressure profiles along minor radius with the corresponding confinement modes. Source: CEA.

1.3 Aim & Outline

Divertor controls the exhaust of heat and of helium ashes, and protects the core plasma from impurity contamination. From an engineering point of view, there is a limit of a few MW/m^2 on the peak value of steady-state heat load on divertor targets [23][24][25]. Thus, heat load on divertor targets becomes a critical issue for tokamak reactor-grade devices. In order to decrease the heat load of divertor targets, detachment operation regime (introduced in section 2.3.3) is proposed for future

tokamak devices, e.g. ITER, CFETR and the EU-DEMO. In order to confidently predict detachment and explore possible scenarios to decrease the heat load on divertor targets for future tokamak devices, the physical models which are widely used in boundary plasma numerical modelling tool, SOLPS-ITER (see chapter 4), need to be validated against current experimental data, e.g. ASDEX Upgrade. The main aim of this thesis is to validate SOLPS-ITER modelling results of detachment against ASDEX Upgrade L-mode detachment discharges.

In this chapter, research background is briefly introduced including nuclear fusion, tokamak and divertor. In chapter 2, basic physical processes related to plasma transport in SOL are introduced. The basic theoretical model, Two-point model (TPM) and divertor operation regimes are also described. Recent study about ASDEX Upgrade detachment is summarized. In chapter 3, basic theories of plasma diagnostic systems which provide experimental data for the validation of SOLPS-ITER modelling results, are introduced. In chapter 4, a detailed description of the SOLPS-ITER code is presented, including the fluid plasma solver B2.5 and the Monte Carlo transport code EIRENE, which is used for neutral transport. In chapter 5, a numerical comparison between SOLPS-ITER and SOLPS5.0, which has been used for edge plasma modelling more than twenty years in the past, is presented. In chapter 6, SOLPS-ITER modelling results about ASDEX Upgrade L-mode detachment are presented. The effect of boundary conditions, drifts and radial convective velocity are discussed. Conclusions and perspectives are given in chapter 7.

Chapter 2

Boundary Plasma Physics

2.1 Basic aspects of boundary plasma

In this chapter, basic aspects of boundary plasma physics, which are relevant for boundary plasma modelling, are introduced. When plasma enters the SOL region, various types of volumetric processes can happen that are described in section 2.1.1. Section 2.1.2 discusses the Debye sheath formation in front of solid surfaces. Furthermore, when plasma and neutral particles strike on solid surfaces, several plasma-wall interactions should be considered, which are introduced in section 2.1.3.

2.1.1 Volumetric processes

In SOL region, ions, electrons and neutrals co-exist. Thus, different types of atomic reactions can happen. The most important ones are ionization, recombination and charge exchange. For example, hydrogenic recombination (radiative and three body), charge exchange and ionisation reaction rates versus temperature are shown in Figure 2.1.
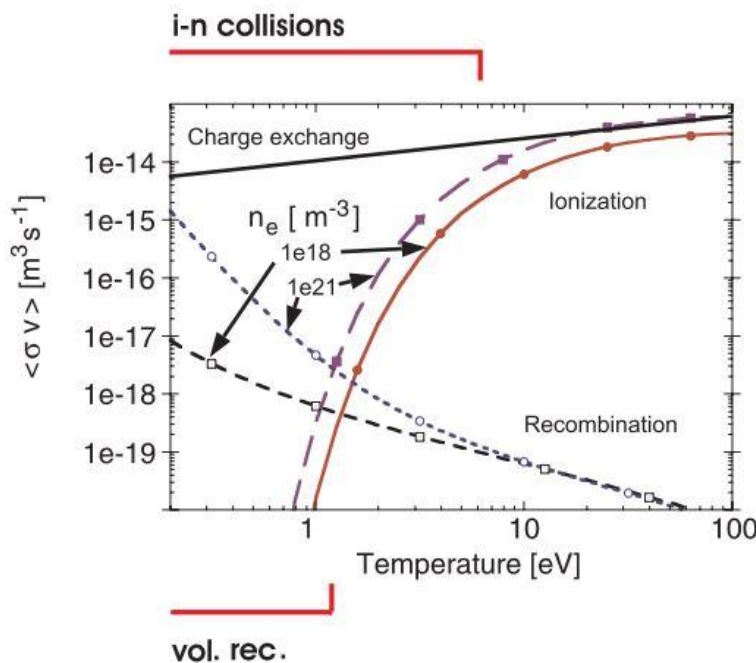
Figure 2.1 Reaction rates for hydrogenic recombination (radiative and three body), charge exchange and ionisation rates as a function of temperature and density [27].

Ionization rates decrese strongly when the temperature falls below 10 eV. At higher temperature, ionization constitutes an ion source and plasma energy sink in the SOL region. The recombination rates decrease as the temperautre increases. Below 2 eV, recombination rates are larger than ionization. Recombination in the SOL region play as a particle sink. When the temperature is about ~5 eV, charge exhange rate coefficients are, at least, one magnitude higher than ionization and recombiation. The charge exchange is a momentum sink because of the friction between neutrals and ions. For impurity ions, e.g. Carbon, Neon, Argon etc., bremsstrahlung emission and line radiation have to be considered as power loss [6].

2.1.2 Debye sheath

Plasma can be treated as quasi-neutral when space scales is larger than the Debye length λ_D:

$$\lambda_D = \left(\frac{\varepsilon_0 k T_e}{e^2 n_e}\right)^{\frac{1}{2}} \tag{2.1}$$

For typical boundary plasma in a tokamak device, $\lambda_D \approx 10^{-5}$ m [6]. Any single particle potential is shielded within a few Debye lengths. Figure 2.2 shows the main phenomenon when plasma (ions and electrons) reach a solid surface. At the interface between plasma and solid, the Debye sheath is formed and the quasi-neutrality of plasma does not hold anymore ($n_i > n_e$) in the sheath region. The length of Debye sheath is of a few Debye lengths. In the sheath region in front of the target, there is a potential drop ($\sim 3k\dfrac{T_e}{e}$ eV) that acclerates positive charged ions and repells negetively charged electrons. At the entrance of Magnetic Pre-sheath, according to the Bohm-Chordura criterion [26], the ion velocity v_{ion} is:

$$v_{ion} \geqslant c_s = \left(\frac{T_e + T_i}{m_i}\right)^{\frac{1}{2}} \tag{2.2}$$

where c_s is the plasma sound speed, T_e is the electron temperature, T_i is the ion temperature and m_i is the ion mass. The heat flux at the sheath entrance is:

$$q_{\parallel,se} = \gamma T \Gamma_{\parallel,se} = \gamma n T c_s \tag{2.3}$$

where γ is the sheath heat transmission factor, usually is assumed to be 8 [6][32].
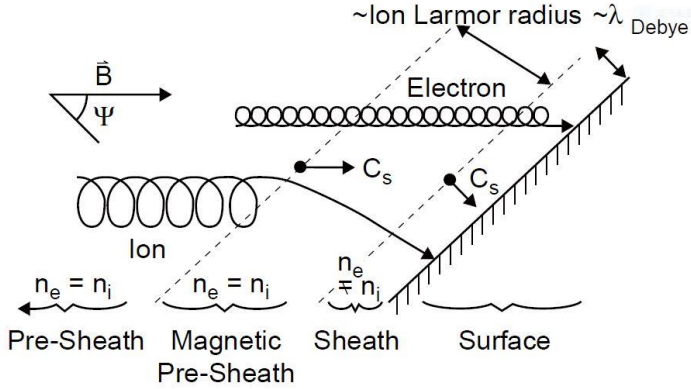
Figure 2.2 The structure of the sheath in front of a target surface with an oblique magnetic field and its influence on electron and ion trajectories is shown [26].

2.1.3 Plasma wall interaction

When ions or atoms strike a solid surface, one of the following processes may occurs [6]:

- particles back-scatter or reflect with some fraction of the impacting energy.
- particles fall into the solid material, subsequently released as thermal ions with velocity which is dependent on the solid surface temperature.
- Particles are trapped into the solid material.

The reflection process is described by particle and energy reflection coefficients R_N and R_E [29].

$$R_N(E_0) = \frac{N}{N_0} \tag{2.4}$$

$$R_E(E_0) = \frac{\overline{E}(E_0)N}{E_0 N_0} = \frac{\overline{E}(E_0)}{E_0} R_N(E) \tag{2.5}$$

where N is the number of reflected particles, N_0 is the total number of impacting particles, E_0 is the impact energy, and $\overline{E}(E_0)$ is the average energy of refected particles. Plasma particles are neutralized in the solid surface, and then released as neutrals. The relased neutral particles are re-ionized in the SOL region. This process is called recycling [5].

The impacting particles can induce electrons emitting from the solid surface. Another consequence is the sputtering includes physical sputtering and chemical sputtering. A basics feature [30] of physical sputtering is that the momentum is transferred from impacting particles to the atoms of surface materials. When the transferred energy exceeds the binding energy of surface atoms, the surface atoms leave the surface. In contrast to physical sputtering, chemical sputtering is a

chemical reaction that happens between the impacting particles and surface materials, for example, the production of CH_4 in tokamak devices [31].

2.2 Two-point model [6]

Two-point model (TPM) describes plasma transport in the SOL region between two extreme points, as shown in Figure 2.3. The TPM can be thought as straightening the SOL region along the magnetic field between an upstream and a target locations:

- Upstream, which is called 'u' for short. It can be anywhere above X-point in a single null divertor configuration. Parallel gradients of plasma parameters in that region are small. Thus, upstream can be approximately any point between two targets. Usually, the upstream is taken to be the outer mid-plane.
- Target, which is called 't' for short. It means the divertor targets.
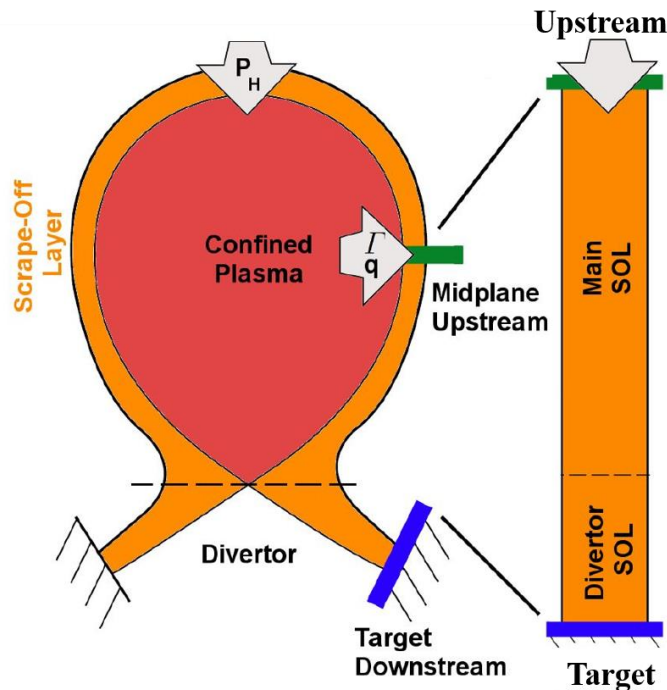
Figure 2.3 A schmetic view of Two-point model and SOL transport [32].

TPM is derived from one-dimensional fluid equations. Considering conservation equations, particle conservation equation is:

$$\frac{d}{dx}(nv) = S_{particle} \tag{2.6}$$

Momentum conservation equation is:

$$\frac{d}{dx}(p_e + p_i + m_i n v^2) = S_{mom} \tag{2.7}$$

Energy conservation equation is:

$$\frac{d}{dx}\left[q_{\parallel,cond} + \frac{5}{2}\Gamma_{\parallel}(T_e + T_i) + \frac{1}{2}nm_iv^3\right] = S_{energy} \tag{2.8}$$

where n is the plasma density, v is the plasma velocity, $S_{particle}$ is the particle source, p_e and p_i are the electron and ion static pressure, S_{mom} is the momentum source, $q_{\parallel,cond}$ is the parallel conduction heat flux, $\Gamma_\parallel$ is the parallel particle flux, T_e and T_i are the electron and ion temperatures, S_{energy} is the energy source.

There are some assumptions. For particle conservation, the recycling neutral particles near divertor target are re-ionized immediately. The particle flux only exists between recycling region and target. Without considering recombination, the only sink for plasma is the divertor target. There is no perpendicular transport and reversed flux. At upstream, plasma velocity is zero and increases up to the sound speed at the sheath entrance.

For momentum conservation, the basic TPM neglects both friction and viscosity. Volumetric processes are also not considered. There is no momentum loss along flux tube, so that $P_{static} + P_{dynamic} = nk(T_e + T_i) + nm_i v^2 = constant$. It is also assumed that the electron temperature equals the ion temperatures.

For energy conservation: there is no convection but only conduction from upstream to target. There is no radiation loss and Joule heating during the transport process.

With above assumptions and conservation equations, TPM are:

$$n_u T_u = 2n_t T_t \tag{2.9}$$

$$T_u^{\frac{7}{2}} = T_t^{\frac{7}{2}} + \frac{7}{2}\frac{1}{\kappa_{0e}}q_\parallel L_\parallel \tag{2.10}$$

$$q_\parallel = \gamma n_t T_t c_s \tag{2.11}$$

From (2.9) (2.10) and (2.11) are the TPM, where $L_\parallel$ is parallel connection length from upstream to target. Upstream density n_u and parallel heat flux $q_\parallel$ are treated as 'input', the unknown parameter n_t, T_t, T_u are treated as 'output'.

$$T_u \approx \left(\frac{7}{2}\frac{1}{\kappa_{0e}}q_\parallel^{\frac{2}{7}} L_\parallel^{\frac{2}{7}}\right) \propto q_\parallel^{\frac{2}{7}} L_\parallel^{\frac{2}{7}}$$

$$T_t = \frac{m_i}{2e}\frac{4q_\parallel^2\left(\frac{7}{2}\frac{q_\parallel L}{\kappa_{0e}}\right)^{-\frac{4}{7}}}{\gamma^2 e^2 n_u^2} \propto n_u^{-2}q_\parallel^{\frac{10}{7}} L_\parallel^{-\frac{4}{7}}$$

$$n_t = \frac{n_u^3}{q_\parallel^2}\left(\frac{7}{2}\frac{q_\parallel L}{\kappa_{0e}}\right)^{\frac{6}{7}}\frac{\gamma^2 e^3}{4m_i} \propto n_u^3 q_\parallel^{-\frac{8}{7}} L_\parallel^{\frac{6}{7}} \tag{2.12}$$

$$\Gamma_t = \frac{n_u^2}{q_\parallel}\left(\frac{7}{2}\frac{q_\parallel L}{\kappa_{0e}}\right)^{\frac{4}{7}}\frac{\gamma e^2}{2m_i} \propto n_u^2 q_\parallel^{-\frac{3}{7}} L_\parallel^{\frac{4}{7}}$$

It can been seen that the upstream temperature T_u is independent on the upstream density n_u, and not sensitive to the heat flux $q_\parallel$ due to the exponent factor of 2/7. Increasing the heat flux $q_\parallel$ results in the increase of T_t. Increasing the upstream density n_u can decrease the target temperature T_t.

In order to consider volumetric power loss, momentum loss and the convection transport of parallel heat flux, the extended-TPM [6] is introduced, which can qualitative estimate the effect of radiation and volumetric atomic processes.

The volumetric power loss is described with a power loss factor f_{power}:

$$(1 - f_{power})q_{\parallel} = q_t \qquad (2.13)$$

For a momentum loss factor f_{mom}:

$$p_t = \frac{1}{2} f_{mom} p_u \qquad (2.14)$$

For a convection transport factor f_{cond}:

$$q_{\parallel,cond} = f_{cond} q_{\parallel}$$
$$q_{\parallel,conv} = (1 - f_{cond}) q_{\parallel} \qquad (2.15)$$

Then extended-TPM is:

$$T_u \propto f_{cond}^{\frac{2}{7}}$$

$$T_t \propto \frac{(1 - f_{power})^2}{f_{mom}^2 f_{cond}^{\frac{4}{7}}}$$

$$\frac{T_u}{T_t} \propto \frac{f_{cond}^{\frac{6}{7}} f_{mom}^2}{(1 - f_{power})^2}$$

$$n_t \propto \frac{f_{mom}^3 f_{cond}^{\frac{6}{7}}}{(1 - f_{power})^2}$$

$$\Gamma_t \propto \frac{f_{mom}^2 f_{cond}^{\frac{4}{7}}}{1 - f_{power}} \qquad (2.16)$$

Applications of the TPM and extended-TPM for analysing divertor operation regime are introduced in next section.

2.3 Divertor operation regime

There are three divertor operation regimes: sheath-limited regime (or low recycling regime), conduction-limited regime (or high recycling regime), and detachment as shown in Figure 2.4. In the three different divertor regimes, the relationship between upstream and target plasma parameters are different.
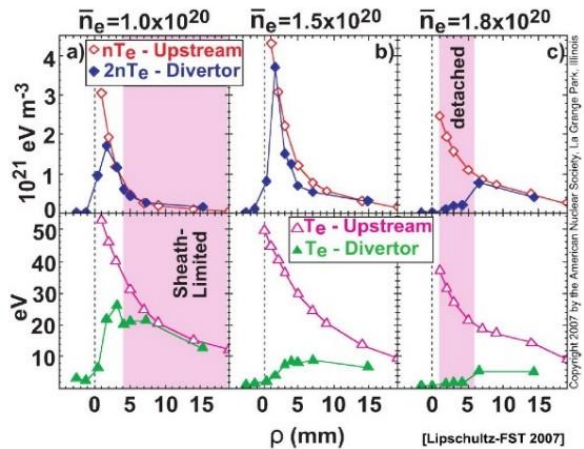
Figure 2.4 Divertor operation regimes including sheath-limited regime, conduction limited regime and detachment [33].

2.3.1 Sheath-limited regime

In low density discharge, the plasma collisionality $\nu^* = \dfrac{L}{\lambda}$, where L is the conection legth and λ is self-collisionality lengths, is low (<10). Plasma in SOL region is in the sheath-limited regime. Along the flux tube, the temperature gradient is small that $T_u \approx T_t$, only conductive heat flux is presented. The ion velocity is almost zero at upstream. Ions are accelerated to the plasma sound speed at the sheath entrance. The heat flux is limited only by the heat transmission of the sheath at divertor target. According to equation (2.9), the target density $n_t = \dfrac{1}{2} n_u$ which means as the upstream density increases, the target density will linearly increase. For the target heat flux $q_t = q_{\parallel} = \gamma n_t T_t c_s$. Increasing the power entering the SOL region, the consequent high heat flux to the divertor target will lead to the damage of divertor target. Thus, there is no interest for the sheath-limited regime in current tokamak devices.

2.3.2 Conduction-limited regime

As the upstream density n_u increases, the collisionality ν^* is also increased. Divertor moves from the sheath-limited to the conduction-limited regime. Recycling neutrals are ionized near the target. The temperature gradient along magnetic field line is noticeable. The target temperature T_t is lower than the upstream temperature T_u. Heat flux is mainly conductive. The total pressure is constant along a given flux tube, as in the sheath-limited regime. The TPM, equation (2.12), describes the conduction-limited regime well [6].

2.3.3 Detachment

When the divertor is in conduction-limited regime, keeping on increasing the the upstream density, a roll-over of particle flux at divertor targets is observed called detachment as shown in Figure 2.4 and Figure 2.5.

In the detachment, the electron temperature at target T_t is about 1~2 eV. From what we discussed in section 2.1.1, recombination near target is dominant. There is a pressure drop along magnetic field lines, since momentum loss mechanisms are active. The target pressure p_t is much lower than the upstream pressure p_u. The momentum loss can be explained by friction and charge-exchange due to ion-neutral collision, plasma recombination which results in the escape of neutrals, and cross-field transport [32]. In the detachment, the heat flux at target is strongly reduced. It should be noticed here that in this study, only the particle detachment is focused on, and power detachment is not considered [32].

The basic TPM is not accurate enough to describe detachment; the extended-TPM is better. The momentum loss factor f_{mom} and the power loss factor f_{power} depend on volumetric processes which are determined by plasma parameters (n_e and T_e). When the target temperature is above 2 eV, we do not consider momentum loss, and combining equations (2.3) and (2.16) gives the qualitative relation of the heat flux at target

$$q_t \propto (1 - f_{power}) \qquad (2.17)$$

which means the target heat flux can be reduced by volumetric radiation processes. In experiments, for H-mode discharges, the impurity seeding is used to radiate most of power [14][32] . When the temperature is below 2eV, without considering the power loss, the particle flux is decreased due to the increase of momentum loss.

The roll-over of particle flux at divertor targets is observed in JET, DIII-D, ASDEX Upgrade [33][34][35]. In detachment, strong asymmetry of particle fluxes between inner and outer targets is observed [35]. In experiments, an effective way to measure the degree of detachment (DOD) [36] is using a ratio between particle flux from the TPM and measured particle flux at divertor targets.

$$\text{DOD} = \frac{\Gamma_{TPM}}{\Gamma_{\exp}} = c \frac{\overline{n}_e^2}{\Gamma_{\exp}} \qquad (2.18)$$
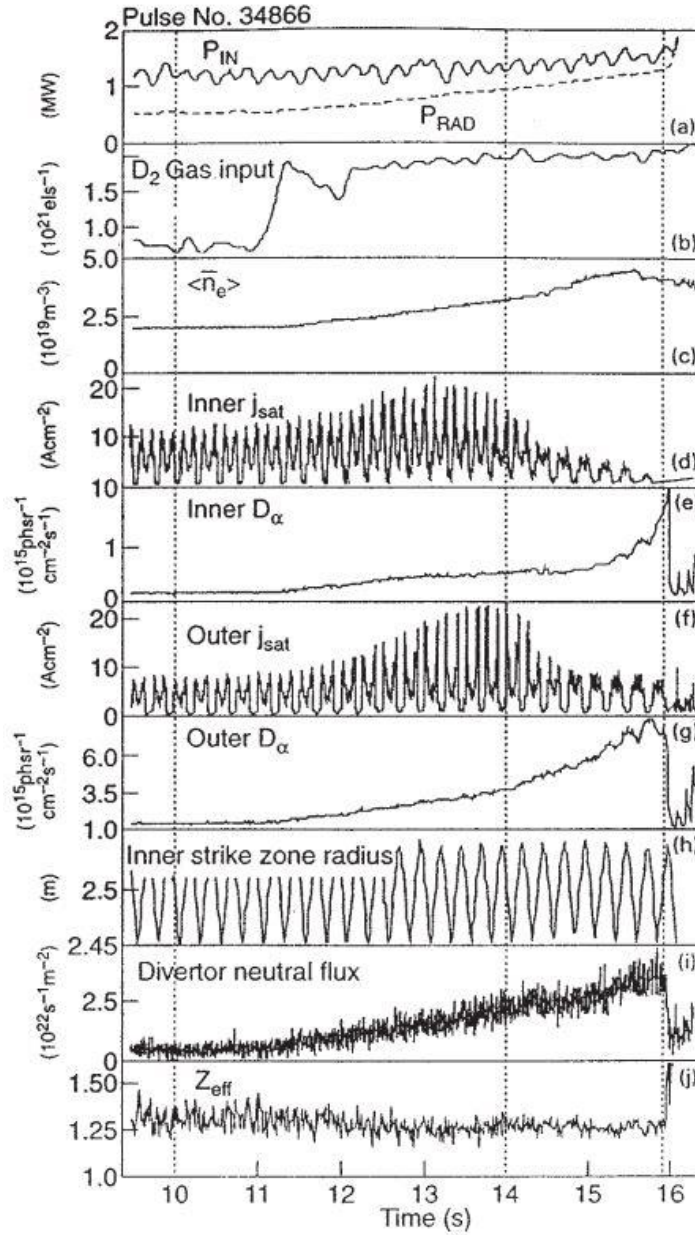
Figure 2.5 Experimental observation of detachment in JET [34] .

2.4 Divertor detachment states

2.4.1 Classification of divertor detachment states [35]

In recent study of ASDEX Upgrade L-mode density ramp discharges, a new classification of divertor detachment states is proposed. The detachment is not a continuously evolving process but rather undergoes three distinct states: the onset of detachment state (OS), the fluctuating detachment state (FS), the complete detachment state (CDS). This classification is observed with different heating power, forward and reversed magnetic field, and hydrogen and deuterium fuelling. The classification of three detachment states for deuterium fuelling discharge #27100 is shown in Figure 2.6.
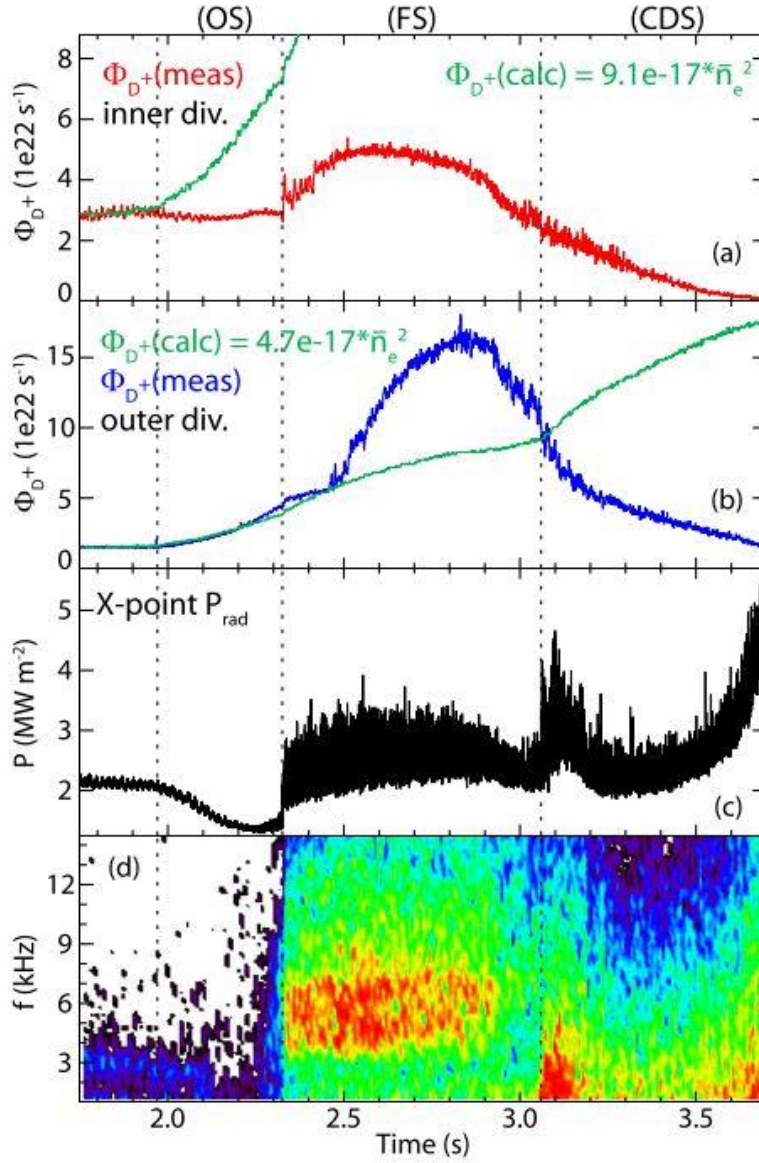
Figure 2.6 Characteristic of three detachment states for #27100: onset of detachment state (OS), the fluctuating detachment state (FS) and the complete detachment state (CDS) [35].

The onset of detachment: the first deviation of integrated particle flux from TPM model scaling at inner target occurs when the measured ion flux Φ_{D+}^{meas} at inner target become less than ion flux Φ_{D+}^{calc} from the TPM calculation. At this phase, partially detached from the strike point at the inner divertor target happens. While the outer divertor is still attached and in the conduction-limited regime. The measured ion flux Φ_{D+}^{meas} at the outer divertor target is still consistent with the value calculated from the TPM.

The fluctuating detachment state: fluctuating radiation, originating close to the X-point, appears in the fluctuating detachment state. From Figure 2.6, it can been seen that a fluctuation band suddenly appeared. In the fluctuating state, in the inner divertor volume, the electron density n_e is an order of magnitude higher than the

electron density at divertor targets and the line averaged electron density $\bar{\bar{n}}_e$, which is called the High Field Side High Density (HFSHD) region. Radiation is directly proportional to the square of electron density, thus the total radiation distribution can be used to estimate the position of the HFSHD region, as shown in Figure 2.7. In the fluctuating detachment state, the roll-over of particle flux at the inner and outer divertor targets happens.
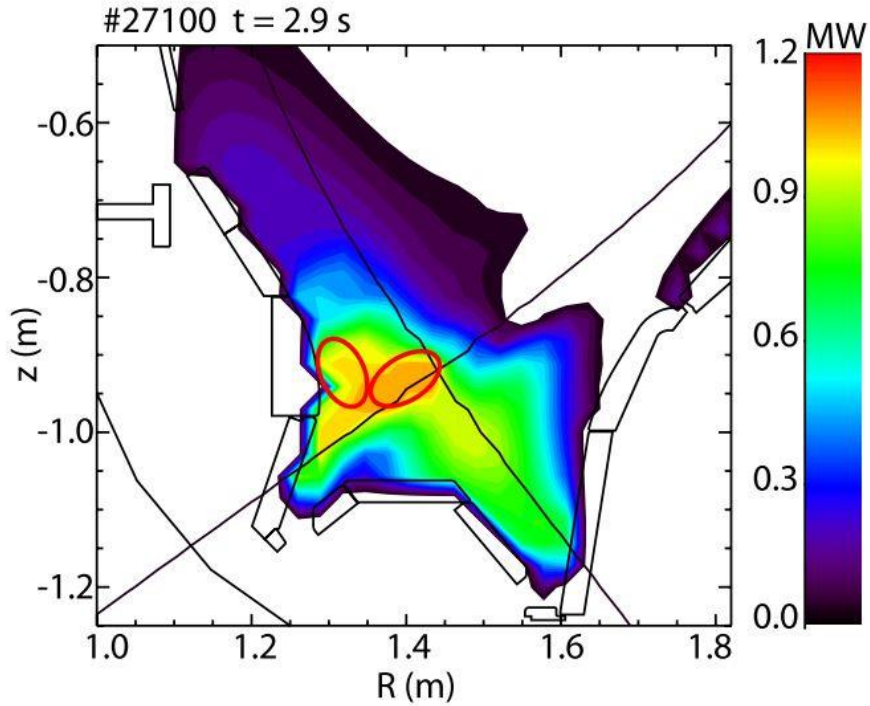
Figure 2.7 Estimated position the HFHDS region in fluctuating detachment state through radiation distribution for #27100 [35].

The complete detachment state: the fluctuation of radiation near X-point disappears. In the complete detachment state, the HFSHD region moves along magnetic field line to above the X-point (see Figure 2.8). When transiting from the fluctuating detachment state to the complete detachment state, the ion flux at the outer target begin to be lower than the TPM scaling.
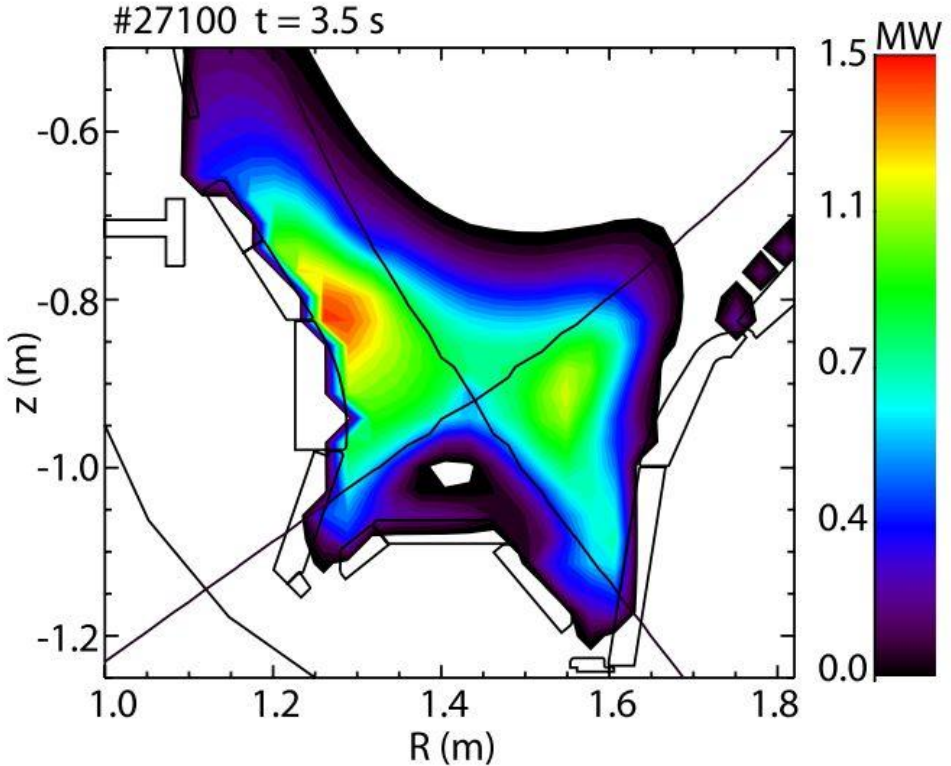
Figure 2.8 Estimated position the HFHDS region in complete detachment state through radiation distribution for #27100 [35].

Similar to L-mode discharge, the processes of detachment in H-mode discharge are classified in four phases: the onset of detachment, the fluctuating detachment state, partial detachment of outer target and the complete detachment state [37].

2.4.2 The High Field Side High Density region

The High Field Side High Density (HFSHD) is a region (often localized in the inner divertor in forward magnetic field) where the electron density is an order magnitude higher than electron density at targets and line averaged electron density $\bar{n}_e$. Measured electron density comes from Stark broadening of spectroscopic Balmer lines [38]. In both ASDEX Upgrade and JET, the HFSHD region is observed, and is independent on machine size and confinement mode [39]. In the complete detachment state, the HFSHD region extends towards the far SOL region, i.e. about 10 times of heat decay length away from the separatrix and 20cm above the X-point in the complete detachment state of ASDEX upgrade [40]. The formation of the HFSHD region increases the neutral leakage in the high field side that increases the neutral flux at high field side. Detailed power scan shows that the electron density and neutral flux at high field side increases linearly with heating power [42].

The dynamics of the HFSHD front in ASDEX Upgrade is illustrated in Figure 2.9 [40]: entering the fluctuating detachment state, the ionization front moves towards upstream to reduce the ionization radiation that balances the increased recombination radiation [41]. The recombination zone is near the strike point of the

inner divertor target. The divertor nose constitutes an obstacle for the perpendicular neutral flux from the target to the region above the X-point. Passing into this shadow the neutral flux above the X-point is strongly reduced, the ionization front fades away and the heat flux from upstream can increase the temperature in the recombination region, subsequently reducing recombination and reforming an ionization front below the X-point. A cycle reformation of the ionization front propagating from below to above the X-point occurs leading to a fluctuation as observed in the experiment.
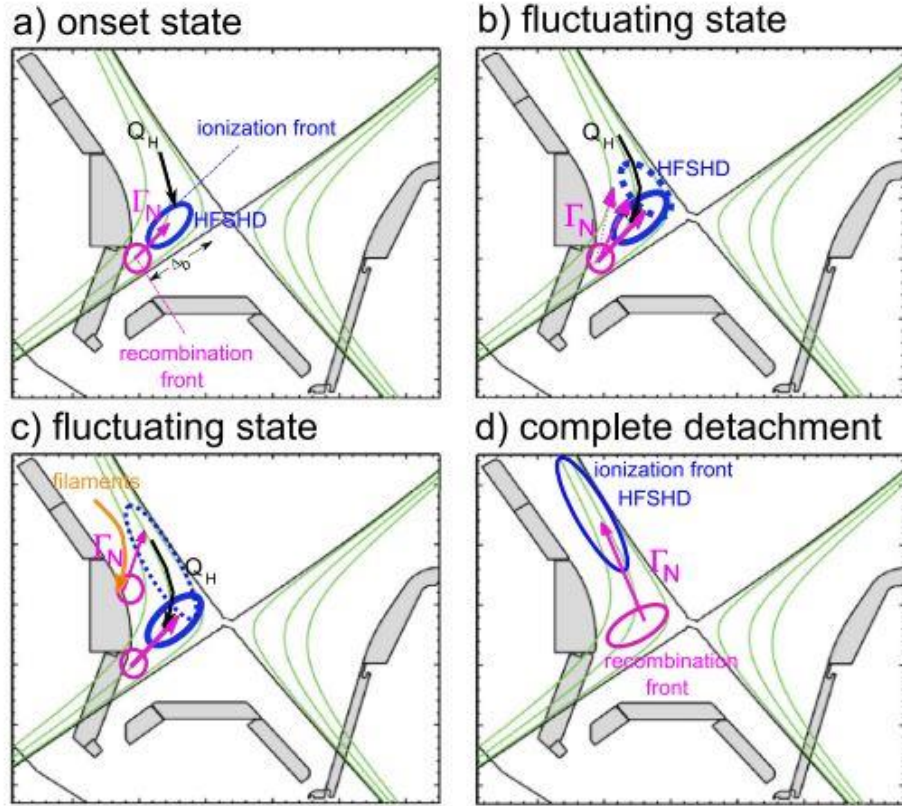
Figure 2.9 Schematic of dynamics of the HFSHD front [40].

The TPM and extended-TPM can not identify the complicate volumetric processes occurring during detachment states. In order to simulate the three detachment states, a more accurate two dimensional numerical tool named SOLPS-ITER is used. A detailed intrudction of SOLPS-ITER is in chapter 4.

2.5 Perpendicualr transport

In TPM, only the parallel transport which is along magnetic field line is considered. The transport perpendicular to the magnetic filed is neglected, beacuse parallel transport is much stronger than perpendicular transport. In this section, we briefly introduce the transport perpendicular to the magnetic field line. An empirical description of perpendicular transport in radial direction in tokamak is

$$\Gamma_r = - D_\perp \frac{\partial n}{\partial r} + v_r n \tag{2.19}$$

where Γ_r is the perpendicular particle flux in radial direction, $D_\perp$ is the diffusive transport coefficient, v_r is the convective velocity in radial direction and n is the particle density. The main idea of equation (2.19) is that the perpendicular transport in radial direction has two parts: one is due to particle diffusion and another is convection. In the practice of boundary plasma modelling, the radial particle flux is usually described by an effective diffusion coefficient: $\Gamma_r = - D_\perp^{(eff)} \frac{\partial n}{\partial r}$. An empirical diffusive coefficient derived from experiments is [43]

$$D_\perp^{(eff)} = D_\perp^{Bohm} = \frac{0.06 T_e}{B} \tag{2.20}$$

For ASDEX Upgrade L-mode discharges, in the upstream of the SOL region, where $T_e \approx 50\,\mathrm{eV}$, $B \approx 2.5\,\mathrm{T}$, the perpendicular transport coefficient $D_\perp^{Bohm}$ is about 1.2 m^2/s which is much larger than the value given by theory [44]. Experiments of Alcator C-Mode discharges show that in order to keep the perpendicular particle flux, with diffusion-only assumption, the perpendicular transport coefficient should be increased sharply along radial direction in the SOL region [45].

Intermittent transport in SOL region is observed in experiments [46][47][48], which is convection origin. In the far SOL region, turbulence propagates radially in the form of so-called filaments aligned to the magnetic filed lines or blobs [49]. In ASDEX Upgrade L-mode discharges, the filament transport characteristics are measured[49][50][51] including auto-correlation time, detection frequency, density flucuation and radial propagation velocity. At the transition from the sheath-limited to the high recycling regime, an increase of blob amplitude and corresponding transport is observed [51]. For boundary plasma modelling, through the telegraph equation, an effective perpendicular diffusion coefficient including both diffusion and intermittent transport can be derived [53].

Chapter 3

Experimental diagnostic

In ASDEX Upgrade tokamak, there are serval diagnostic systems to measure plasma parameters. In this chapter, experimental diagnostic systems related to boundary plasma, whose measurments are used to validate SOLPS-ITER modelling results in chapter 6, are briefly introduced.

3.1 Thomson Scattering

Thomson scattering (TS) diagnostic [101] uses Nd:YAG laser to measure electron density and electron temperature profiles. The electron density and temperature are calculated from the spectrum of laser light which is scattered by electrons and leads to a spectral broadening due to Doppler effect. The electron temperature is measured from the amplitude of the broadening, and the electron density is measured from the intensity of spectrum.

In ASDEX Upgrade, lasers shot vertically from the bottom to measure the core and boundary plasma parameter profiles as shown in Figure 3.1. 16 (11) spatial channels with 4 spectral channels each are used for measuring core and edge radial profiles of the electron density and temperature. Clusters of 4 and 6 Nd-YAG lasers with pulse energies of 1J and pulse durations of 15 ns in each are used for the core and edge system. The laser clusters penetrate either through the E port (core plasma), or through the D port (edge plasma on the low field side of the tokamak). The repetition rate for each laser is 20 Hz [103].
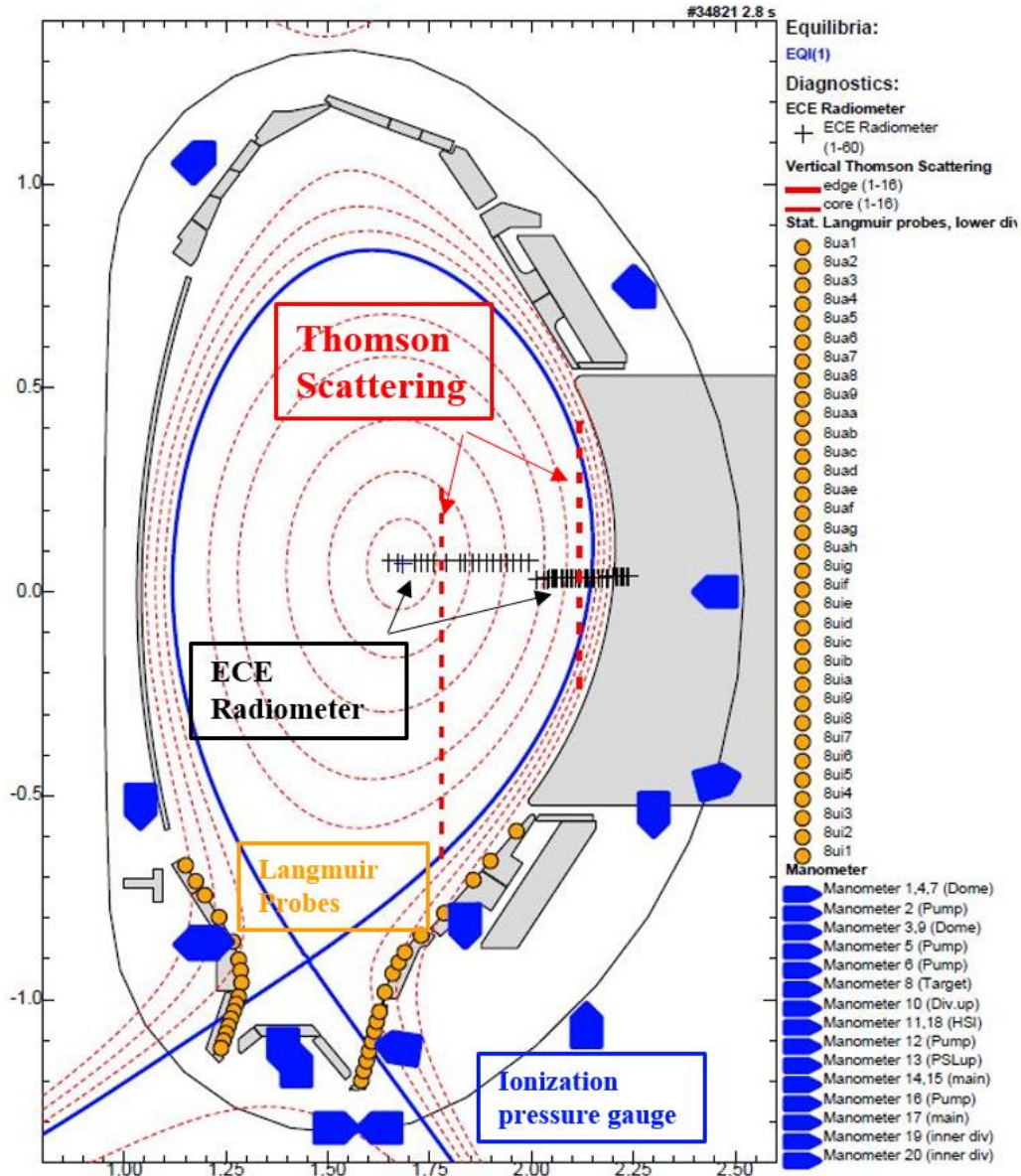
Figure 3.1 Related diagnostic systems in the ASDEX Upgrade.

3.2 Electron Cyclotron Emission Radiometer

Electron cyclotron emission radiometer (ECE) diagnostic [102][104] is used for measuring electron temperature from radiometry of electron cyclotron emission. Hot electrons gyrate around field lines with cyclotron frequency $\omega = \dfrac{eB}{m}$, where ω is the angular velocity, B is the magnetic field, and m is the electron mass. At the second harmonic of the electron cyclotron frequency, the plasma usually emits like a blackbody source. Therefore, the electron temperature can be derived from the absolute intensity of the second harmonic X mode emission if the plasma is optically thick, in which case the Rayleigh-Jeans law of thermal emission holds. Since the magnetic field (and consequently the emission frequency $f = 2\pi\omega$)

depends on the radius, the power spectrum represents a radial electron temperature profile. At present, only the heterodyne radiometer in ASDEX Upgrade provides electron temperature profiles regularly [103].

In ASDEX Upgrade, Integrated Data Analysis (IDA) within the framework of Bayesian probability theory are applied to the combined analysis of Lithium beam emission spectroscopy (LIB), deuterium cyanide laser interferometry, Electron Cyclotron Emission (ECE), and Thomson scattering spectroscopy [105][106]. The four heterogeneous diagnostics enable a simultaneous estimation of electron density and temperature profiles with high spatial and temporal resolution. The coherent IDA analysis of the profile diagnostics allows one to consider diagnostic interdependencies correlating density and temperature profiles [106]. The IDA measurements of electron density and electron temperature profiles at outer mid-plane are used in chapter 6.

3.3 Langmuir Probes

In ASDEX Upgrade, flush mounted Langmuir probes are implemented to measure the plasma parameters in front of divertor targets. A Langmuir probe is essentially a pin collecting electron and ion currents that are used to estimate electron density n_e, electron temperature T_e and plasma potential V_p using Voltage-Current characteristic curve.

The principle of a Langmuir probe is shown in Figure 3.2. When a metal probe penetrates into the plasma, electrons reach the surface of the probe at a rate which is much larger than ions. This results in a negative potential at the probe surface, which attracts positive ions and repels negative electrons. Adjusting the potential of probe through an additional voltage, when the current is zero, the floating potential V_{fl} is measured. At large negative voltage, the saturated current

$$I_{sat} = A_{probe}\, j_{sat} = n_e A_{probe}\, ec_s \tag{3.1}$$

is used to calculated the electron density. Reducing the negative voltage, the electron temperature is calculated from the slope of the Voltage-Current characteristic curve:

$$T_e = \frac{e(V_{probe} - V_{fl})}{kB}\left[\ln\left(1 + \frac{I_{probe}}{I_{sat}}\right)\right]^{-1} \tag{3.2}$$
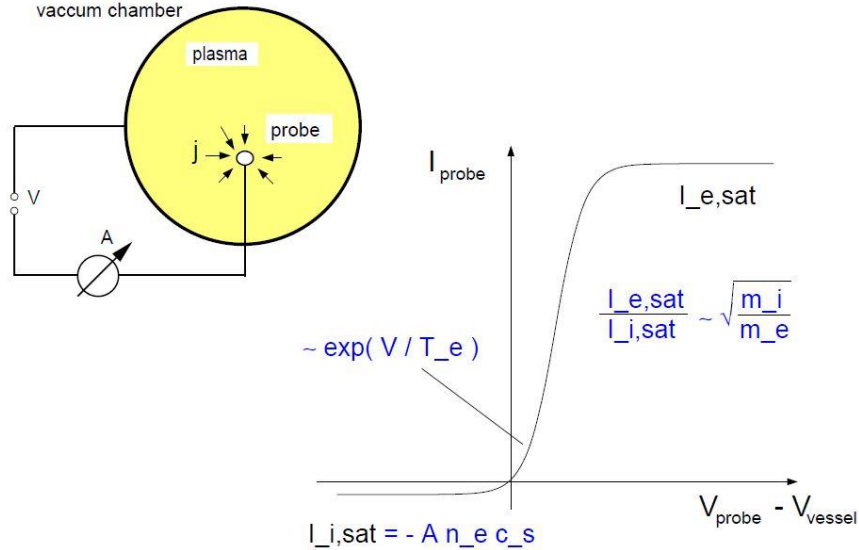
Figure 3.2 Principle of a single Langmuir probe measurement [107].

In addition to single Langmuir probe, there are double Langmuir probe and triple Langmuir probe. A double Langmuir probe works closed to floating potential that electron density and electron temperature are derived directly from the Voltage-Current characteristic curve. A triple Langmuir probe consists of a single probe for floating potential and a double probe for voltage and saturated current. There are three types of Langmuir probe construction scheme to face different heat loads: fast moving probe, heat sink probe and flush mounted probe [107]. The fixed Langmuir probes in the lower divertor of ASDEX Upgrade are flush mounted probe. The reliable measured electron temperature range is from 2~25 eV. In chapter 6, ion flux and electron temperature are measured by flush mounted triple Langmuir probe.

3.4 Divertor Spectroscopy

Volume electron density is determined by divertor spectroscopy, which is based on the spectroscopic measurement of the Stark broadening of the Balmer lines [38]. The spectral Balmer lines are broadened when the surrounding plasma emits atoms. The Stark broadening effect is proportional to the surrounding plasma density. Thus, the surrounding plasma density can be deduced from the broadening of Balmer lines. Stark broadening effect is a combination of pressure broadening due to Coulomb collisions (collision damping) and Stark split due to the electric field produced by surrounding plasma. The measured Balmer lines are fitted to theoretic profiles of Stark broadened Balmer line to give the corresponding volume electron density.

The line-of-sight (LOS) of divertor spectroscopy for #27100 discharge is shown in Figure 3.3 which includes RIV, ZIV, ZON and RXV groups. The measured volume electron density is corresponded to the region where the Balmer line emissivity is highest. The measured volume electron density is not an average value but is close to the maximum density along LOS [108]. The uncertainty of

divertor spectroscopy is about 15% and the lower limit for divertor spectroscopy measurement is $n_e \approx 4.0 \times 10^{19} \, \text{m}^{-3}$.
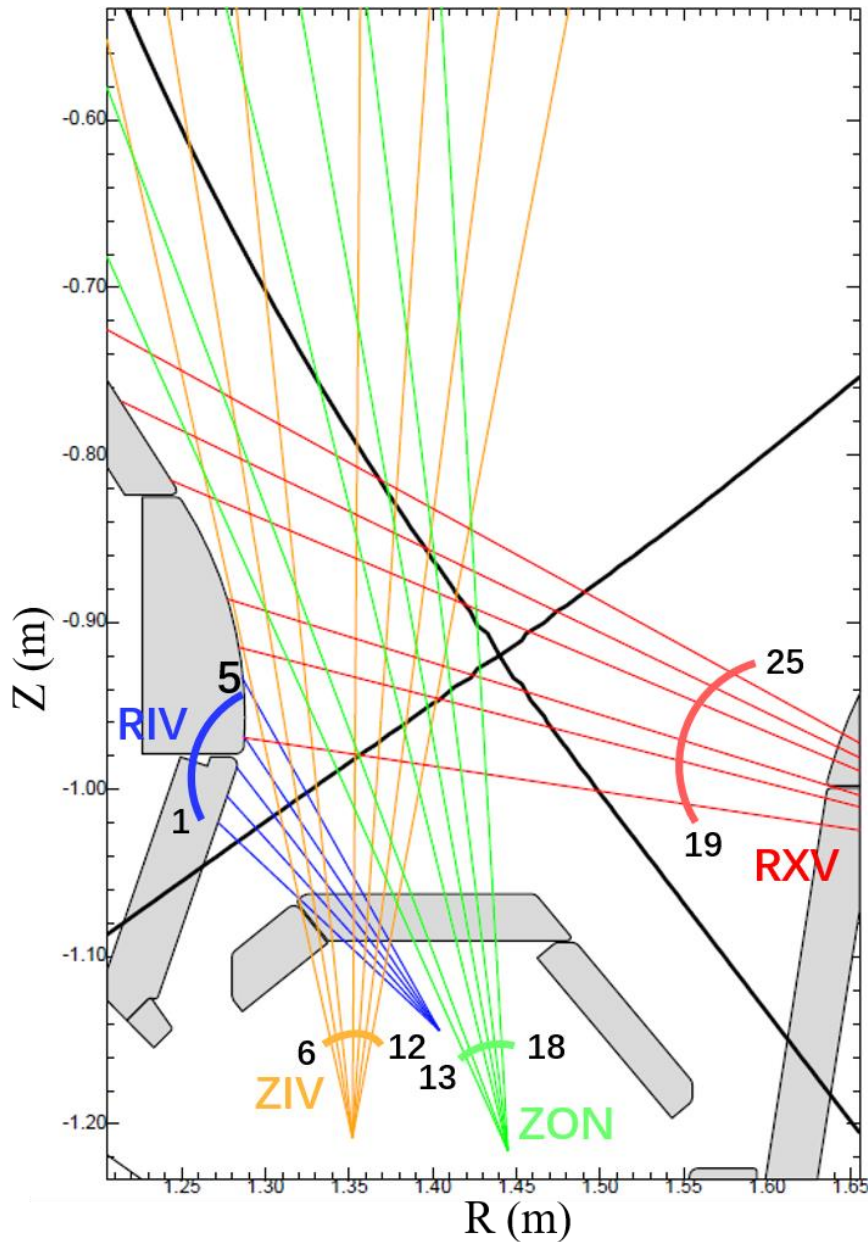
Figure 3.3 LOS of divertor spectroscopy for #27100. RIV, ZIV, ZON and RXV are differnt groups of divertor spectroscopy.

3.5 Ionization Pressure Gauge

Ionization pressure gauges measure neutral particle flux densities in the vacuum vessel of ASDEX Upgrade. Neutral particles enter the gauges and then are ionized by electron impact and the induced ion currents are measured [109][110]. The locations of gauges in ASDEX Upgrade are shown in Figure 3.1. Neutral flux density measurements are not only important for the control operation of tokamak devices, but also fundamental for the understanding of the plasma–wall interaction and its influence on the plasma performance. For example, the neutral compression

pressure ratio between dome and pump decides pumping efficiency, which is important for the removal of impurity. Moreover, the neutral flux density on the high field side is associated with the HFSHD region [42]. In section 6.2.1, the modelling results of neutral flux densities at dome and pump locations are validated against experimental measurements.

Chapter 5

Numerical Tool

4.1 SOLPS-ITER

4.1.1 Development process of SOLPS

Plasma transport in the SOL region is complicated, because both parallel transport along magnetic field line and perpendicular transport (due to the gradient of density and filament dynamics) exist. The TPM is not accurate enough to describe the physical characteristics of plasma transport, especially the divertor detachment. Thus, more comprehensive physical models are needed. SOLPS code package (Scrape-Off Layer Plasma Simulation) is widely used for boundary plasma modelling. It includes a fluid plasma solver B2/B2.5 [54][55][56] and a Monte Carlo code EIRENE [57] for neutral particle transport.

The SOLPS code package has grown from the coupling of B2/B2.5 and EIRENE. Historically, since the two main components are maintained and developed by different teams, various 'weddings' took place between the two families, leading to a multiplicity of SOLPS versions that results in multiple parallel existing branches [58]. Summary of various SOLPS and corresponding B2/B2.5 and various EIRENE are in Table 4.1 [59].

Table 4.1 Summary of various SOLPS versions and corresponding B2/B2.5 and EIRENE.

	EIRENE96	EIRENE99	EIRENE_facelift	EIRENE_2010
B2	SOLPS4.0		SOLPS4.2	SOLPS4.3
B2.5 + drifts	SOLPS5.0		SOLPS5.1	
B2.5+improved drifts model	SOLPS5.2			SOLPS-ITER

In order to model helium pumping and impurity penetration, the original B2 which is a multi-spcies plasma fluid code was developed and applied to ASDEX tokamak [54]. Considering the electric field, currents and drifts in the SOL region, B2.5 is developed by Max-Planck-Institut für Plasmaphysik (IPP) [55][56]. Compared to EIRENE96, EIRENE99 contains a collisional radiative model for atomic and molecular ionization, recombination and dissociation rate coefficients, improved treatment of molecular vibrationally excited states [60]. SOLPS5.0 with EIRENE99 were widely used for ASDEX Upgrade modelling in the past twenty years [61][62][63][64]. SOLPS4.2, in which neutral-neutral collisions and line radiation are implemented in EIRENE_facelift, was applied to ITER and JET

modelling [65][66]. SOLPS4.3, which is based on EIRENE_2010 was applied to ITER design [67][68].

In 2015, the ITER Organization has started developing, distributing, and maintaining SOLPS-ITER as the state-of-the-art numerical tool for edge plasma modelling [69][70]. Compared to SOLPS5.0, which was widely used for ASDEX Upgrade modelling, SOLPS-ITER includes not only SOLPS5.0 physics but also a large number of new physics/numerics improvements/additions, which are recommended to SOLPS-ITER users. The most important feature about fluid plasma is the new treatment of drifts and currents, based on SOLPS5.2 [71][72].

Workflow of SOLPS-ITER is shown in Figure 4.1. DivGeo is a GUI that helps user to create and manipulate comuputational grids. Uinp creates input paramters for EIRENE including geometry paramters, atomic reactions and reflection models etc. b2ah, b2ai and b2ar set default physical parameters, initial plasma paramters and atomic rates for fluid plasma. b2mn is the main program that provides final numerical solution. b2pl is a post-processing tool for plotting. More details are in the EIRENE user manual [57] and the SOLPS-ITER user maual [93].
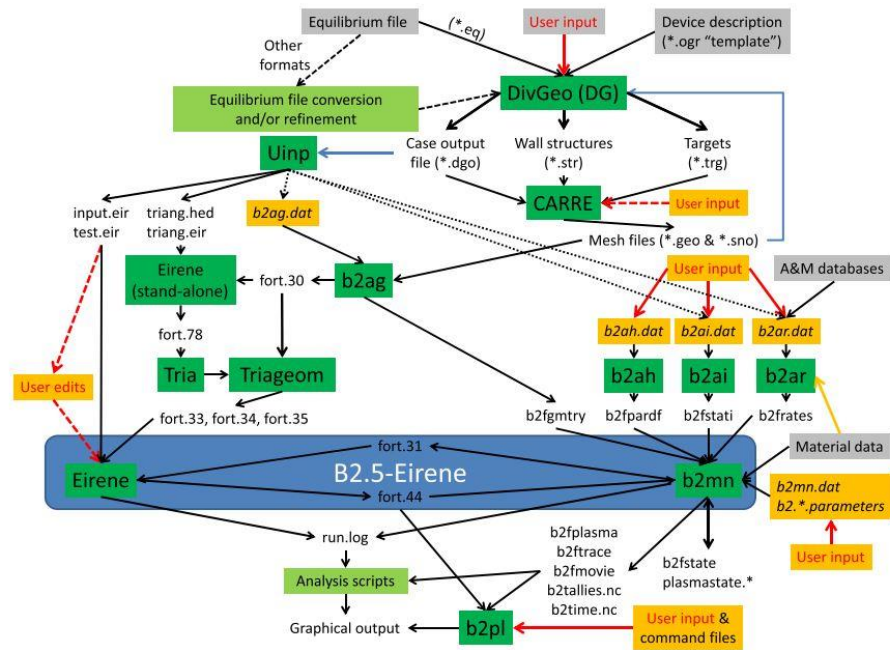
Figure 4.1 SOLPS-ITER workflow [70].

4.1.2 State of the art

In the past twenty years, SOLPS5.0 has been widely used for ASDEX Upgrade modelling research. The state of research about SOLPS5.0 modelling of ASDEX Upgrade is briefly introduced in this section. Since the distribution of SOLPS-ITER, it has been used to study boundary plasma physics in various tokamak devices. Thus, applications of SOLPS-ITER are also presented.

For ASDEX Upgrade L-mode low density discharges, the inner divertor is in the high recycling regime and outer divertor is in the low recycling regime. SOLPS5.0 provides confident results about electron density n_e and electron temperature T_e profiles at both inner and outer divertor targets [73][74]. The decrease of divertor target heat load with nitrogen seeding in ASDEX Upgrade L-mode discharges is successfully modelled by SOLPS5.0 [75]. The nitrogen retention in ASDEX Upgrade L-mode discharges is studied by SOLPS5.0 [76][77]. SOLPS5.0 simulation results with drifts and currents are compared in detail with experimental data, showing that the particle fluxes at inner divertor targets are higher than experimental measurements in the onset of detachment and fluctuating detachment states [63]. SOLPS5.0 modelling results also show that the HFSHD region is associated with drifts, which move particle from the outer to the inner divertor region. For SOLPS5.0 modelling about H-mode nitrogen seeding discharges, F. Reimold shows that [64] considering the convective transport due to filaments, which is mimicked by adding a pinch velocity, the discrepancies on the particle flux at the inner target are reduced and also a good agreement on volume electron density is recovered.

Now, SOLPS-ITER is widely used for boundary plasma study. SOLPS-ITER is applied to study the effect of drifts in TCV [78], Alcator C-mod [79] and DIII-D [80]. Impurity radiation in ITER is investigated by SOLPS-ITER [81]. The effect of drifts for snowflake [82][83] and upper single null configurations [84] in ASDEX Upgrade are studied by SOLPS-ITER. The detachment operation in HL-2M is predicted by SOLPS-ITER [85].

4.2 B2.5

In this section, the basic fluid equations of B2.5 used in SOLPS-ITER are introduced.

4.2.1 Braginskii equations

B2.5 equations are based on Braginskii equations [86] which are following:
Particle conservation equation for ion:

$$\frac{\partial n_i}{\partial t} + \nabla \cdot \left(n_i \vec{V}_i \right) = S_{n_i} \tag{4.1}$$

Particle conservation equation for electron:

$$\frac{\partial n_e}{\partial t} + \nabla \cdot \left(n_e \vec{V}_e \right) = S_e \tag{4.2}$$

Momentum conservation equation for ion:

$$\frac{\partial}{\partial t} \left(m_i n_i \vec{V}_i \right) + \vec{\nabla} \cdot \left(m_i n_i \vec{V}_i \vec{V}_i \right) =$$
$$-\vec{\nabla} p_i - \vec{\nabla} \ddot{\Pi}_i + Z_i e n_i \left(\vec{E} + \vec{V}_i \times \vec{B} \right) + \vec{R}_i + \vec{S}_{m_i \vec{V}_i} \tag{4.3}$$

Beacause the electron mass is much lighter than ion mass, terms related to electron mass are neglected. The simplified momentum conservation equation for electron:

$$-\vec{\nabla} p_e - e n_e \left(\vec{E} + \vec{V}_e \times \vec{B} \right) + \vec{R}_e = 0 \tag{4.4}$$

where

$$\vec{R} \equiv \vec{R}_e = -\vec{R}_i = e n_e \left(\frac{\vec{j}_{\parallel}}{\sigma_{\parallel}} + \frac{\vec{j}_{\perp}}{\sigma_{\perp}} \right) - 0.71 n_e \vec{\nabla} T_e - \frac{3}{2} \frac{e n_e^2}{\sigma_{\perp} B^2} \vec{B} \times \vec{\nabla} T_e \tag{4.5}$$

is responsible for the friction between ion and electron. $\ddot{\Pi}$ is the viscosity tensor. $\vec{j}_{\parallel}$ and $\vec{j}_{\perp}$ are the parallel and perpendicular current respectively. $\sigma_{\parallel}$ and $\sigma_{\perp}$ are the classical electrical conductivities.

Energy conservation equation for ion:

$$\frac{\partial}{\partial t} \left(\frac{3}{2} n_i T_i + \frac{m_i n_i}{2} \vec{V}_i^2 \right) +$$
$$\vec{\nabla} \cdot \left[\left(\frac{5}{2} n_i T_i + \frac{m_i n_i}{2} \vec{V}_i^2 \right) \vec{V}_i + \ddot{\Pi}_i \cdot \vec{V}_i + \vec{q}_i \right] \tag{4.6}$$
$$= \left(e n_i Z_i \vec{E} - \vec{R} \right) \cdot \vec{V}_i - Q_{ei} + S_E^i$$

Simplified energy conservation equation for electron:

$$\frac{\partial}{\partial t} \left(\frac{3}{2} n_e T_e \right) + \vec{\nabla} \cdot \left(\frac{5}{2} n_e T_e \vec{V}_e + \vec{q}_e \right) = - e n_e \vec{E} \cdot \vec{V}_e + \vec{R} \cdot \vec{V}_i + Q_{ei} + S_E^e \tag{4.7}$$

where $\vec{q}_i$ and $\vec{q}_e$ are the ion and electron heat flux denstity.

4.2.2 B2.5 equations

In a tokamak device, there is toroidal symmetry. In B2.5, Braginskii equations are transformed from a referenced parallel coordinate system to a poloidal coordinate system through mathematical treatment [92], which means only poloidal

and radial transport are considered, as in Figure 4.2. The magnetic field $\vec{B}$ in tokamak has two components: poloidal field $\vec{B}_x$ and toroidal field $\vec{B}_z$ along the poloidal and toroidal directions. The radial direction is $\vec{B}_y$. In the parallel coordinate system (parallel $\vec{B}_\parallel$, diamagnetic $\vec{B}_\perp$ and radial $\vec{B}_y$), the parallel direction is the direction along the magnetic field line, the diamagnetic direction $\vec{B}_\perp$ is perpendicular to both parallel and radial direction.
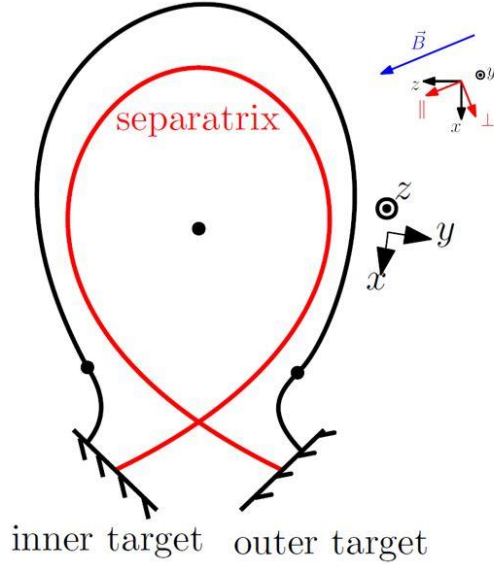
Figure 4.2 Schematic view of parallel and poloidal coordinate systems [88].

The basic fluid plasma equations in B2.5 for SOLPS-ITER are following.
For particle conservation equation:

$$\frac{\partial n_a}{\partial t} + \frac{1}{\sqrt{g}} \frac{\partial}{\partial x}\left(\frac{\sqrt{g}}{h_x}\tilde{\Gamma}_{ax}\right) + \frac{1}{\sqrt{g}}\frac{\partial}{\partial y}\left(\frac{\sqrt{g}}{h_y}\tilde{\Gamma}_{ay}\right) = S_a^n \qquad (4.8)$$

$$\tilde{\Gamma}_{ax} = \left(b_x V_{\parallel a} + V_{ay}^{(E)} + V_{ay}^{(AN)} + V_a^{corr\_dpc}\right)n_a - D_{n,a}\frac{1}{h_x}\frac{\partial n_a}{\partial y} + \tilde{\Gamma}_{ax}^{(dia)} \quad (4.9)$$

$$\tilde{\Gamma}_{ay} = \left(V_{ay}^{(E)} + V_{ay}^{(AN)}\right)n_a + \frac{\left(j_y^{(AN)} + j_y^{(in)} + \tilde{j}_y^{(vis\parallel)} + \tilde{j}_y^{(vis\perp)} + \tilde{j}_y^{(visq)}\right)}{e}$$
$$- D_{n,a}\frac{1}{h_x}\frac{\partial n_a}{\partial y} + \tilde{\Gamma}_{ay}^{(dia)} \qquad (4.10)$$

In B2.5, only the parallel component of the momentum transport is fully written down in a conservation equation:

$$m_a \frac{\partial n_a V_{\parallel a}}{\partial t} + \frac{1}{h_z \sqrt{g}} \frac{\partial}{\partial x} \left(\frac{h_z \sqrt{g}}{h_x} \Gamma_{ax}^m \right) + \frac{1}{h_z \sqrt{g}} \frac{\partial}{\partial y} \left(\frac{h_z \sqrt{g}}{h_y} \Gamma_{ay}^m \right) +$$

$$\frac{b_x}{h_x} \frac{\partial n_a T_u}{\partial x} + Z_a e n_a \frac{b_x}{h_x} \frac{\partial \Phi}{\partial x} =$$

$$S_{a\parallel}^m + S_{CF_a}^m + S_{fr_a}^m + S_{Therm_a}^m + S_{I_a}^m + S_{R_a}^m + S_{CX_a}^m + S_{AN_a}^m + S_{EIRENE_a}^m \qquad (4.11)$$

$$\Gamma_{ax}^m = m_a V_{\parallel a} \Gamma_{ax}^{Cor} + \frac{4}{3} \widetilde{\widetilde{\eta}}^{(CL)} \frac{\partial \ln h_z}{h_x \partial x} V_{\parallel a} - \eta_{ax} \frac{\partial V_{\parallel a}}{h_x \partial x}, \ \ z_a = 1 \& z_{n,a} = 1$$

$$\qquad (4.12)$$

$$= m_a V_{\parallel a} \Gamma_{ax}^{Cor} - \eta_{ax} \frac{\partial V_{\parallel a}}{h_x \partial x}, \ \ \text{otherwise}$$

$$\Gamma_{ay}^m = m_a V_{\parallel a} \Gamma_{ay}^{Cor} - \eta_{ay} \frac{\partial V_{\parallel a}}{h_y \partial y} \qquad (4.13)$$

For electron energy conservation equation:

$$\frac{3}{2} \frac{\partial n_e T_e}{\partial t} + \frac{1}{\sqrt{g}} \frac{\partial}{\partial x} \left(\frac{\sqrt{g}}{h_x} \tilde{q}_{ex} \right) + \frac{1}{\sqrt{g}} \frac{\partial}{\partial x} \left(\frac{\sqrt{g}}{h_y} \tilde{q}_{ey} \right)$$

$$+ \frac{n_e T_e}{\sqrt{g}} \frac{\partial}{\partial x} \left(\frac{\sqrt{g}}{h_x} b_x V_{e\parallel} \right) =$$

$$Q_e + c_{E \times B} n_e T_e B_z \frac{1}{h_x h_y} \left(\frac{\partial \Phi}{\partial y} \frac{\partial}{\partial x} \left(\frac{1}{B^2} \right) - \frac{\partial \Phi}{\partial x} \frac{\partial}{\partial y} \left(\frac{1}{B^2} \right) \right)$$

$$- \frac{j_y^{(ST)}}{e n_e} \frac{\partial n_e T_e}{h_y \partial y} + Q_{Fei} + Q_e^{EIRENE} \qquad (4.14)$$

$$\tilde{q}_{ex} = \left(\frac{3}{2} \Gamma_{ex} + V_{ex}^{(str)} n_e - \tilde{c}_e^{(2)} \frac{j_x^{(\parallel)}}{e} \right) T_e - \kappa_{ex} \frac{1}{h_x} \frac{\partial T_e}{\partial x} - q_{ex}^{P.Sch} \qquad (4.15)$$

$$\tilde{q}_{ey} = \frac{3}{2} \left(\Gamma_{ey} - \frac{5}{3} \frac{j_y^{(ST)}}{e} \right) T_e - \kappa_{ey} \frac{1}{h_y} \frac{\partial T_e}{\partial y} - q_{ey}^{P.Sch} \qquad (4.16)$$

For ion energy conservation equation;

$$\frac{3}{2} \frac{\partial n_i T_i}{\partial t} + \frac{1}{\sqrt{g}} \frac{\partial}{\partial x} \left(\frac{\sqrt{g}}{h_x} \tilde{q}_{ix} \right) + \frac{1}{\sqrt{g}} \frac{\partial}{\partial y} \left(\frac{\sqrt{g}}{h_y} \tilde{q}_{iy} \right)$$

$$+ \sum_{a=0}^{ns-1} \frac{n_a T_i}{\sqrt{g}} \frac{\partial}{\partial x} \left(\frac{\sqrt{g}}{h_x} V_{a\parallel} b_x \right)$$

$$\qquad (4.17)$$

$$= Q_\Delta + Q_{F_{ab}} + c_{E \times B} T_i B_z \frac{1}{h_x h_y} \left(\frac{\partial \Phi}{\partial y} \frac{\partial}{\partial x} \left(\frac{1}{B^2} \right) - \frac{\partial \Phi}{\partial x} \frac{\partial}{\partial y} \left(\frac{1}{B^2} \right) \right) \sum_{a=0, Z_a \neq 0}^{ns-1} n_a$$

$$+ \sum_{fluid \ species} \left(\eta_{ax} \left(\frac{\partial V_{a\parallel}}{h_x \partial x} \right)^2 + \eta^{(AN)} \left(\frac{\partial V_{a\parallel}}{h_y \partial y} \right)^2 \right) + Q_I^{(i)} + Q_R^{(i)} + Q_i^{EIRENE}$$

$$\tilde{q}_{ix} = \frac{3}{2} \Gamma_{ix} T_i + V_{ix}^{(str)} n_i T_i - \kappa_{ix} \frac{1}{hx} \frac{\partial T_i}{\partial x} - q_{ix}^{P.Sch} \qquad (4.18)$$

$$\tilde{q}_{iy} = \left[\frac{3}{2} \Gamma_{iy} + V_{iy}^{(str)} n_i + \frac{3}{2} \frac{\left(j_y^{(AN)} + \tilde{j}_y^{(vis \parallel)} + \tilde{j}_y^{(vis \perp)} + \tilde{j}_y^{(visq)} + j_y^{(in)} \right)}{e} \right] T_i$$

$$- \kappa_{iy} \frac{1}{h_y} \frac{\partial T_i}{\partial y} - q_{iy}^{P.Sch} \tag{4.19}$$

For current conservation equation:

$$\frac{1}{\sqrt{g}} \frac{\partial}{\partial x} \left(\frac{\sqrt{g}}{h_x} j_x \right) + \frac{1}{\sqrt{g}} \frac{\partial}{\partial y} \left(\frac{\sqrt{g}}{h_y} j_y \right) = 0 \tag{4.20}$$

$$j_x = j_x^{(AN)} + \tilde{j}_x^{(dia)} + j_x^{(in)} + \tilde{j}_x^{(vis \parallel)} + \tilde{j}_y^{(vis \perp)} + \tilde{j}_x^{(visq)} + \tilde{j}_x^{(s)} + \tilde{j}_x^{(\parallel)} \tag{4.21}$$

$$j_y = j_y^{(AN)} + \tilde{j}_y^{(dia)} + j_y^{(in)} + \tilde{j}_y^{(vis \parallel)} + \tilde{j}_y^{(vis \perp)} + \tilde{j}_y^{(visq)} + \tilde{j}_y^{(s)} \tag{4.22}$$

The right terms of equation (4.8), (4.11), (4.14) and (4.17) are source terms due to volumetric process as mentioned in section 2.1.

In section 2.5, the perpendicular transport is introduced. For boundary plasma modelling, the perpendicular transport can be diffusion or convection or a combination of them. In B2.5, only the parallel momentum conservation is considered and the perpendicular transport (both $\vec{e}_y$ and $\vec{e}_\perp$) is determined by drifts, currents, diffusion and anomalous transport as in equation (4.10). In B2.5 the transport due to drifts is described following [71]. In this study in chapter 6, the convective transport by filaments is mimicked through radial convective transport similar to [42].

$$\Gamma_{ix} = b_x \Gamma_{i \parallel} + b_z \Gamma_{i \perp}$$

$$\Gamma_{iy} = \Gamma_{iy}^{(AN)} + \Gamma_{iy}^{(drifts)} + \Gamma_{iy}^{(current)} - D_\perp \frac{\partial n}{\partial y} \tag{4.23}$$

$$\Gamma_{i \perp} = \Gamma_{i \perp}^{(AN)} + \Gamma_{i \perp}^{(drifts)} + \Gamma_{i \perp}^{cond} - D_\perp \nabla_\perp n$$

For SOLPS-ITER, it possible to use a fast and simple fluid neutral model. The source terms are calculate by B2.5 atomic package, and the above equations are applied for fluid neutral species. In order to avoid unphysically large fluxes, flux-limits for particle flux and heat flux are introduced [89]. In SOLPS code package, there is also an option for adopting kinetic neutral models, where the neutral transport and atomic reactions is described by Monte-Carlo code, EIRENE. For the kinetic neutral models, running time is longer than the fluid neutral model, even several weeks.

4.2.3 Computational domain and boundary conditions

B2.5 solves the above conservation equations in a rectangle which is mapped from a physical domain, as shown in Figure 4.3, which is a typical example for a lower single null configuration.
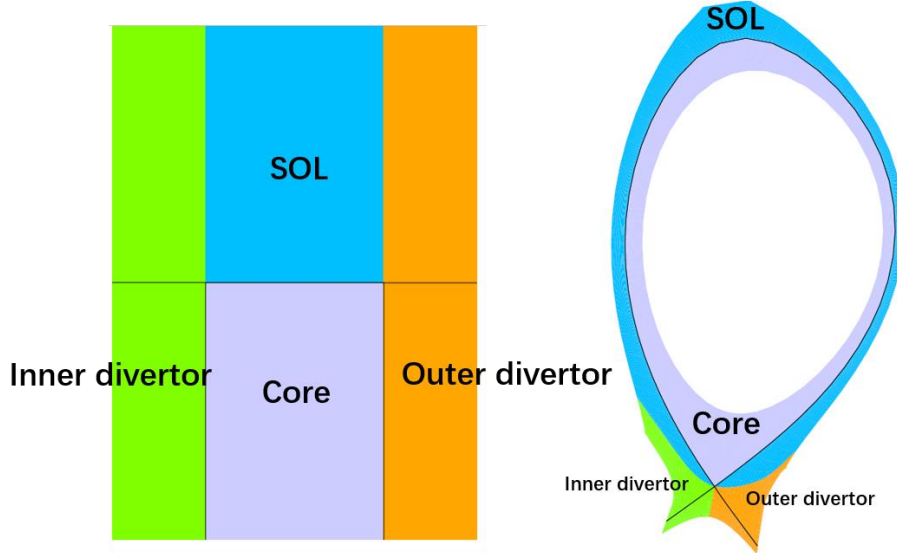
Figure 4.3 Computational domain and physical domain for ASDEX Upgrade lower single null configuration.

B2.5 is essentially a computational fluid solver; boundary conditions are implemented through "infinitesimal" small volume elements along boundaries, the so-called "guard cells" [92]. The desired boundary conditions are implemented by forcing proper sources (not source terms in conservation equations) in the guard cells. For example, if a flux Φ is desired to cross a boundary grid cell of area A, the corresponding source (sink) in the adjacent guard cell is set up to be $-\Phi A$. SOLPS-ITER provides various types of boundary conditions e.g. fixed density or fixed particle flux at core boundary. For divertor targets, usually sheath conditions are selected, prescribing the velocity and heat flux at the sheath entrance. In the thin sheath region, the fluid approximation of plasma is broken. For example, the collisional mean free paths for ions and electrons are about 0.17m and 9m, while the sheath length is about 10^{-5} m. The fluid assumption works well in other region, because the connection length is much larger, e.g. ~16m for ASDEX Upgrade [92].

4.3 EIRENE

Here we present basic knowledge about EIRENE.

4.3.1 Physics of EIRENE

In SOLPS code package, a detailed kinetic neutral transport is provided by EIRENE, which is a Monte Carlo code coupled to B2.5. With a plasma background, the particle source, momentum source and energy source due to plasma and neutral interactions are calculated by EIRENE.

Even if EIRENE is very complicated, the main idea is simple: using the Monte Carlo Method to solve Boltzmann equation in a domain. For boundary plasma

modelling, the domain is the vacuum vessel including the plasma region and the surrounding vacuum up to the solid surfaces. For example, neutral hydrogenic atoms D, neutral hydrogenic molecules D_2 and shorting living molecular ions D_2^+ are considered. The source of such type of particles could be gas puffing, recycling at surface and volumetric recombination. Neutral particles move along straight lines until they undergo an 'event' which could change their direction and/or end their life. The 'event' could be ionization or pumping, also neutral-plasma collision and reflection at material surfaces. After a large number of particle histories is recorded, the distribution of the particles is examined.

In addition to B2.5, EIRENE was also coupled to other fluid plasma codes e.g. EMC3 [94][95], EDGE2D [96][97] and SOLEDGE2D [98].

4.3.2 Coupling procedures

When EIRENE runs coupled to B2.5, the particle, parallel ion momentum, electron energy and ion energy source terms, namely SNI, SMO, SEE, SEI, respectively, are provided by EIRENE only in the outer iteration [100]. During the process of inner iteration, SIMPLE algorithm is used to solve fluid plasma equations [99]. The coupling procedures for B2.5-EIRENE in SOLPS-ITER are following:

- Fluxes (particle, momentum and energy) and plasma background are passed to EIRENE.
- The geometric data, source sampling distribution is prepared.
- EIRENE calculates the volume integrated source terms.
- The source terms are rescaled and linearized.
- The total energy sources SEE and SEI are transferred to internal source terms.
- EIRENE provides source terms to B2.5.

It should be noted that in B2.5, the internal ion and electron energy equations are solved. In the coupling procedures, the total ion and electron energy sources are obtained [69][100]. The total energy source terms are transferred to internal energy source and then passed to B2.5.

$$S_{EIR}^{internal} = S_{EIR}^{total} - \sum_a \left(v_{\parallel a} S_{EIR}^m - \frac{1}{2} m_a v_{\parallel a}^2 S_{EIR}^n \right) \qquad (5.1)$$

where S_{EIR}^m and S_{EIR}^n are the momentum and particle sources calculated by EIRENE respectively.

Chapter 5

Comparison of SOLPS5.0 and SOLPS-ITER

5.1 Modelling setup

As mentioned in section 3.1, SOLPS5.0 has been used for ASDEX Upgrade boundary plasma modelling more than twenty years. As a common sense in SOLPS community, based on previous SOLPS modelling cases, it can increase modelling efficiency and avoid numerical problems. SOLPS-ITER is the newest version of the SOLPS code package, which includes not only SOLPS5.0 physics but also a large number of new physics/numerics improvements/additions recommended to SOLPS users [111]. Thus, in order to use SOLPS-ITER to continue SOLPS5.0 modelling to study detachment states, it is necessary to examine the backward compatibility of SOLPS-ITER with SOLPS5.0. At least, carefully evaluating the differences of the plasma parameters computed by SOLPS-ITER and SOLPS5.0, at upstream (outer mid-plnae) and divertor targets, in a framework where the same physics (plasma transport model, boundary conditions, transport coefficients, etc.) and numerics are used. Besides, in order to use the new drifts model in SOLPS-ITER, the recommended new physics/numerics improvements/additions are prerequisite.

In SOLPS code package, both fluid neutral model and kinetic neutral model are provided. For fluid neutral model, all the recommended physics/numerics in SOLPS-ITER can be disable, which means the difference should be small. For kinetic neutral model, the differences should be evaluated. This is because a lot of improvements are implemented in new version of EIRENE [112] that is used in SOLPS-ITER. The backward compatibility of SOLPS-ITER with SOLPS4.3 has already be examined. The remaining differences are within ~20%; they might be from different formulations of the equations and the different discretization schemes [69]. The fluid part of B2.5 in SOLPS-ITER has been proved match well with B2.5 in SOLPS5.0 [71]. The results of a numerical comparison between SOLPS-ITER and SOLPS 5.0 are in the next setcion, including fluid and kinetic neutral models. For SOLPS-ITER solutions, there are two types. One is named as SOLPS-ITER-backward which is optimized to mimic SOLPS5.0 physics/numerics. Another one named SOLPS-ITER includes the recommended physics/numerics except drifts. For SOLPS5.0, EIRENE96 and EIRENE99 are provided; we select EIRENE99.

The computaional grid is shown in Figure 5.1. There are 96 cells in the poloidal direction and 36 cells in the radial direction. In SOLPS-ITER, various types of boundary conditions are provided e.g. temperature or power flux at the core boundary. In this section, the input power across the core boundary is set as 0.8 MW and equally distributed to electrons and ions. The most common boundary condition for particle conservation equation at the core boundary is ion density or ion flux. In this charpter, a value of 1×10^{20} s^{-1} is prescribed for the ion particle flux across the core boundary for numerical stability reasons i.e. to prevent the possible appearance of a small negative flux if we set the condition of exactly zero flux, which would affect the total particle balance.
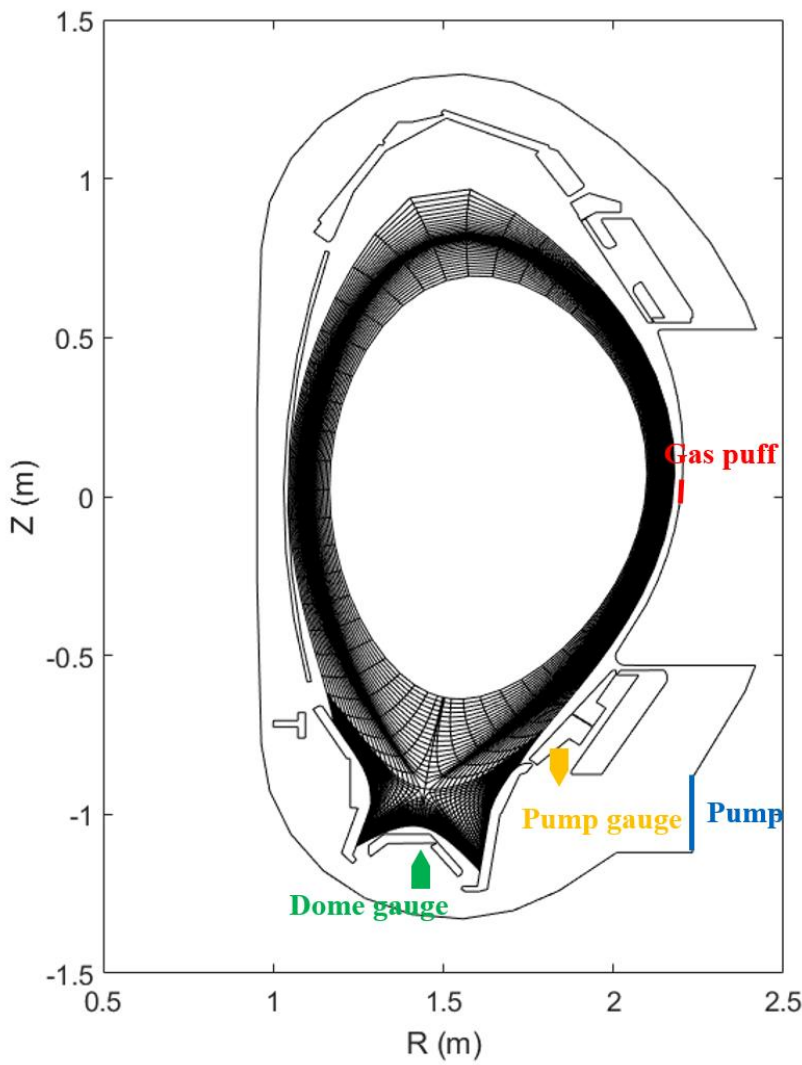
Figure 5.1 Computational grid (96 × 36) and vessel structures.

In SOLPS code package, it is possible to either operate with a fixed gas puff level, or automatically feedback-controlled mode to obtain a desired electron density value at the outer mid-plane separatrix. Both options are included in this study. The corresponding electron density at outer mid-plane separatrix $n_{e,sep}$ and

gas puffing rate Γ_{puff} are summarized in Table 5.1. At both the private flux region and wall boundaries, we choose a particle density decay length of 2.5 cm for all ionic species and a temperature decay length of 1 cm. The perpendicular transport coefficients are shown in figure 5.2; they have been fine-tune to experimental data [63]. In SOLPS-ITER, physical models are selected through corresponding "switches" that allow users to use the ones which are same in SOLPS5.0 or the new physics/numerics improvements/additions. The details about the switches about SOLPS-ITER-backward can be found in [111][113].

Table 5.1 Outer mid-plane electron density $n_{e,sep}$ (m^{-3}) for feedback-controlled mode cases and gas puffing rate Γ_{puff} (D/s) for fixed gas-puff-controlled mode cases.

	$n_{e,sep}$ (m^{-3}) at feedback-controlled mode	Γ_{puff}(D/s) at fixed gas-puff-controlled mode
Fluid neutral model	2.0E19	None
Kinetic neutral model	2.0E19	4.7E21
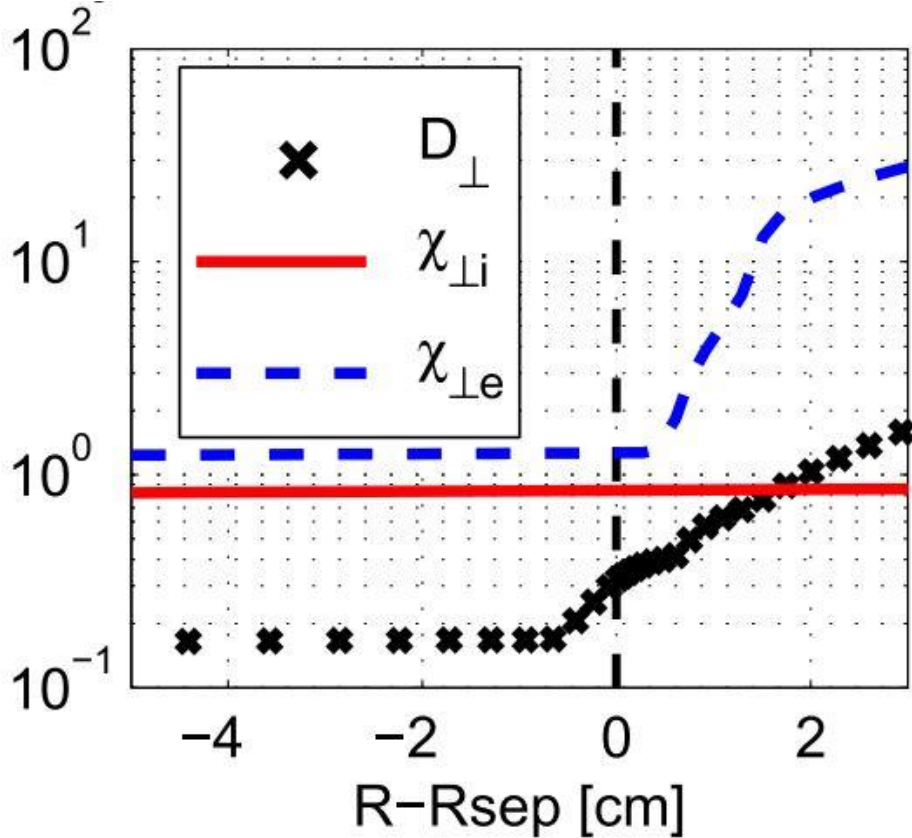
Figure 5.2 Perpendicular transport coefficients along the outer mid-plane[63].

For kinetic neutral model, neutral particle transport is described by EIRENE, which follows both atoms and molecules after their entering the domain. The volumetric processes (ionization, recombination and charge-exchange) depends on rate coefficients from database. The list of atomic reactions used in this section is in Table 5.2; this is the same as the Kotov-2008 model [114] except for dissociative recombination (D+2+e→2D+ +2e). The is because EIRENE provides standard setting about atomic reactions. The dissociative recombination is only included in

the version EIRENE in SOLPS-ITER, not EIRENE99. We adopt the standard reflection model at all surfaces, except the pumping surface. The surface interaction database of different projectile and material surfaces is from TRIM [115][116]. In this section, for the pumping surface the albedo is 0.9 to mimic a pumping speed $\sim 114\text{m}^3/\text{s}$ of ASDEX Upgrade [42] including the cryopump and turbopump [117].

Table 5.2 Atomic and molecular processes for deuterium used by EIRENE.

Reactions
$D + e \rightarrow D^+ + 2e$
$D^+ + e \rightarrow D + hv$
$D^+ + 2e \rightarrow D + e$
$D + D^+ \rightarrow D^+ + D$
$D_2 + e \rightarrow D_2^+ + 2e$
$D_2 + e \rightarrow 2D + e$
$D_2 + e \rightarrow D + D^+ + 2e$
$D_2 + D^+ \rightarrow D_2 + D^+$
$D_2 + D^+ \rightarrow D_2^+ + D$
$D_2^+ + e \rightarrow D + D^+ + e$
$D_2^+ + e \rightarrow 2D^+ + 2e$

5.2 Simulation results

5.2.1 Fluid neutral model

The comparison results about fluid neutral model are introduced in this section. Figure 5.3 shows the electron density n_e and electron temperature T_e profiles at the outer mid-plane. There is a good agreement between SOLPS-ITER-backward and SOLPS5.0, similarly to [71] that electron density n_e profiles at the outer mid-plane of SOLPS5.2 are identical to SOLPS5.0 for L-mode simulation. SOLPS-ITER shows ~5% higher of electron density and ~5% lower of electron temperature than SOLPS-ITER-backward, especially in the core region.
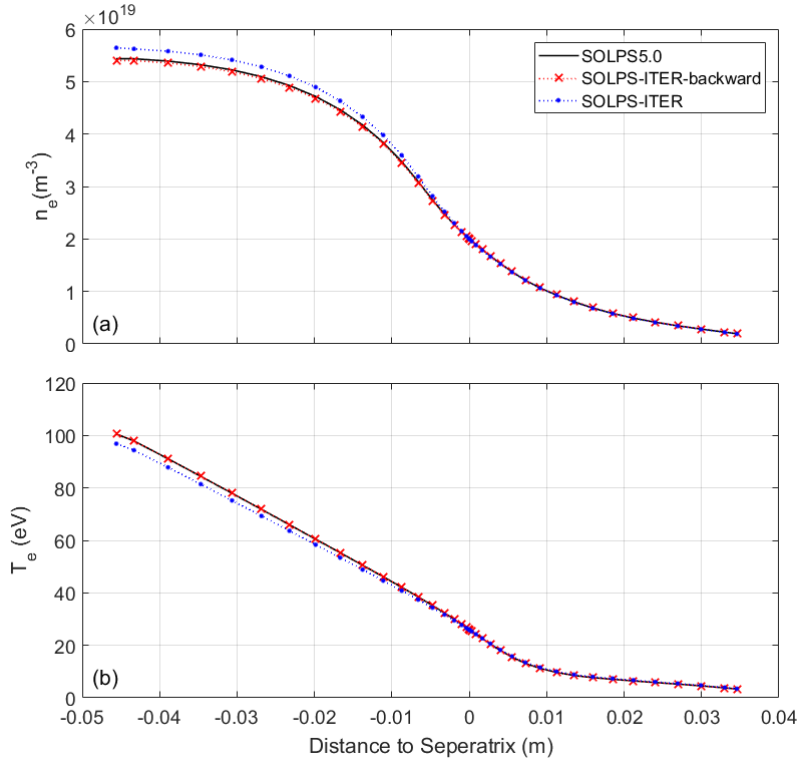
Figure 5.3 (a) Electron density n_e and (b) electron temperature T_e profiles at the outer mid-plane for fluid neutral model. Electron density at the outer mid-plane separatrix $n_{e,sep}$ ($\sim 2.0 \times 10^{19}$ m^{-3}) is feedback-controlled through neutral flux at the wall boundary.

Electron density n_e and electron temperature T_e profiles at outer target are in Figure 5.4. SOLPS-ITER-backward successfully reproduces SOLPS5.0 results, except the n_e profiles at outer target which have a ~15% discrepancy. Such discrepancy might be from the discretization error induced by computational grid [69][118]. SOLPS-ITER target profiles present stronger discrepancies with SOLPS-ITER-backward. These will disappear in kinetic neutral cases, (see the discussion of Figure 5.7 below), thus a reasonable explanation is that they are due to the recommended physics/numerics related to fluid neutral models (e.g. flux limits, parallel transport coefficients, fluid source terms etc.) implemented in SOLPS-ITER.
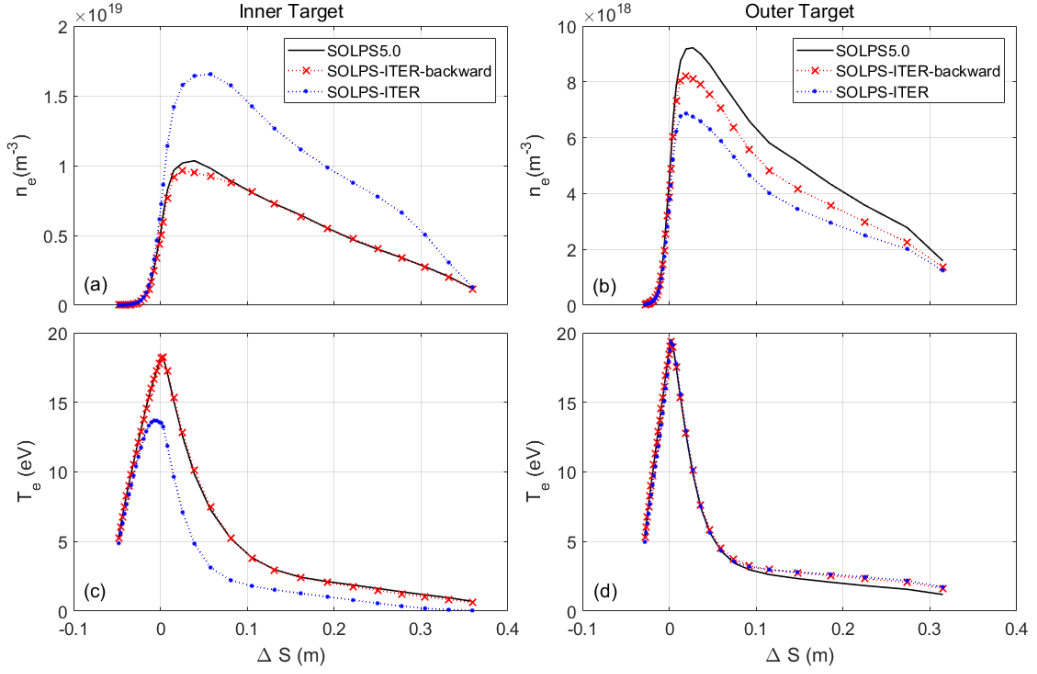
Figure 5.4 Targets profiles for fluid neutral model. (a) Electron density n_e profiles at the inner target, (b) electron density n_e profiles at the outer target, (c) electron temperature T_e profiles at the inner target and (d) electron temperature T_e profiles at the outer target.

The profiles of poloidal current density j_x including contributions from the classical parallel and anomalous radial currents projected onto the poloidal direction, are shown in Figure 5.5. The parallel current is a strong function of electron density n_e and electron temperature T_e; and the implemented radial transport models are similar [118]. Furthermore, the parallel electron thermal conductivity used to determine $j_{\parallel}$ is slightly different [93] [113], so it is not surprising to see that again SOLPS-ITER-backward can accurately reproduce SOLPS5.0 results, while the agreement with SOLPS-ITER is more qualitative.
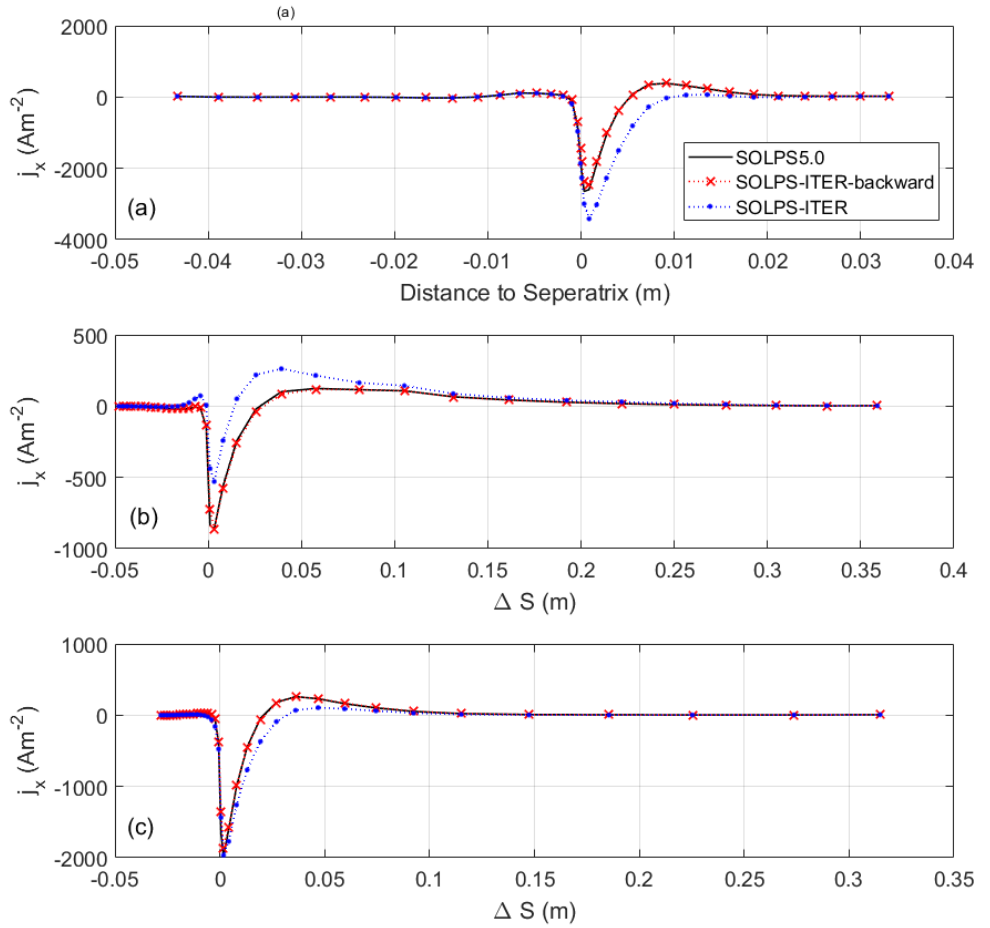
Figure 5.5 Profiles of the poloidal current density j_x at (a) the outer mid-plane, (b) the inner target, and (c) the outer target.

5.2.2 Kinetic neutral model

For kinetic neutral cases, both fixed gas-puff controlled and feedbackcontrolled modes are considered. Outer mid-plane n_e and T_e profiles in fixed gas-puff controlled mode are presented in Figure 5.6. There is ~8% difference in the core region between SOLPS-ITER-backward and SOLPS5.0, while the difference between SOLPS-ITER and SOLPS-ITER-backward is ~5%. At the targets, SOLPS-ITER-backward and SOLPS-ITER results match closely while SOLPS5.0 shows sensibly different results, as seen in Figure 5.7. The new version of EIRENE is the main driver for the differences (~20%) between SOLPS-ITER backward and SOLPS5.0; this can be deduced because in fluid neutral cases, such differences are not observed.
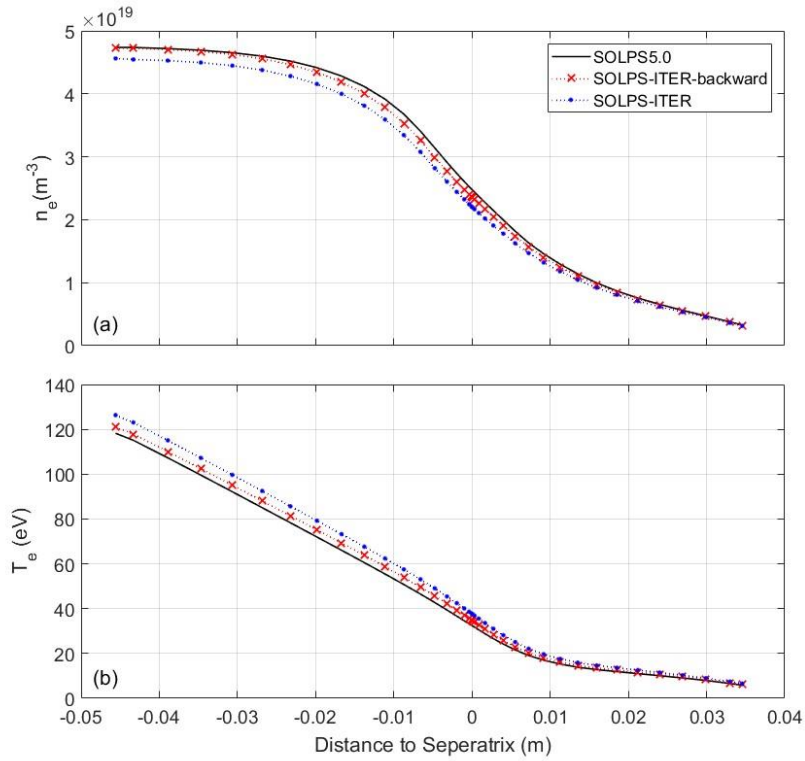
Figure 5.6 (a) Electron density n_e profiles and (b) electron temperature T_e profiles at the outer mid-plane for kinetic neutral cases in fixed gas-puff mode. The gas-puff value is 4.7×10^{21} D/s. The upstream density is $2.5 \times 10^{19} m^{-3}$, $2.3 \times 10^{19} m^{-3}$, and $2.2 \times 10^{19} m^{-3}$ for SOLPS5.0, SOLPS-ITER-backward, and SOLPS-ITER, respectively.
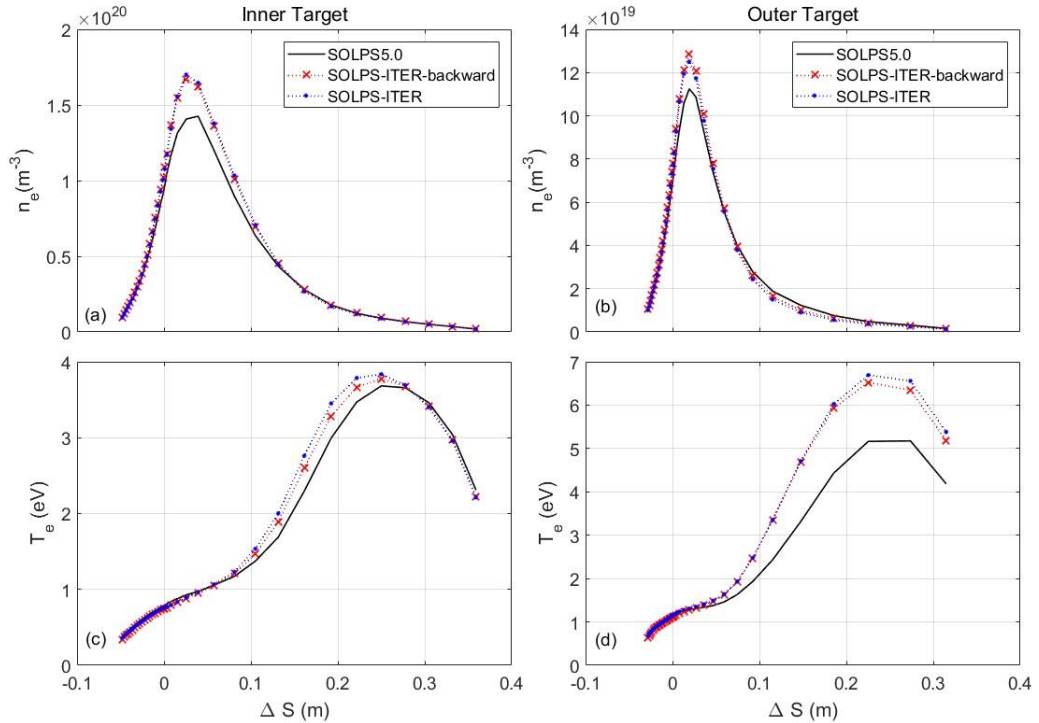
Figure 5.7 Target profiles for kinetic neutral cases in fixed gas-puff mode: (a) Electron density n_e profiles at the inner target, (b) electron density n_e profiles at the outer target, (c) electron temperature T_e profiles at the inner target, and (d) electron temperature T_e profiles at the outer target.

We also check the total particle source SNI, electron energy SEE and ion energy sources SEI provided by EIRENE, which are given in Table 5.3, while Figure 5.8 shows the detailed 2D distributions in the divertor region (including also a zoom near the outer target). Even if the total ion energy source in SOLPS5.0 is only ~60% of the other two, the energy source is higher near the outer divertor target. For the total particle and electron energy sources, the differences are small (~5%), so we believe that the ion energy source calculated by EIRENE is mainly responsible for the observed discrepancies between SOLPS5.0 and SOLPS-ITER-backward. It should be noted that the sources distribution shown in Figure 5.8 are taken from cases converged with the respective codes, so the sources are not calculated from exactly the same plasma background. As a further check of our hypothesis, we also run EIRENE99 in standalone mode in SOLPS-ITER-backward, with exactly same plasma background, reflection models, atomic database and large trajectory number. The results for the total source are also shown in Table 5.3, qualitatively confirming our discussion. The reason of the lower ion energy source calculated by EIRENE99 is unclear now, in the future a full benchmark activity similar to is expected to solve this problem.
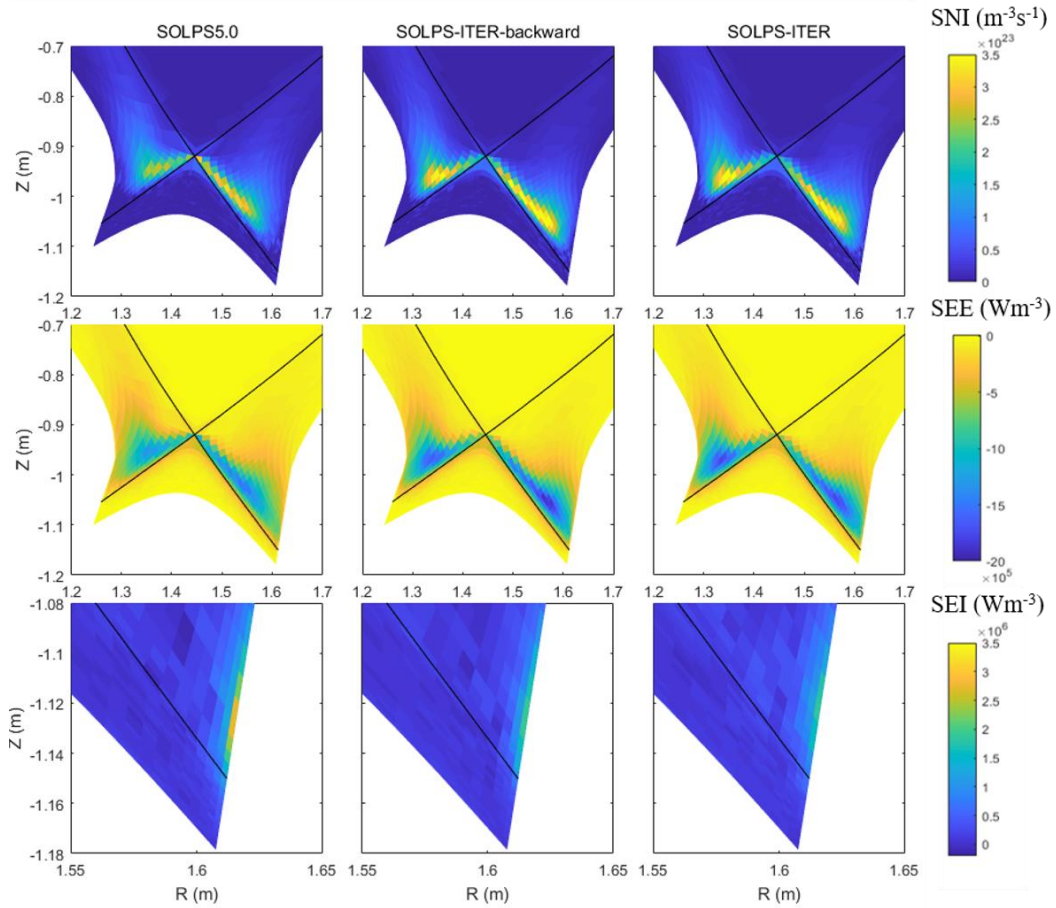
Figure 5.8 Distributions of ion source (SNI), electron energy source (SEE), and ion energy source (SEI). From left to right are SOLPS5.0, SOLPS-ITER-backward, and SOLPS-ITER. From top to bottom are SNI, SEE, and SEI. For SEI, only the region near outer target is shown.

Table 5.3 Total particle source (SNI), total electron energy source (SEE), and total ion energy source (SNI) provided by EIRENE. The values in parentheses are calculated with exactly same plasma background, atomic database, and large trajectory number (100,000 in each strata).

Total Source	SNI (s^{-1})	SEE (W)	SEI (W)
SOLPS5.0	7.20E+22	-4.11E+5	6.59E+4
SOLPS-ITER-backward	7.66E+22(7.22E+22)	-4.14E+5(-4.01E+5)	1.05E+5(9.67E+5)
SOLPS-ITER	7.59E+22	-4.07E+5	1.08E+5

We also compare the neutral flux density at dome and pump gauges in Table 5.4, the corresponding locations are marked in Figure 5.1. With the same gas puffing rate, the neutral flux densities match within 4% differences. Thus, we believe that SOLPS-ITER-backward successfully reproduced SOLPS5.0 results about neutral flux density, even with different ion energy source.

Table 5.4 Neutral flux density at dome and pump gauges locations measured by EIRENE

	Flux density at dome gauge ($m^{-2}s^{-1}$)	Flux density at pump gauge($m^{-2}s^{-1}$)
SOLPS5.0	7.54E+22	4.54E+22
SOLPS-ITER-backward	7.73E+22	4.64E+22
SOLPS-ITER	7.52E+22	4.48E+22

The outer mid-plane profiles in feedback controlled mode are shown in Figure 5.9. At the core boundary, the electron density in SOLPS-ITER-backward is ~5% higher than SOLPS5.0. In order to get the same $n_{e,sep}$, a little higher gas puffing rate is required which is consistent with Figure 5.6, showing that with same gas puffing rate, the electron density n_e mid-plane profiles in SOLPS-ITER-backward are lower than SOLPS5.0. With similar upstream conditions, the targets profiles of SOLPS-ITER-backward and SOLPS5.0 match better than in fixed gas-puff mode: only ~10% discrepancies in Figure 5.10, as opposed to ~20% differences in Figure 5.7. The discrepancies of electron temperature target profiles between SOLPS-ITER-backward and SOLPS-ITER in Figure 5.10 are mainly from the different puffing rate due to different version of EIRENE. In SOLPS-ITER, the gas puffing rate ($\Gamma_{puff} \sim 4.17 \times 10^{21}$ D/s) is ~9% higher than SOLPS-ITER backward ($\Gamma_{puff} \sim 3.82 \times 10^{21}$ D/s) to achieve the prescribed $n_{e,sep}$ value. With a higher gas puffing rate, the targets are more detached and have lower electron temperature. This can be deduced from Table 5.5 which presents the pressure ratio between inner/outer targets and upstream. The values of SOLPS-ITER are lower than SOLPS-ITER-backward and SOLPS5.0, hich means the divertor targets are more detached in SOLPS-ITER.
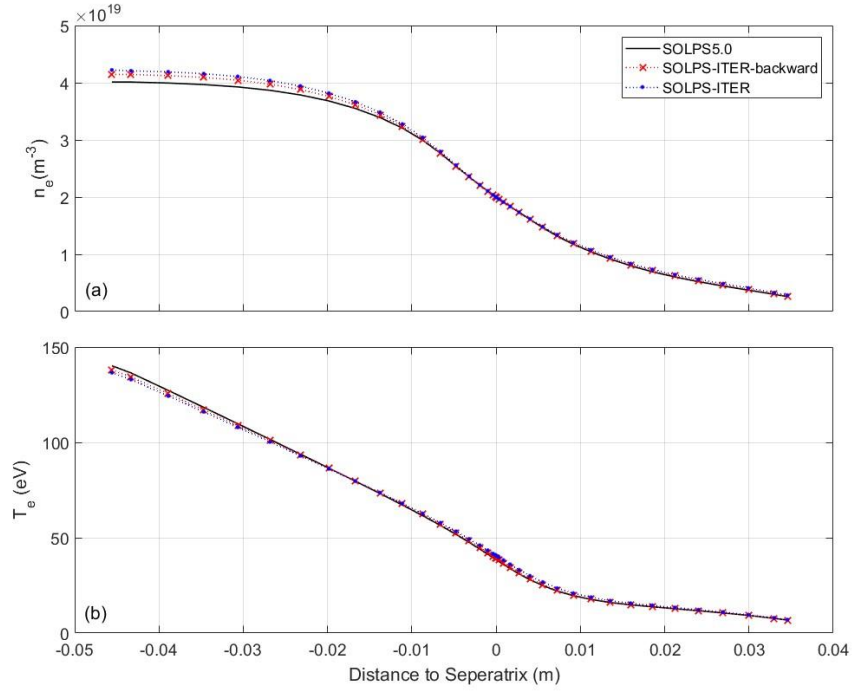
Figure 5.9 (a) Electron density n_e and (b) electron temperature T_e profiles at the outer mid-plane for kinetic neutral cases in feedback-controlled mode. The fixed upstream density $n_{e,sep}$ is 2.0×10^{19} m^{-3}. The gas puffing rate is 3.60×10^{21} D/s, 3.82×10^{21} D/s, and 4.17×10^{21} D/s for SOLPS5.0, SOLPS-ITER-backward, and SOLPSITER, respectively.
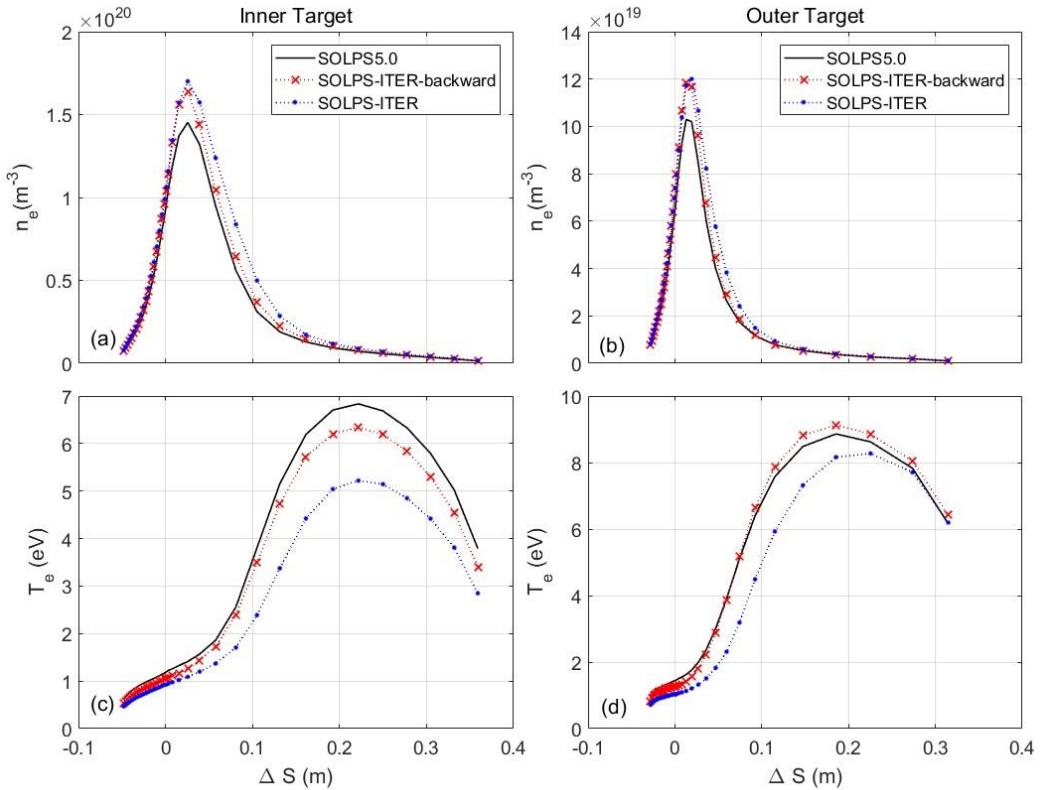
Figure 5.10 Target profiles for kinetic neutral cases in feedback control mode: (a) Electron density n_e profiles at the inner target, (b) electron density n_e profiles at the outer target, (c) electron temperature T_e profiles at the inner target, and (d) electron temperature T_e profiles at the outer target.

Table 5.5 Pressure ratio between inner/outer targets and upstream

	Inner target to upstream	Outer target to upstream
SOLPS5.0	0.67	0.73
SOLPS-ITER-backward	0.64	0.73
SOLPS-ITER	0.60	0.64

5.2.3 Detachment characteristic

We also test the capacity of the various code versions to capture detachment through an upstream density ($n_{e,sep}$) scan, varying it from 1.0×10^{19}/m^3 to 3.6×10^{19}/m^3 in feedback controlled mode. In Figure 5.11, the roll-over of the integrated ion flux at the targets, which is the characteristic of detachment, has been observed in all cases. SOLPS-ITER-backwards results in ~10% higher peak ion flux at the targets, compared to SOLPS5.0 from attached to detached state, but it can capture the roll-over detachment characteristic as predicted by SOLPS5.0. For SOLPS-ITER-backward and SOLPS-ITER, the discrepancy in the ion flux at the targets is smaller than SOLPS5.0. For the heat flux, there is a good agreement between SOLPS-ITER-backward and SOLPS5.0 at targets. However, SOLPS-ITER shows slightly lower values. This is because, in order to get the same $n_{e,sep}$ value, a higher gas puffing rate in SOLPS-ITER is needed, which is to compensate the effect of recommended physics/numerics that leads to the differences of targets density and temperature profiles associated with the calculation of the heat flux.
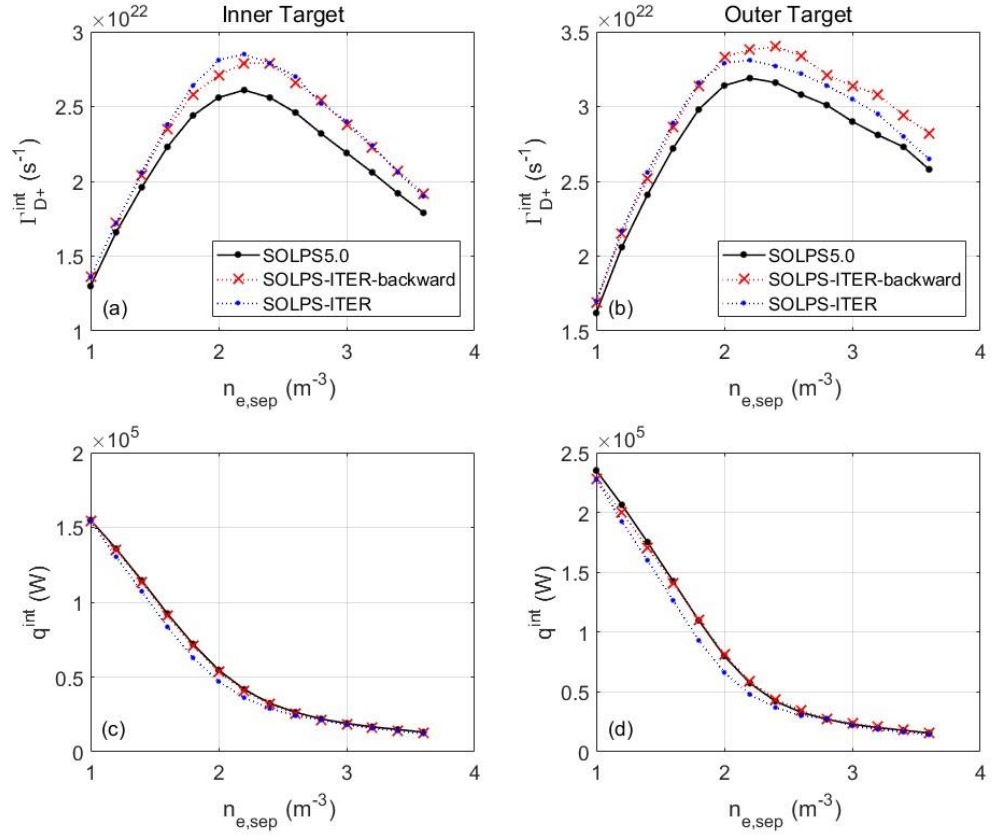
Figure 5.11 Density scan for electron density at outer mid-plane separatrix $n_{e,sep}$. (a) Integrated ion flux Γ_{D+}^{int} at the inner target and (b) integrated heat flux q_{int} at the inner target, as a function of $n_{e,sep}$. (c) Integrated ion flux Γ_{D+}^{int} at the outer target and (d) integrated heat flux q_{int} at the outer target, as a function of $n_{e,sep}$.

The lower heat flux of SOLPS-ITER compared to SOLPS5.0 and SOLPS-ITER-backward is consistent with the input power scan in Figure 6.12, where SOLPS-ITER-backward is closer to SOLPS5.0 than to SOLPS-ITER. The maximum electron temperature at the outer target in SOLPS-ITER is ~10% lower than SOLPS-ITER-backward and the pressure ratios of target to upstream in SOLPS-ITER are lower than SOLPS-ITER backward, which means that the outer target is tlsmore detached.
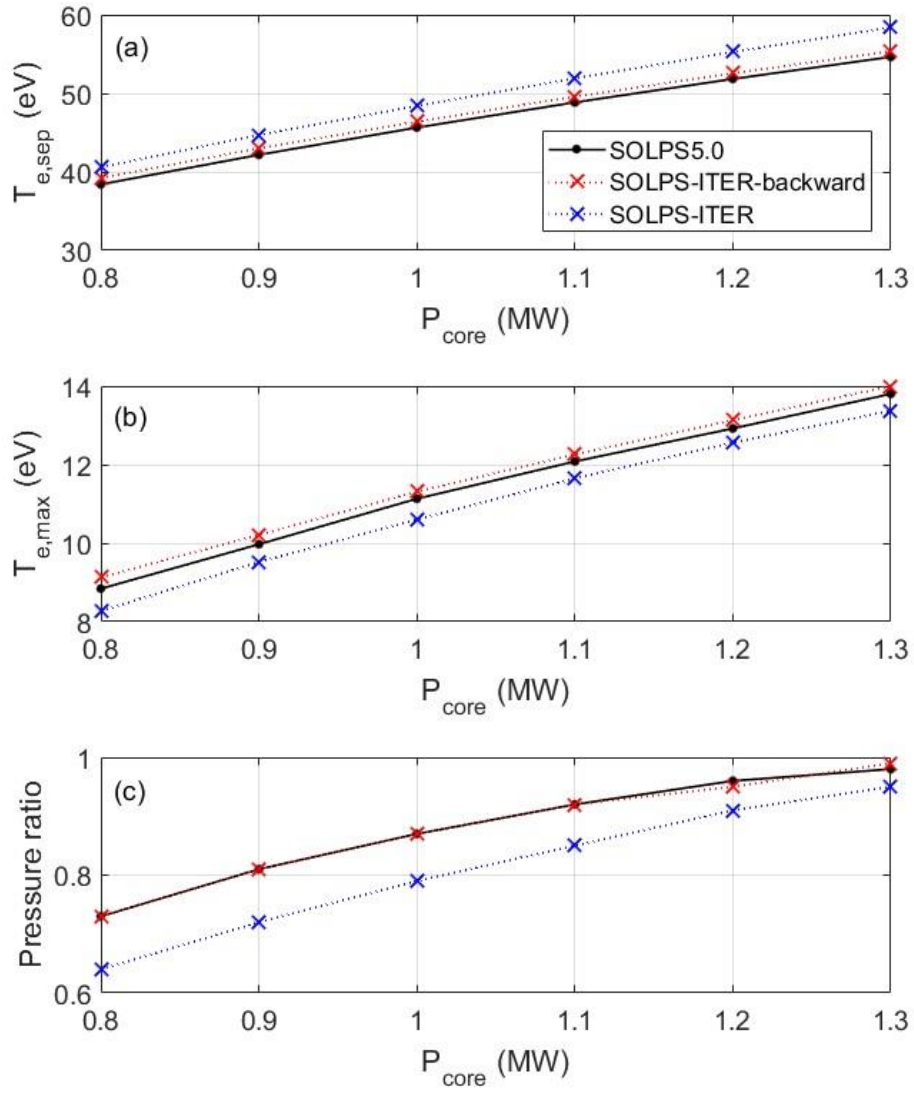
Figure 5.12 Input power scan for (a) Electron upstream temperature $T_{e,sep}$, (b) maximum electron temperature $T_{e,max}$ at the outer target, and (c) pressure ratio of outer target to upstream.

In this chapter, in order to use SOLPS-ITER to continue SOLPS5.0 modelling about ASDEX Upgrade L-mode detachment discharges, SOLPS-ITER has been instructed to mimic SOLPS5.0 physics to examine SOLPS-ITER backward compatibility including both fluid neutral and kinetic neutral models.

There is good agreement within ~5% of the simulation results between SOLPS-ITER and SOLPS5.0 with the neutral fluid model, except for the n_e profiles at outer target. For kinetic neutral models, in fixed gas-puff mode, there is ~20% difference in the n_e and T_e target profiles. In the feedback-controlled mode, with the same $n_{e,sep}$ the differences of targets profiles are reduced to ~10%. Such discrepancies are similar to previous benchmark activities [7] and are much smaller than the discrepancies between the modelling results and the experimental measurements; thus we believe that SOLPS-ITER has good compatibility with SOLPS5.0 from a practical point of view. Through a detailed comparison of the simulation results

between SOLPS-ITER-backward and SOLPS-ITER, we trust that the added SOLPS-ITER physics does not introduce unwanted spurious effects for pure deuterium simulations. For the kinetic neutral model in the fixed gas-puff mode, the recommended physics/numerics only produce ~5% differences of outer mid-plane and target profiles. A scan in upstream density ($n_{e,sep}$) covering from attached to detached conditions produced closely matching results within ~10% differences in all cases, and the roll-over of ion flux happens at about the same upstream density.

Chapter 6

SOLPS-ITER modelling results

6.1 Selected ASDEX Upgrade discharges

In this section, we briefly describe two selected ASDEX Upgrade L-mode discharges (#27100 and #34821), which are used to validate SOLPS-ITER modelling results.

Discharge #27100 is an L-mode density ramp discharge of ASDEX Upgrade, including three distinct detachment states: the onset of detachment, the fluctuating detachment state and the complete detachment state as mentioned in sections 2.3 and 2.4. In the phase of fluctuating detachment state of discharge #27100, the HFSHD region is observed in the inner divertor volume; A detailed description of detachment states in discharge #27100 is in references [35] [108]. Discharge #34821 is an L-mode discharge with fuelling steps aiming at repeating #27100 detachment states. Both discharges are in lower single null divertor configuration. The plasma currents I_p of the two selected discharges are 1MA. The toroidal forward magnetic field of the two selected discharges are 2.5T, so that the direction of $\vec{B} \times \nabla \vec{B}$ points towards the X-point and lower divertor. The time evolution of edge averaged electron density, gas puffing rate, radiation and heating power of the two selected discharges are shown in Figure 6.1.
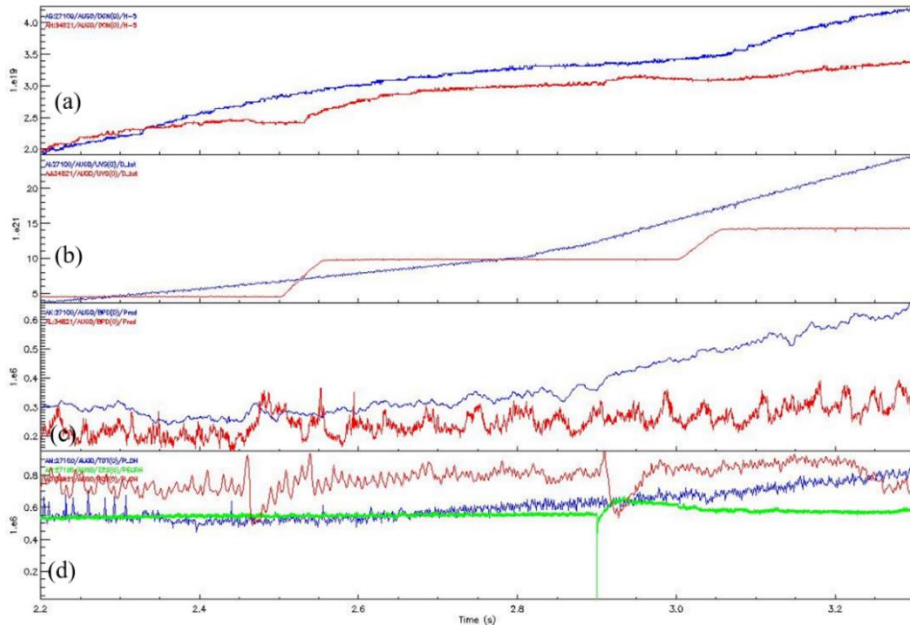
Figure 6.1 Time evolution of (a) edge line averaged electron density, (b) gas puffing rate, (c) radiation of main plasma (d) heating power for dischages #27100 and #34821.

Time points of #27100 and #34821 with corresponding electron density at the outer mid-plane separatrix $n_{e,sep}$ and detachment states are summarized in Table 6.1. The experimental data at such time points within 0.1s time window are selected to validate SOLPS-ITER modelling results.

Table 6.1 Divertor detachment states with corresponding electron density at outer mid-plane separatrix $n_{e,sep}$ and time point for #27100 and #34821.

Divertor detachment states	$n_{e,sep}$ ($\times 10^{19}$ m^{-3})	Time point for #27100	Time point for #34821
Onset of detachment	1.0	2.3s	2.3s
The fluctuating detachment state	2.0	2.8s	2.8s
The complete detachment state	2.2	3.05s	3.2s

SOLPS code package provides stationary solutions. For discharge #27100, we assume that plasma are steady state at the time points with 0.1s time window and ignore the changes of gas puffing value. For #34821 discharge, the gas puffing rate is constant at the time points with 0.1s time window; the plasma are steady state. In the fluctuating detachment state in #27100, the fluctuation band of radiation power near X-point is 5.5 kHz . There are also oscilations of plasma parameters on divertor targets in experiments [108], which means plasma is not a truely steady state in the fluctuating detachment state. In order to compare experimental data with SOLPS modelling results, the particle fluxes at divertor targets and electron density in inner divertor volume measured by Langmuir probes, which are used in section 6.3, are averaged values within 0.01s similar to [42]. The timescale of 0.01s is much larger than the timescale of fluctuating radiation ($\frac{1}{5.5\,\text{kHz}} = 2 \times 10^{-4}\,\text{s}$), thus the measured particle fluxes and electron temperature at divertor targets are approximate to steady state.

6.2 Modelling setup

In this chapter, SOLPS-ITER is used to model the onset of detachment state (OS), the fluctuating detachment state (FS), and the complete detchment state (CDS). The 96×36 computational grid of SOLPS-ITER used in this section is the same as the one in chapter 5. In order to validate against experimental data, the sub-divertor structures, including turbopump, cryopump and neutral baffles as [62][42], are considered. The pumping speed for cryopump is 100 m³/s and 14 m³/s for turbopump. The corresponding albedos of the pumping surfaces are 0.92 and 0.987, resepectively. The kotov-2008 model of atomic reactions [66] are used in EIRENE. It is impossible to simultaneously match the SOLPS-ITER modelling resutls and the experimental data about gas puffing rate Γ_{puff}, pumping speed Γ_{pump} and electron density at the outer mid-plane separatrix $n_{e,sep}$. Thus, the feedback controlled mode in SOLPS-ITER is used to exactly reproduce the experimental value of $n_{e,sep}$ [119]. Similar to [64], a perpendicular outward convective transport component in the low field side of scrape-off layer is used to mimic the convective

transport by filaments. The perpendicular transport coefficients are shown in Figure 6.2.
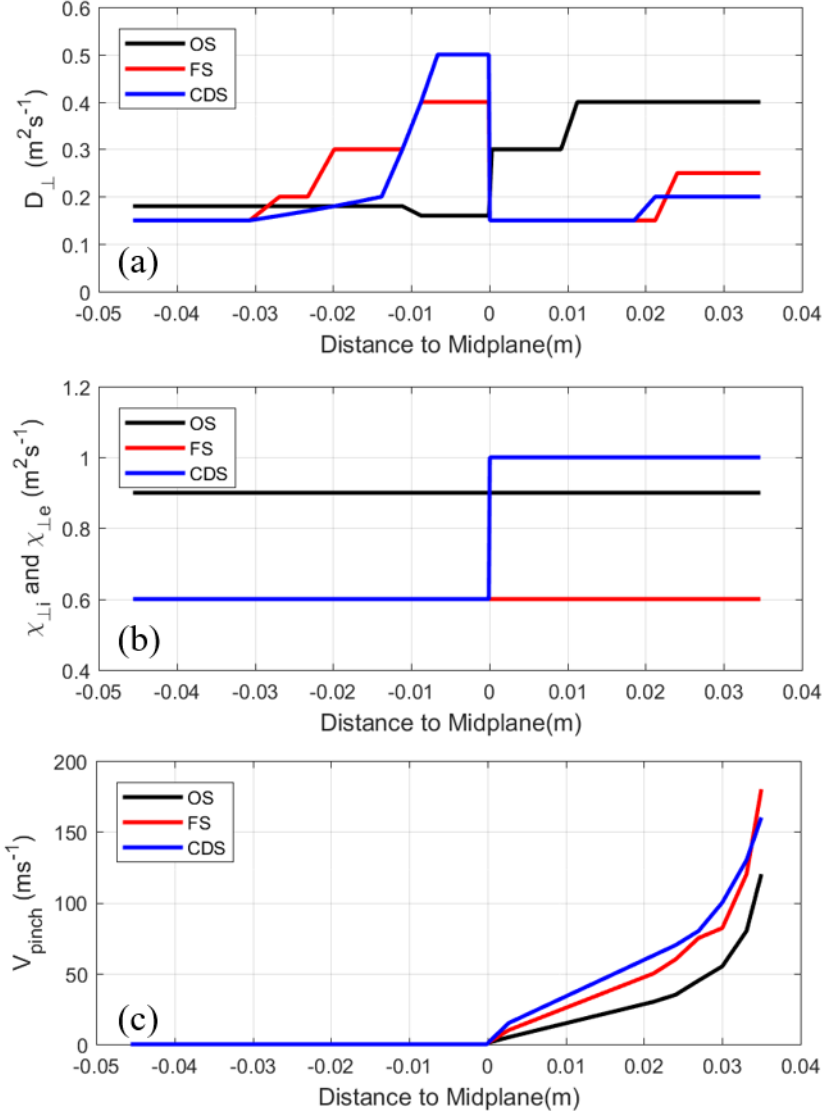
Figure 6.2 (a) Particle diffusive transport coefficient $D_\perp$, (b) electron and ion heat diffusive transport coefficient $\chi_{\perp i}$ and $\chi_{\perp e}$, and (c) convective pinch velocity V_{pinch} at the outer mid-plane for the modelling of the three detachment states. OS is for the onset of detachment, FS is for the fluctuating detachment state and the CDS is for the complete detachment state.

The $E \times B$ and diamagnetic drifts and all currents (parallel electric current, anomalous current, diamagnetic current, inertial current, ion-neutral current, current due to perpendicular and parallel viscosity, current due to viscosity tensor) in SOLPS-ITER are considered. The speed-up scheme of particle flux surface averaging method [122] is used to reduce CPU running time. The drifts-compatible boundary conditions [123] are used. The input power across the core boundary is estimated to be 0.8 MW according to the total heating power substracts the radiation power in core plasma which is in Figure 6.1, and is equally distributed to ions and electrons. The particle flux across the core boundary is 5×10^{20} s^{-1} to mimic neutrals penetrating deep in the core, ionizing and then coming back towards the plasma

edge. Sheath boundary conditions at the targets and leakage wall boundary conditions with a factor of 0.01 both for density and energy are used.

6.3 Modelling results

The modelled and measured electron density n_e and electron temperature T_e profiles at the outer mid-plane during three detachment states are shown in Figure 6.3. Measured electron density comes from Thomson scattering (TS) and Integrated data analysis (IDA) and measured electron temperature are provided by Thomson scattering (TS) and Electron cyclotron emission (ECE) measurements. In feedback controlled mode, the electron density at the outer mid-plane separatrix $n_{e,sep}$ is prescribed to exactly match the experimental values. Through adjusting the transport coefficients, especially in the core region near separatrix, there is a reasonable match of n_e between modelling results and experimental data. For the onset of detachment and the fluctuating detachment states, the modelling results of T_e in the core region near separatrix is higher than the ECE measurements but within the range of TS mesurements.
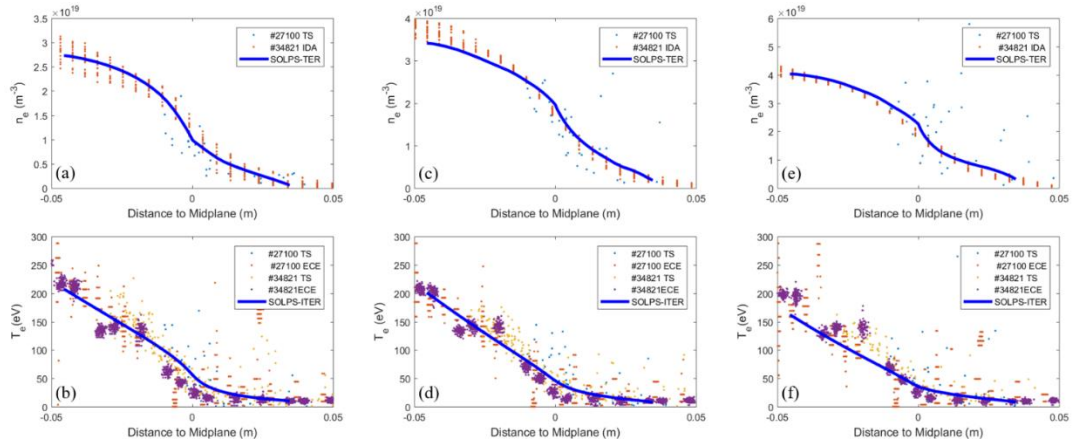
Figure 6.3 The measured and modeled electron density n_e and T_e profiles at the outer mid-plane. (a) and (b) are for the onset of detachment state, (c) and (d) are for the fluctuating detachment state, (e) and (f) are the complete detachment state. Measured electron density are taked from Thomson scattering (TS) and Integared data analysis (IDA) , measured electron temperature are from Thomson scattering (TS) and Electron Cyclotron Emission (ECE).

In SOLPS-ITER, the radial particle flux is

$$\tilde{\Gamma}_{ay} = \left(V_{ay}^{(E)} + V_{ay}^{(AN)}\right)n_a + \frac{1}{e}\left(j_y^{(AN)} + j_y^{(in)} + \tilde{j}_y^{(vis\|)} + \tilde{j}_y^{(vis\perp)} + \tilde{j}_y^{(visq)}\right)$$
$$- D_{n,a}\frac{1}{h_x}\frac{\partial n_a}{\partial y} + \tilde{\Gamma}_{ay}^{(dia)} \tag{5.2}$$

$V_{ay}^{(E)}n_a$ and $\tilde{\Gamma}_{ay}^{(dia)}$ are due to $E \times B$ and diamagnetic drifts. $\frac{1}{e}\left(j_y^{(AN)} + j_y^{(in)} + \tilde{j}_y^{(vis\|)} + \tilde{j}_y^{(vis\perp)} + \tilde{j}_y^{(visq)}\right)$ are the contributions from the currents. In

SOLPS-TER, the particle flux due to currents is only considered in the radial direction, not in the poloidal direction. $-D_{n,a}\frac{1}{h_x}\frac{\partial n_a}{\partial y}$ is the diffusive term and $V_{ay}^{(AN)}n_a$ is the convective transport part which we employ to mimic convective transport by filaments similar to published work in [42]. The profiles of radial particle fluxes along the outer mid-plane are presented in Figure 6.4.
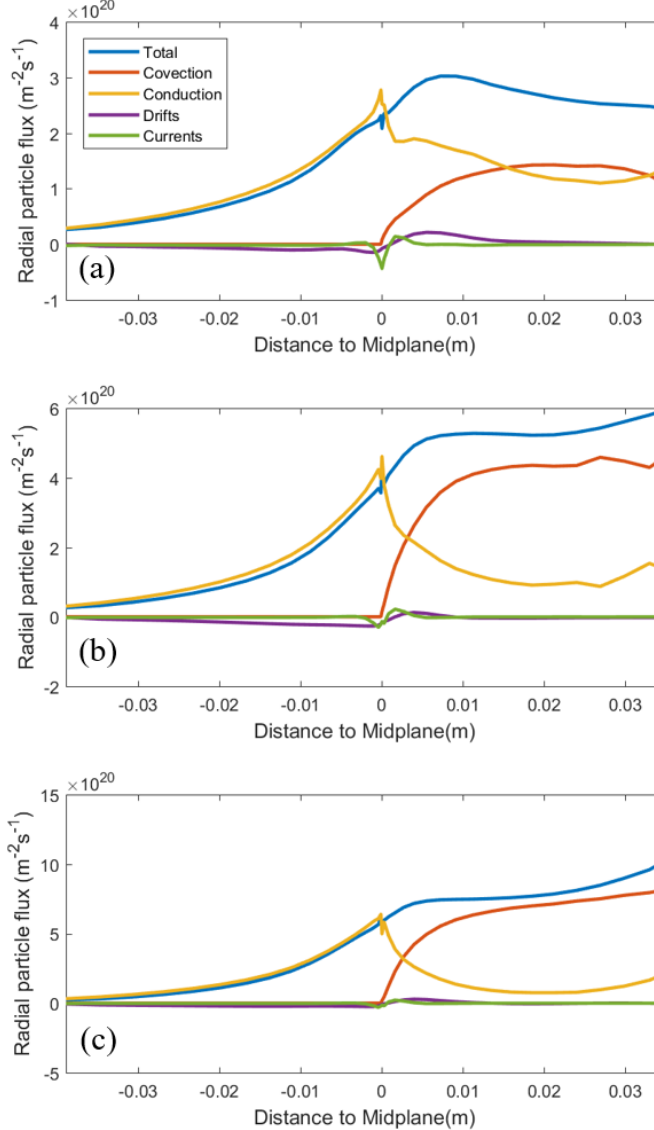
Figure 6.4 Modelled radial particle fluxes along the outer mid-plane for (a) the onset of detachment state, (b) the fluctuating detachment state and (c) the complete detachment. We show total particle flux, and the individual contributions: particle flux due to conduction, particle flux due to convection, particle flux driven by drifts and particle flux due to currents.

For all three detachment states in our modelling, the radial particle fluxes due to drifts and currents are minor compared to convection and diffusion. The convection particle flux for the three detachment states modelling are $\sim 1\times10^{20}$ m^{-2}s^{-1}, $\sim 4\times10^{20}$ m^{-2}s^{-1} and $\sim 8\times10^{20}$ m^{-2}s^{-1} in the far SOL region, respectively. For the modelling fluctuating and the complete detachment states, the convective transport

is dominant in the far SOL region, resulting in an increase of particle flux across wall boundary and a decrease of particle fluxes to the divertor targets.

The modelling results of particle flux Γ_{ion} and electron temperature T_e profiles at the inner and outer targets are compared with Langmuir probe measurements. Results without considering drifts are also presented to investigate their effect close to the targets. For the onset of detachment state, there is a good agreement of peak value of particle flux at inner targets (with drift) which is shown in Figure 6.5. While for the value of Γ_{ion} at inner target between -10cm ~ -5cm, the modelling result are lower than the experimental value by a factor of 2. The discrepancy of particle flux profiles at the inner target between modelled and measured values in previous study [63] are reduced.
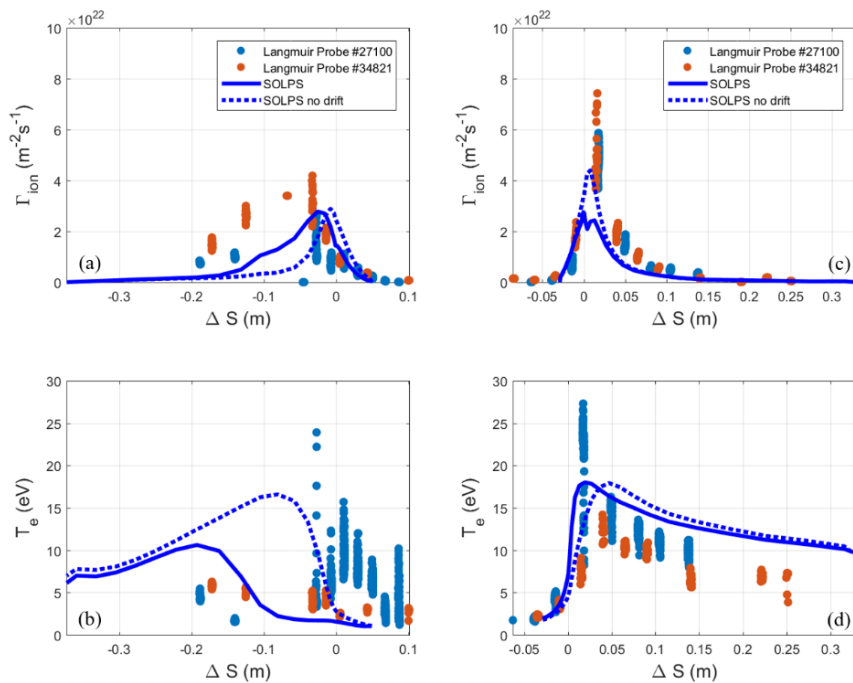
Figure 6.5 Comparison between measured and modeled value of (a) ion flux Γ_{ion} at the inner target, (b) electron temperature T_e at the inner target, (c) ion flux Γ_{ion} at the outer target, (d) electron temperature T_e at the inner target for onset of detachment state. Both #27100 and #34821 are presented. Solid lines are for cases with drifts, and dashed lines are for cases without drift.

For the peak value of particle flux at the outer target, the modeling result is lower than experimental data within a factor of 2. The drifts results in the integrated particle flux Γ_{int} at the inner flux increase and decrease at the outer target at the onset of detachment state for the onset of detachment as shown in Table 6.2.

Table 6.2 Modelling result of integrated particle flux Γ_{int} ($\times 10^{22}$ s^{-1}) with and without drifts at the inner and outer targets for the onset of detachment state.

	Γ_{int} at the inner target	Γ_{int} at the outer target
With drifts	2.4	1.5
Without drifts	1.5	1.9

Electron temperature T_e profiles at the targets for the onset detachment state are in Figure 6.5. With drifts, the observed in-out asymmetry of T_e in experiments is reproduced in our modelling that the peak value of T_e at the inner target is ~10eV at about Δ20cm, while at the outer target it is ~20eV near strike point. A physical explanation is that the radial $E \times B$ drift transports particles from the outer divertor region to private flux region and from private flux region to inner divertor region [63][120]. As the increase of ion density, a recombination front is formed close to the inner target strike point. Thus, the electron temperature at the inner divertor near the strike point decreas below 2eV. There is still discrepancy between modelling results and experimental data at ΔS from 0 to 5cm at the inner target, whose reason is still unclear now.

For the modelling of the fluctuating detachment state, there is a good agreement between modelling results and experimental data for particle flux Γ_{ion} profiles at the inner target, as shown in Figure 6.6. The discrepancy shown by SOLPS 5.0 modelling results of particle flux at the inner target in previous study [63] are reduced. As for the particle flux at the outer target, both the total and peak value of modelling results are lower than experimental data by a factor of ~3, similar to previous SOLPS5.0 results [63]. By comparing the modelling results between with drifts and without drifts, it can be found that the drifts do not change dramaticaly the particle flux profiles at both inner and outer targets for the fluctuating detachment state.

For electron temperature T_e profiles at the inner target in Figure 6.6, the modeled value are about ~2 eV and lower than experimental data especially near the strike point, where the measured value is ~15eV in discharge #27100. This shows that modelling predicts the inner divertor to be detached, while experiments in discharge #27100 shows a region attached close to the strike point; this is unlikely to be a measurement error and we cannot explain it at the moment. At the outer target, there is a good agreement of electron temperature T_e profiles. In the fluctuating detachment state, the inner divertor is detached and the outer divertor is in the high recycling regime. This is successfully reproduced by SOLPS-ITER modelling.
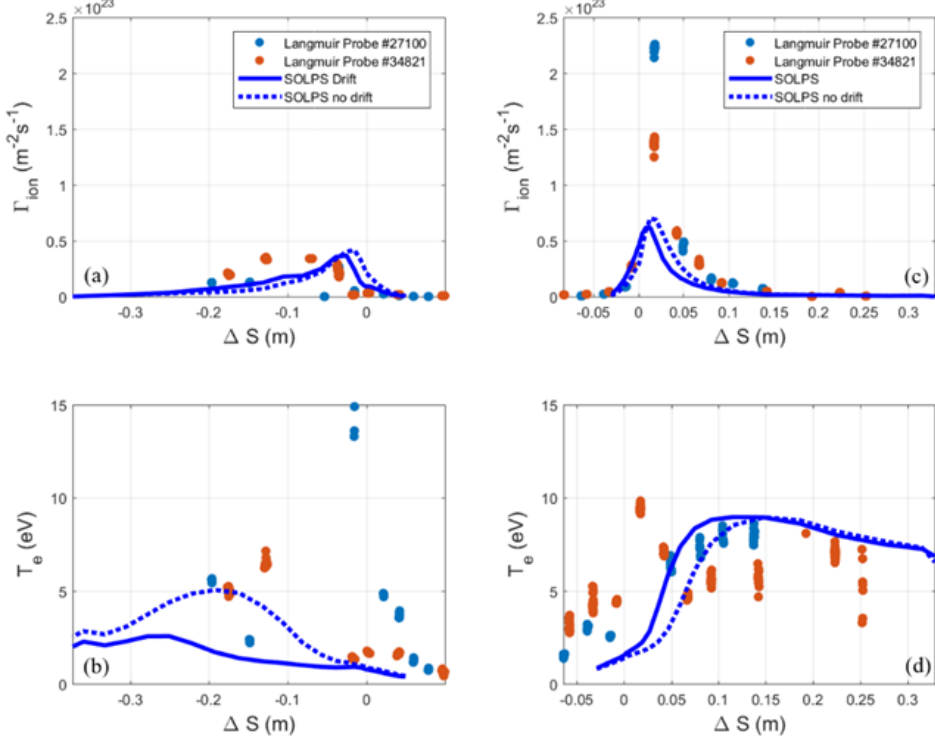
Figure 6.6 Comparison between measured and modeled value of (a) ion flux Γ_{ion} at the inner target, (b) electron temperature T_e at the inner target, (c) ion flux Γ_{ion} at the outer target, (d) electron temperature T_e at the outer target for the fluctuating detachment state. Both #27100 and #34821 are presented. Solid lines are for cases with drifts, and dashed lines are for cases without drifts.

For the complete detachment state modelling, both inner and outer targets are detached in experiments. There is a good agreement of particle flux profiles at both the inner and outer targets as in Figure 6.7. For electron temperature T_e profiles, similar to the modelling of the fluctuating detachment state, the modelled electron temperature are lower than experimental data near strike point at both the inner and outer targets. The modelled peak value of particle flux Γ_{ion} at the outer target is lower the value in fluctuating detachment modelling. The modelled peak value of electron temperature is ~8 eV in the far SOL region. The complete detachment states are succeffully reproduced by SOLPS-ITER. Comparing the modelling results between with and without drifts, it can be found that the changes of particle flux Γ_{ion} due to drifts are ~within 5%.
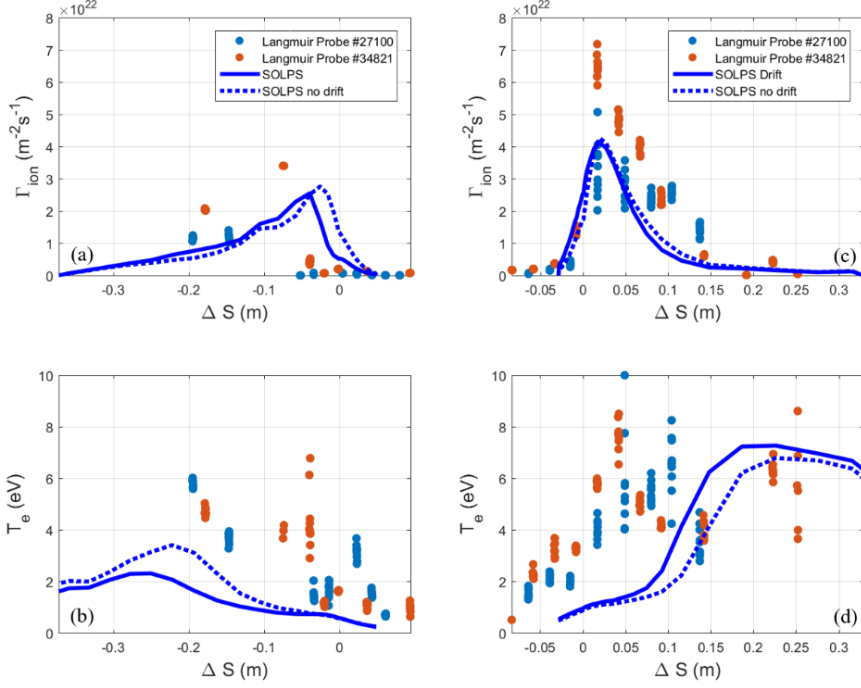
Figure 6.7 Comparison between measured and modeled value of (a) ion flux Γ_{ion} at the inner target, (b) electron temperature T_e at the inner target, (c) ion flux Γ_{ion} at the outer target, (d) electron temperature T_e at the outer target for the complete detachment state. Both #27100 and #34821 are presented. Solid lines are for cases with drifts, and dashed lines are for cases without drifts.

Based on the modelling of the fluctuating detachment state, a parameter scan of electron density at the outer mid-plane separatrix $n_{e,sep}$ is performed for both with and wihtout drifts under same perpendicular transport coefficients. First, for drifts cases, feedback-controlled mode is used to ensure the $n_{e,sep}$ are from 1.0×10^{19} m^{-3} to 3.0×10^{19} m^{-3} with 0.1×10^{19} m^{-3} interval. Then the corresponding gas puffing rates are used for without drifts cases to eliminated the effect due to different deuterium fueling rate. The results are summarized in Figure 6.8.

As the gas puffing rate increases, $n_{e,sep}$ increases similarly both for with and without drifts cases. However, for drifts cases the increase of $n_{e,sep}$ is a bit steeper, so that at low puffing rates it is lower than the corresponding without drifts runs, and becomes slightly higher at high puffing rates. The turning point is at a puffing level of 4.35×10^{21} s^{-1}.
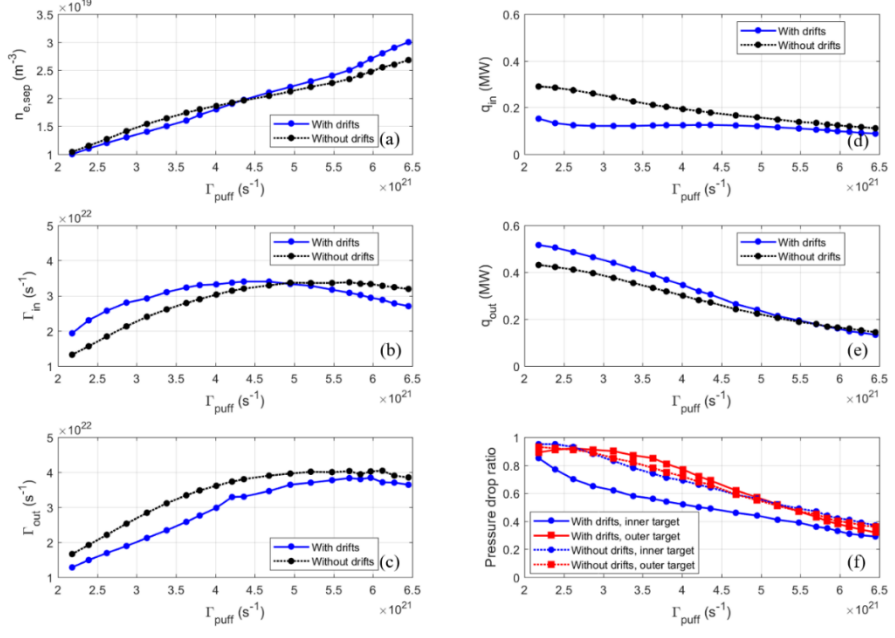
Figure 6.8 Modelling results of a upstream density scan based on the modelling of the fluctuating detachment state. (a) Electron density at the outer mid-plane separatrix $n_{e,sep}$ as a function of gas puffing rate, (b) integrated ion flux at inner target Γ_{in} as a function of gas puffing rate, (c) integrated ion flux at the outer target Γ_{out} as a function of gas puffing rate. (d) integrated heatflux at the inner target q_{in} as a function of gas puffing rate, (e) integrated heat flux at the outer target q_{out} as a function of gas puffing rate, (f) presurre drop at inner and outer targets as a function of gas puffing rate. Both with and without drifts are considered.

For the integrated particle flux at the inner target Γ_{in}, with drifts, the roll-over occurs when the gas puffing rate is 4.35×10^{21} s^{-1}. Without drifts, the roll-over occurs when the gas puffing rate is 5.6×10^{21} s^{-1}. At the outer target, the roll-over of integrated particle fluxes Γ_{out} occurs at the same level of gas puffing rate for both with and without drifts cases, but the particle fluxes with drifts are ~10% lower than without drifts cases. This is because drifts shift particles from the outer divertor region to the inner divertor region. As a consequence of the increase of the particle flux at the inner target, the inner target detached 'earlier' than the outer target, when the outer target is in the high recycling regime. This is consistent with the electron temperature distribution in Figure 6.9. With drifts, in front of the inner target, electron temperautre is about 2~5 eV means that a recombination front exists. Without drifts, the distributions of electron temperature at the inner and outer targets are similar.
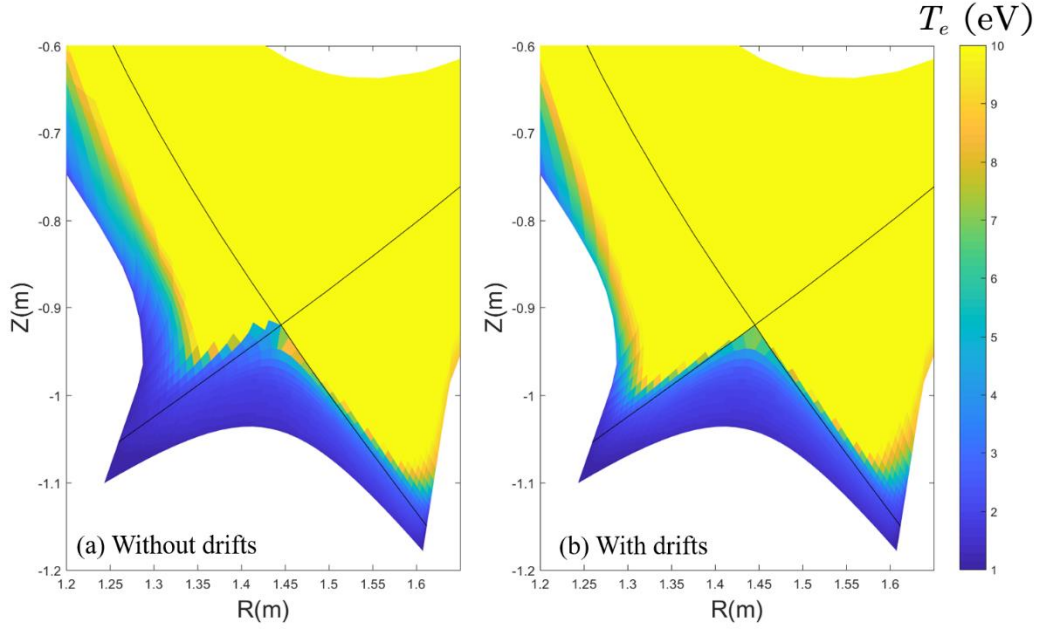
Figure 6.9 Distributions of electron temperature in the divertor region for the modelling of the flutuating detachment state: (a) is with drifts and (b) is without drifts.

The poloidal and radial particle fluxes due to $E \times B$ drift are

$$\Gamma_x^{(E \times B)} = V_x^{(E)} n_e = -\frac{B_z}{B^2} \frac{1}{h_y} \frac{\partial \phi}{\partial y} n_e$$

$$\Gamma_y^{(E \times B)} = V_y^{(E)} n_e = -\frac{B_z}{B^2} \frac{1}{h_x} \frac{\partial \phi}{\partial x} n_e \quad (5.3)$$

The poloidal and radial effective fluxes driven by diamagnetic drift are

$$\Gamma_x^{(dia)} = -D_{axy} \frac{1}{h_y} \frac{\partial n_a T_i}{\partial y} = \left(\frac{1}{B^2} - \frac{1}{\langle B^2 \rangle} \right) \frac{B_z}{e} \frac{1}{h_y} \frac{\partial n_a T_i}{\partial y}$$

$$\Gamma_y^{(dia)} = -D_{ayx} \frac{1}{h_x} \frac{\partial n_a T_i}{\partial x} = \left(\frac{1}{B^2} - \frac{1}{\langle B^2 \rangle} \right) \frac{B_z}{e} \frac{1}{h_y} \frac{\partial n_a T_i}{\partial y} \quad (5.4)$$

The radial particle flux due to currents is

$$\Gamma_y^{(j)} = \frac{\left(j_y^{(AN)} + j_y^{(in)} + \tilde{j}_y^{(vis\|)} + \tilde{j}_y^{(vis\perp)} + \tilde{j}_y^{(visq)} \right)}{e} \quad (5.5)$$

The distribution of contributions from $E \times B$ drift, diamagnetic drift and currents to the radial particle flux in the modelling of fluctuating detachment are in Figure 6.10. Compared to the contribution from the $E \times B$ drift, the contributions of diamagnetic drift and currents can be neglected. We believe that the main

mechanism shifting plasma from outer divertor region to inner divertor region is the $E \times B$ drift [].
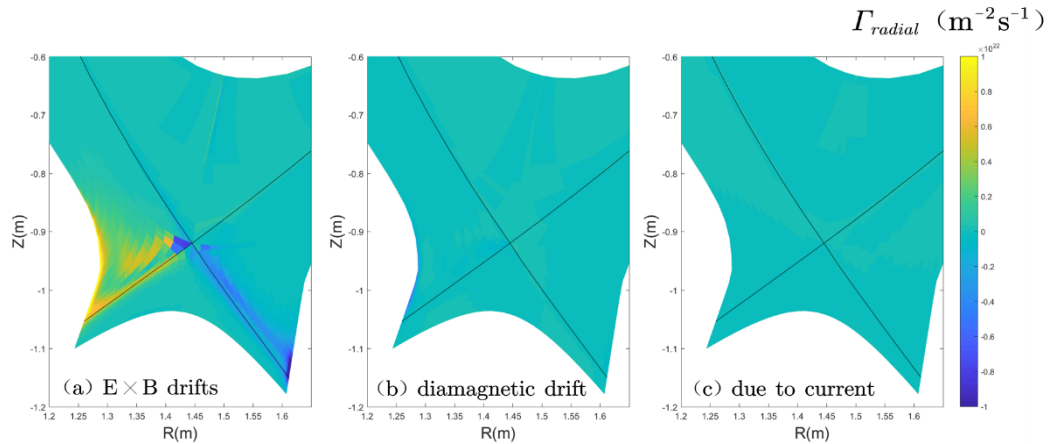
Figure 6.10 Distributions of radial particle fluxes in the divertor region for the modelling of the flcutuating detachment state. (a) is the contributions due to E×B drift, (b) is the contributions due to diamagnetic drift and (c) is the contributions due to currents.

For the integrated power flux at the inner target q_{in} in Figure 6.8, it decreases first from 0.152MW to 0.12MW, then stays almost constant until the roll-over of integrated particle flux, and finally decreases. Without drifts, there is no such trend, and the value is much higher than drifts cases. For the power flux at the outer target q_{out}, both with and without drifts decrease as the gas puffing rate increases. It looks like the drifts 'transfer' power from inner divertor to outer divertor which is opposite to particle flux. Unfortunately, we cannot explain it now. In the future, the effect of drifts to the power flux will be presented. For the pressure drop ratio without drifts, the value is almost the same at both the inner and outer targets. With drifts, the pressure drop ratio at the inner target are lower than at the outer target, which means the inner target is more detached than the outer target and can be responsible for the in-out asymmetry of electron temperature.

We also compared the neutral flux density at dome and pump gauges as in Table 6.3. For the neutral flux density at dome, it can be seen that the discrepancy between modelled and measured value are within ~30%. For the neutral flux density at pump gauge, the modelled value are ~30% higher than experimental value. The discrepancy of neutral flux density and neutral compression ratio in previous publication [63] is also reduced.

Table 6.3 The measured/modelled values of neutral flux density ($\times 10^{21}\text{m}^2/\text{s}^{-1}$) at dome and pump gauges and the ratio of neutral flux densities between these two value. The experimental data are from discharge #34821. The value at dome are measured by F04 gauge and the value at pump are measured by F05 gauge.

Detachment state	Dome	Pump	Ratio
Onset of detachment	18/15	2.0/2.7	9.0/5.6
The fluctuating detachment state	60/45	6.3/7.8	9.5/5.8
The complete detachment state	90/53	7.5/9.8	12.0/5.4

6.3 Effect of radial convective transport

In this study, we assume that the convectivet transport by filaments is mimicked through a radial convective velocity. In experiments, as the upstream density increases, the perpendicular partcile flux density related to filaments transport increases [124]. Thus, the radial convective velocity (pinch velocity) used in the modelling of the fluctuating detachment and the complete detachment states are higher than the value in the modelling of the onset of detachment. In order to explore the effect of the radial convective velocity on the plasma parameters, a parameter scan of the radial convective velocity is performed, where we vary it by means of a scaling factor. Based on the modelling of the fluctuating detachment and the complete detachment states, the scaling factor for pinch velocity ranges from 0 to 1.0 with 0.2 interval.
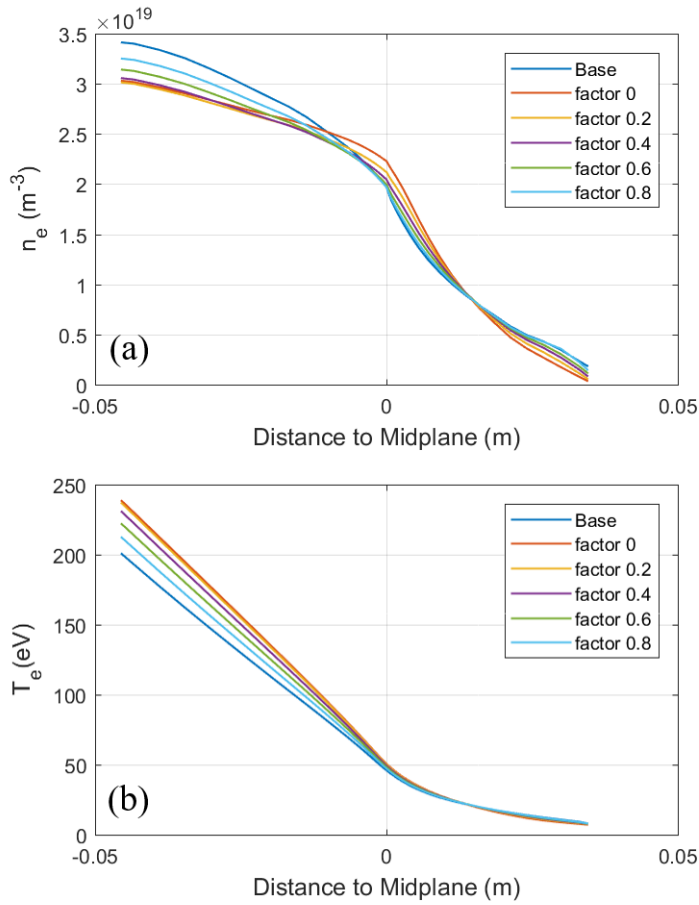
Figure 6.11 Modelling results of radial convective velocity scan based on the modelling of the fluctuating detachment state. (a) is the electron density n_e profiles at the outer mid-plane, (b) is the electron temperature T_e profiles at the outer mid-plane.

The electron density n_e and electron temperature T_e profiles at the outer mid-plane for the radial convective velocity scan are shown in Figure 6.11. As the radial convective velocity increases, electron density n_e is increased in SOL region near separatrix and decreased in the far SOL region. In the core region, strange behaviour is observed which is unclear now. For electron temperature T_e profiles at the outer mid-plane, as the pinch velocity increases, the electron temperature

decreases. For the complete detachment state, similar trends about density and temperature profiles can be observed, as shown in Figure 6.12.
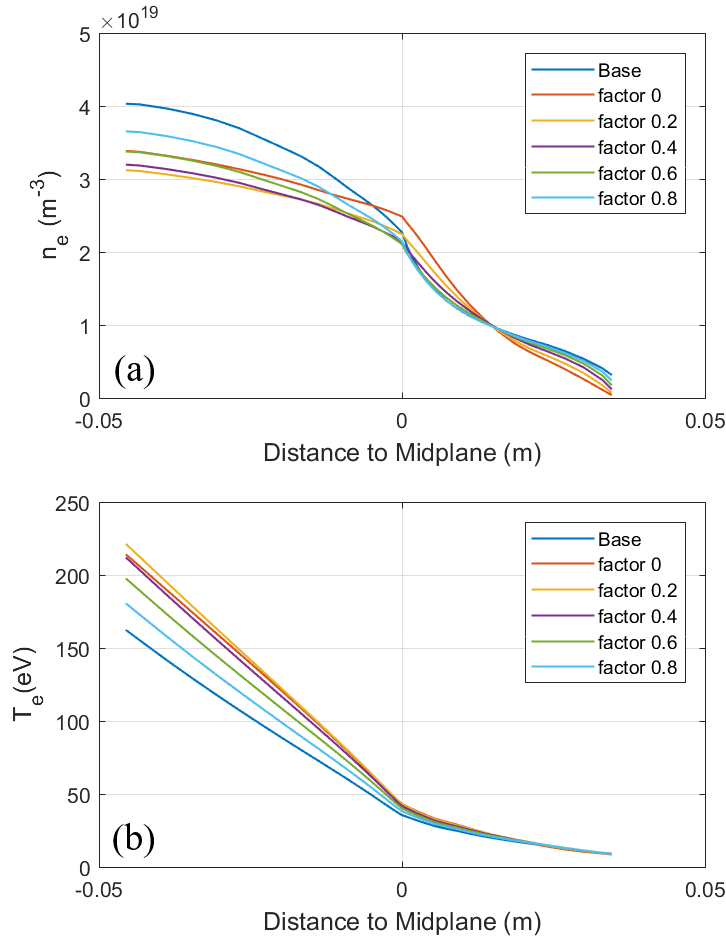
Figure 6.12 Modelling results of radial convective velocity scan based on the modelling of the complete detachment state. (a) is the electron density n_e profiles at the outer mid-plane, (b) is the electron temperature T_e profiles at the outer mid-plane.

For the peak value of particle flux profiles at both the inner and outer targets in the fluctuating detachment state, as the radial convective velocity decreases, particle fluxes increase about ~30% as shown in Figure 6.13. This is because the decrease of the radial convective velocity leads to the decrease of integrated particle flux through the wall boundary that increases particle fluxes at targets from a view of particle balance. For the peak value of electron temperature T_e, it decreases at the inner target and increase at the outer target. For the complete detachment state which is shown in Figure 6.14, there is similar behaviour: the particle flux at the inner and outer targers increase as the radial convective velocity decreases.
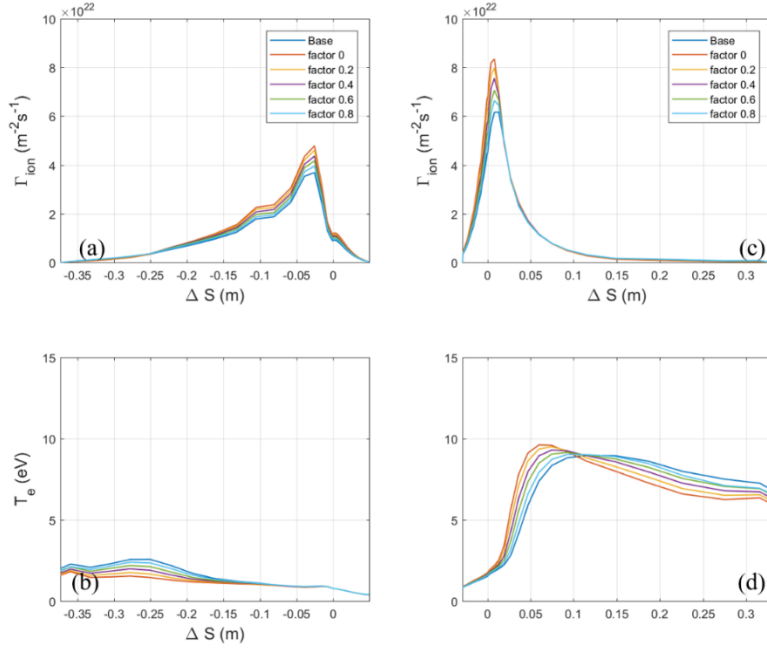
Figure 6.13 Modelling results of radial convective velocity scan based on the modelling of the fluctuating detachment state. (a) is the particle flux Γ_{ion} profiles at the inner target, (b) is the electron temperature T_e profiles at the inner target, (c) is the particle flux Γ_{ion} profiles at the outer target and (d) is the electron temperature T_e profiles at the outer target.
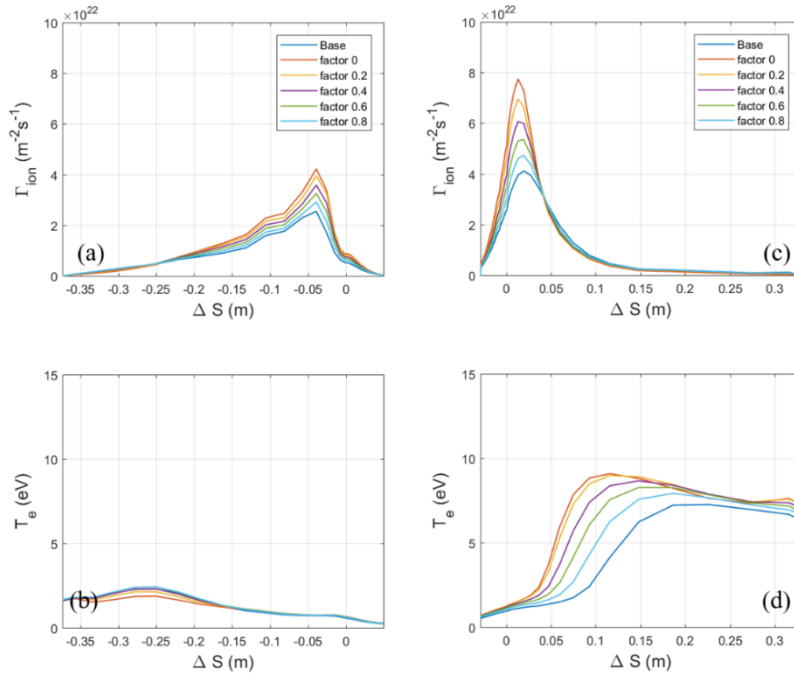
Figure 6.14 Modelling results of radial convective velocity scan based on the modelling of the complete detachment state. (a) is the particle flux Γ_{ion} profiles at the inner target, (b) is the electron temperature T_e profiles at the inner target, (c) is the particle flux Γ_{ion} profiles at the outer target and (d) is the electron temperature T_e profiles at the outer target.

The electron density in the inner divertor volume is measured through the spectroscopic line-of-sight (LOS) which is shown in Figure 3.3. The corresponding modeled and measured volume electron density for the fluctuating detachment and the complete detachment states are shown in Figure 6.15.

For the fluctuating detachment state modelling, the modelled electron density matches qualitatively the experimental data within a factor of 2, except the value along RIV group of divertor spectroscopy, which the LOS index is 1~5. The discrepancy in previous SOLPS5.0 study [63] is reduced. For the measurements of ZIV group of divertor spectroscopy (LOS index 6~12), it can been seen that as the scaling factor increases, the modeled value decreases about ~20% and matches better with experimental data.

For the modelling of the complete detachment state, the measured electron density along RIV group is about 5×10^{19} m^{-3}, while the modeled value decreases form ~4.5×10^{20} m^{-3} to ~3.5×10^{20} m^{-3} as the convective velocity increases. In experiments, the electron density measured by RXV group (LOS index 19~25) of divertor spectroscopy is almost an order of magnitude higher than the value measured by RIV group (LOS index 1~5). This characteristic is not reproduced in the modelling of the complete detachment state.
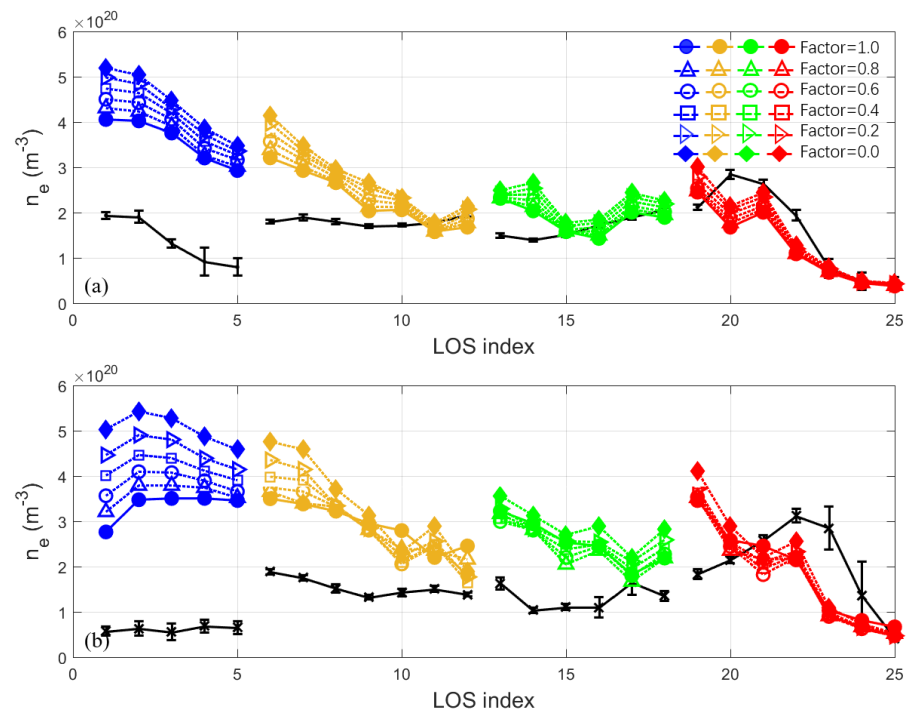
Figure 6.15 Modelled and measured volume electron densities n$_e$ along line of sight for (a) the fluctuating detachment state and (b) the complete detachment state.

6.4 Effect of boundary conditions

In SOLPS modelling activity, in order to solve the particle, momentum, and energy conservation equations, boundary conditions are provided by users. Boundary conditions are important to match experimental data. Some boundary condidions can be derived from experiments, e.g. the input power across the core boundary, which can be derived from the total heating power minus the radiation power in the core plasma. Some boundary conditions are from previous experiences, e.g. the leakage boundary conditions for particle and ion/electron energy at wall boundary. In [32], the effect of different boundary conditions is disccuessed for SOLPS5.0 H-mode modelling. Similar to that, in this section, the effect of different boundary conditions to numerical solutions are presented which is based on the modelling of the fluctuating detachment state. In this section, the modelling results of the fluctuating detachment state is selected as a basis. This is because the discrepancy of particle flux at outer target between experimental data and simulation results are obvious. We want to explore whehter such discrepancy is come from boundary condistions in our modelling or not.

6.4.1 Input power

In this study, the input power through the core boundary is 0.8MW as mentioned in sections 5.1 and 6.2. On the one hand, in SOLPS modelling, the computational grid include part of core plasma (5 cm), thus the indeed value should be higher than 0.8MW. On another hand, due to the error of measurements, the correct power is not exactly known. Thus, we perform a scan on the input power from 0.96MW (20% higher) to 0.64MW (20% lower).
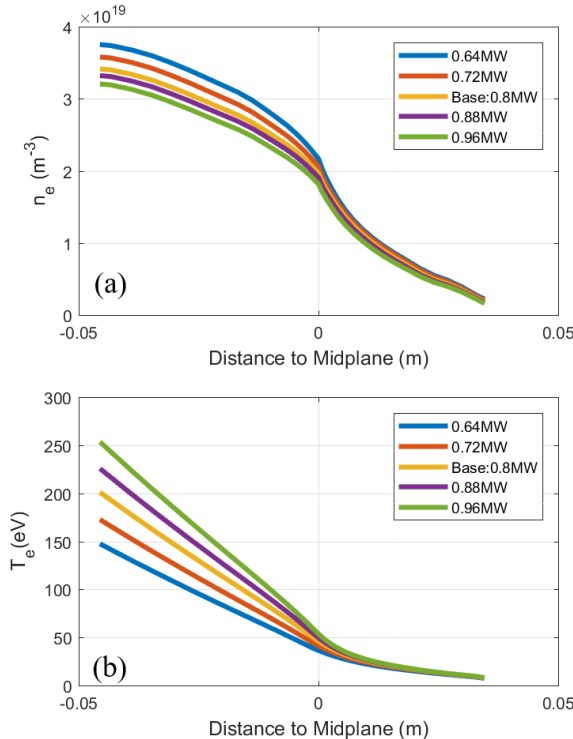

Figure 6.16 Modelling results of input power scan based on the modelling of the fluctuating detachment state. (a) is the electron density n_e profiles at the outer mid-plane, (b) is the electron temperature T_e profiles at the outer mid-plane.

Figure 6.16 shows electron density n_e and electron temperature T_e profiles at the outer mid-plane. The input power of 0.8 MW is coresponding to the modelling of the modelling of the fluctuating detachment state. It can be seen that without any other changes, as the input power increase from 0.64MW to 0.96MW, the electron temperature at the outer mid-plane separatrix $T_{e,sep}$ increases from 37 eV to 53 eV and the electron density at outer mid-plane separatrix $n_{e,sep}$ decreases from 2.16×10^{21} m^{-3} to 1.82×10^{21} m^{-3}. The increase of electron tempeature is easy to understand because of the increases of input power. In this study, the particle flux is prescribed. The decreased density is due to the momentum conservation equation.
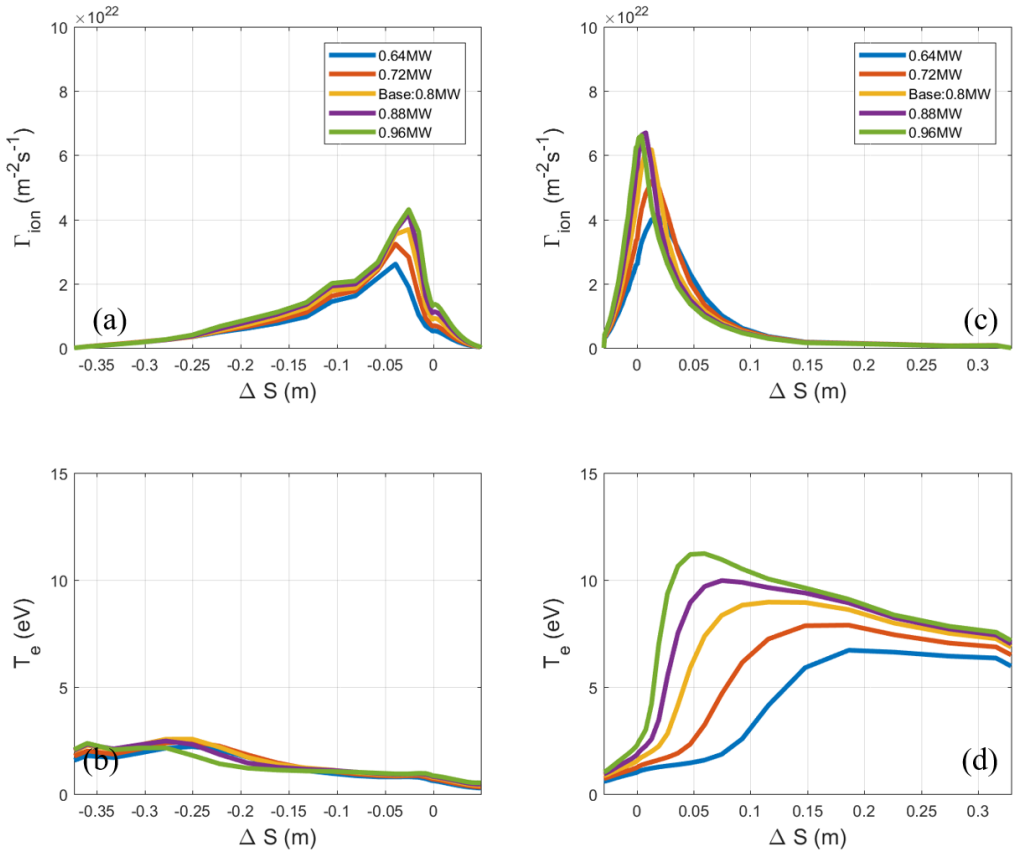
Figure 6.17 Modelling results of input power scan based on the modelling of the fluctuating detachment state. (a) is the particle flux Γ_{ion} profiles at the inner target, (b) is the electron temperature T_e profiles at the inner target, (c) is the particle flux Γ_{ion} profiles at the outer target and (d) is the electron temperature T_e profiles at the outer target.

Figure 6.17 shows the particle flux Γ_{ion} and electron temperature T_e profiles at the inner and outer targets. For the particle fluxes at the inner target, as input power increases, the particle flux increases. For the particle flux at the outer target, it also increases as input power increases. But, it can been seen, the particle flux profiles expands with lower input power which is not observed at the inner target. For electron temperature profiles at the inner target, even with different input power, they are at same level: 2-3 eV. For the electron tempeature at the outer target, as input power increases, the peak value decreases from 12 eV to 6 eV. This means

that the outer target are more detached as the power decreases. Even with 20% higher input power, the peak value of particle flux at the outer target is almost the same. This value is still much lower than the experimental value as mentioned in section 6.3 ($\sim 2 \times 10^{23} \, \text{m}^{-3}\text{s}^{-1}$).
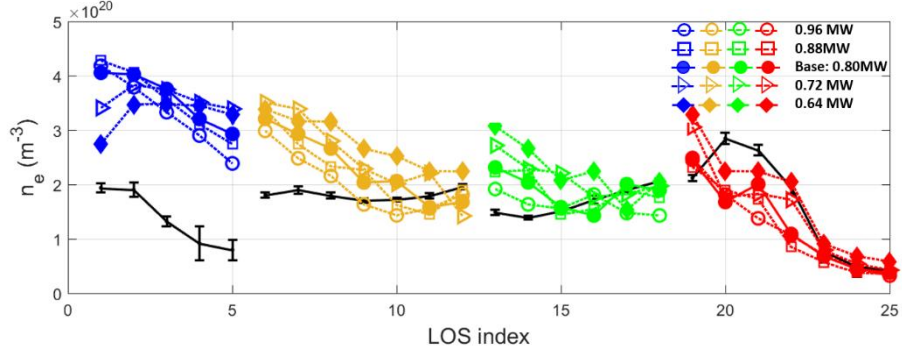
Figure 6.18 Modelled and measured electron densities n_e along line of sight with different input power.

In Figure 6.18, the electron density in inner divertor volume with different input power are shown. Compared to the basic fluctuating detachment modelling, the differnces are within 30%. Even with lower input power, the discrepancy about RIV group of divertor spectroscopy still exists.

6.4.2 Particle flux across the core boundary

In this study, the particle flux across the core boundary is 5×10^{20} s^{-1} to mimic neutrals penetrating deep into the core, ionizing and then coming back towards the plasma edge. The reason why not directly using 'eirene_ionising_core' swtich in SOLPS-ITER is that this switch conflicts with the new drifts model in SOLPS-ITER, with which we need to use drift-compatible boundary conditions. In order to investigate the effect of particle flux acorss the core boundary, another two value (1×10^{20}s^{-1} and 1×10^{21}s^{-1}) are considiered without any other changes. The cases with 1×10^{20}s^{-1} and 1×10^{21}s^{-1} are referred as low paticle flux and high particle in the fowllowing.

The electron density n_e and electron temperature T_e profiles at the outer mid-plane are shown in Figure 6.19. For the low particle flux case, the electron density at the outer mid-plane separatrix $n_{e,sep}$ is 1.7×10^{19} m^{-3}, for the high particle flux case, the coresponding value is 2.2×10^{19} m^{-3}. For electron temperature profiles, as particle flux across the core boundary increases, the temperature decreases in the core region. In the SOL region, even with different value of particle flux cross the core boundary, the electron temperature stays almost unchanged.
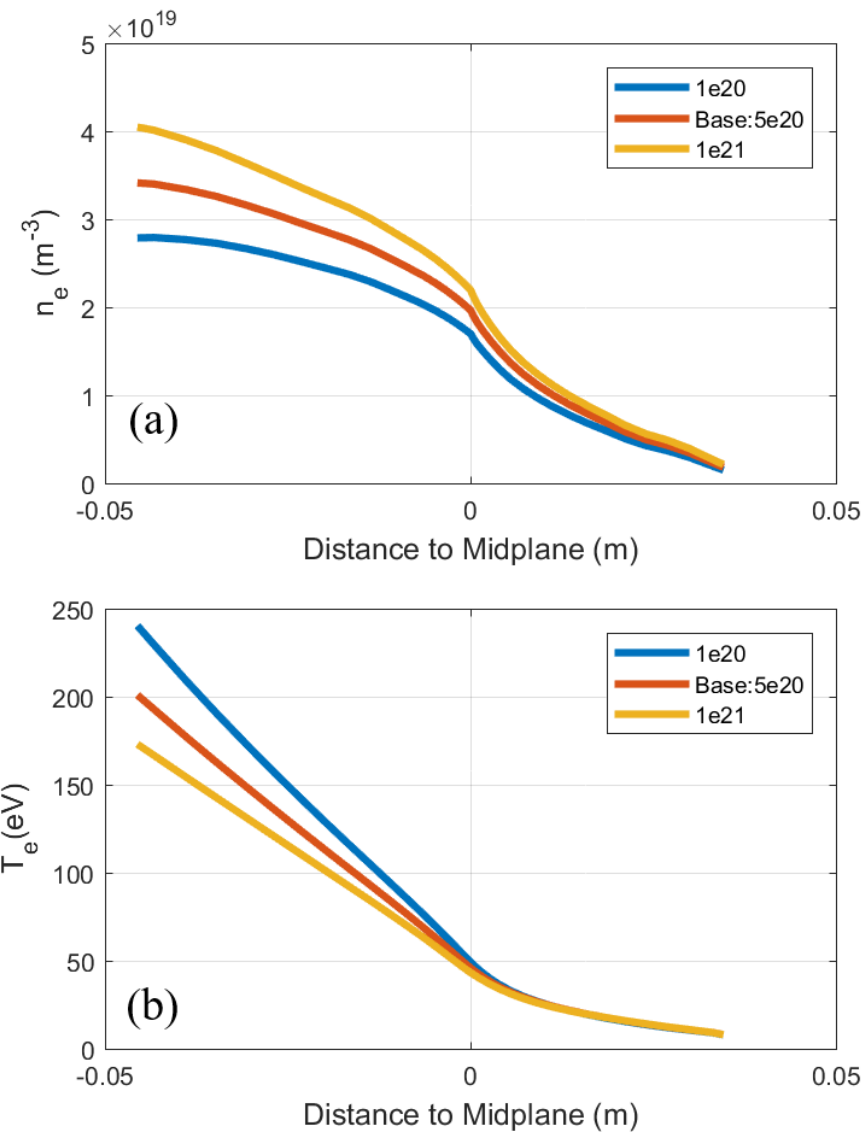
Figure 6.19 Outer mid-plane profiles with different particle flux across the core boundary, (a) electron density n_e profiles, (b) electron temperature T_e profiles.

The particle flux Γ_{ion} and electron temperature T_e profiles at inner and outer targets are shown in Figure 6.20, the differences of particle fluxes are within ~5% which means the detached inner target is not sensitive to the particle flux across the core boundary. Even with different value of particle flux across the core boundary, the modelling results of particle flux is still lower than the experimental value. In the low particle flux case, the peak value of electron temperature at the outer target is ~10 eV near strike point ($\Delta S \sim 5cm$). In the high particle flux case, the peak value is ~8 eV in the far SOL region ($\Delta S \sim 15cm$). The volume electron density in Figure 6.21 presents the differences within 30%.
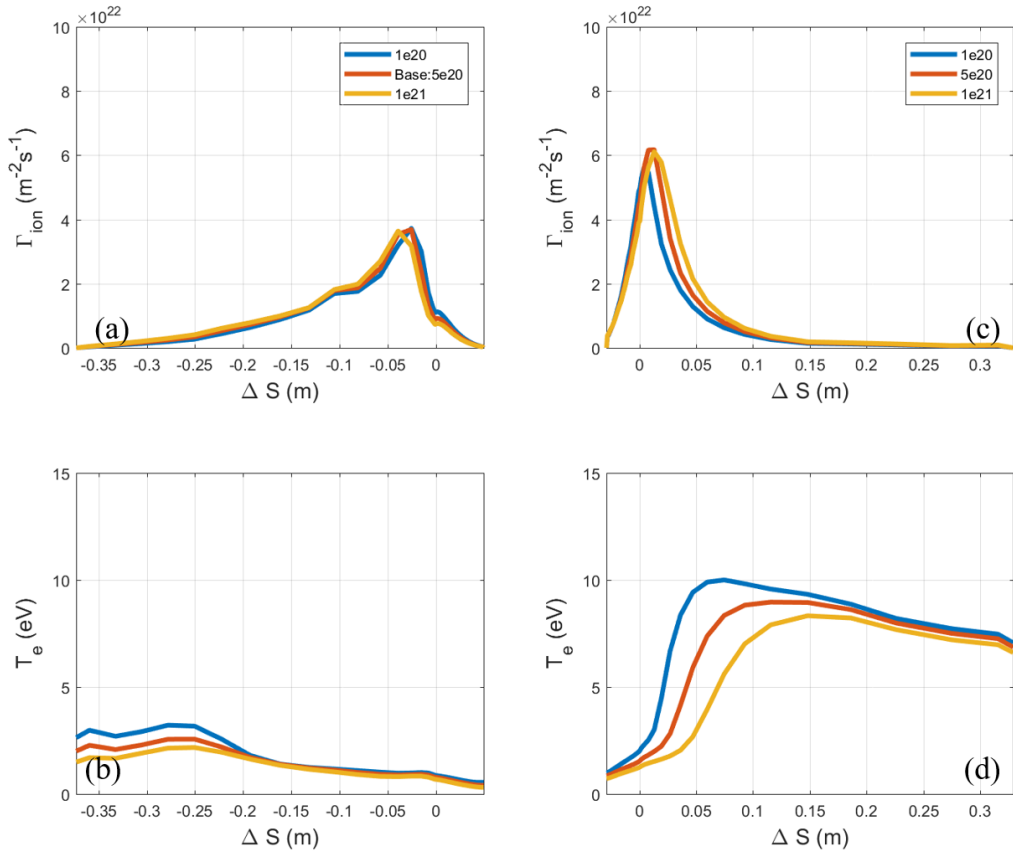
Figure 6.20 Targets profiles with different particle flux across the core boundary. (a) Particle flux profiles Γ_{ion} at the inner target, (b) electron temperature T_e profiles at the inner target, (c) particle flux Γ_{ion} profiles at the outer target, (d) electron temperature T_e at the outer target.
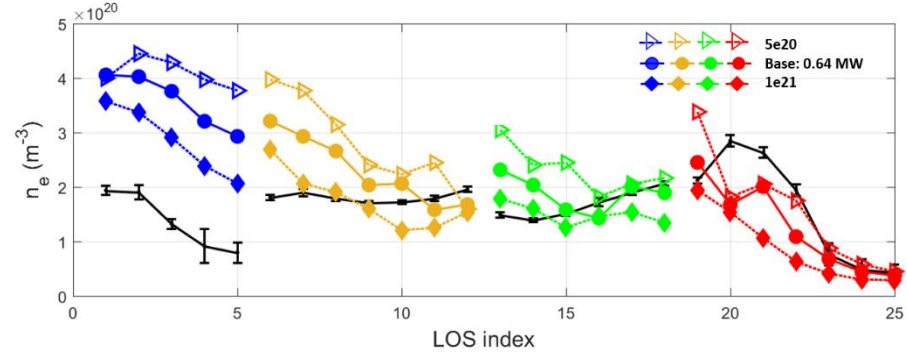
Figure 6.21 Modelled and measured electron densities n_e along line of sight with different particle flux across the core boundary.

6.4.3 Leakage boundary conditions

In this study, the drift-compatible leakage boundary conditions at wall boundary are used with a leakage factor α of 0.01 for particle, ion energy and electron energy. We consider them separately and another two values of leakage factor (0.05, 0.02) are considered.
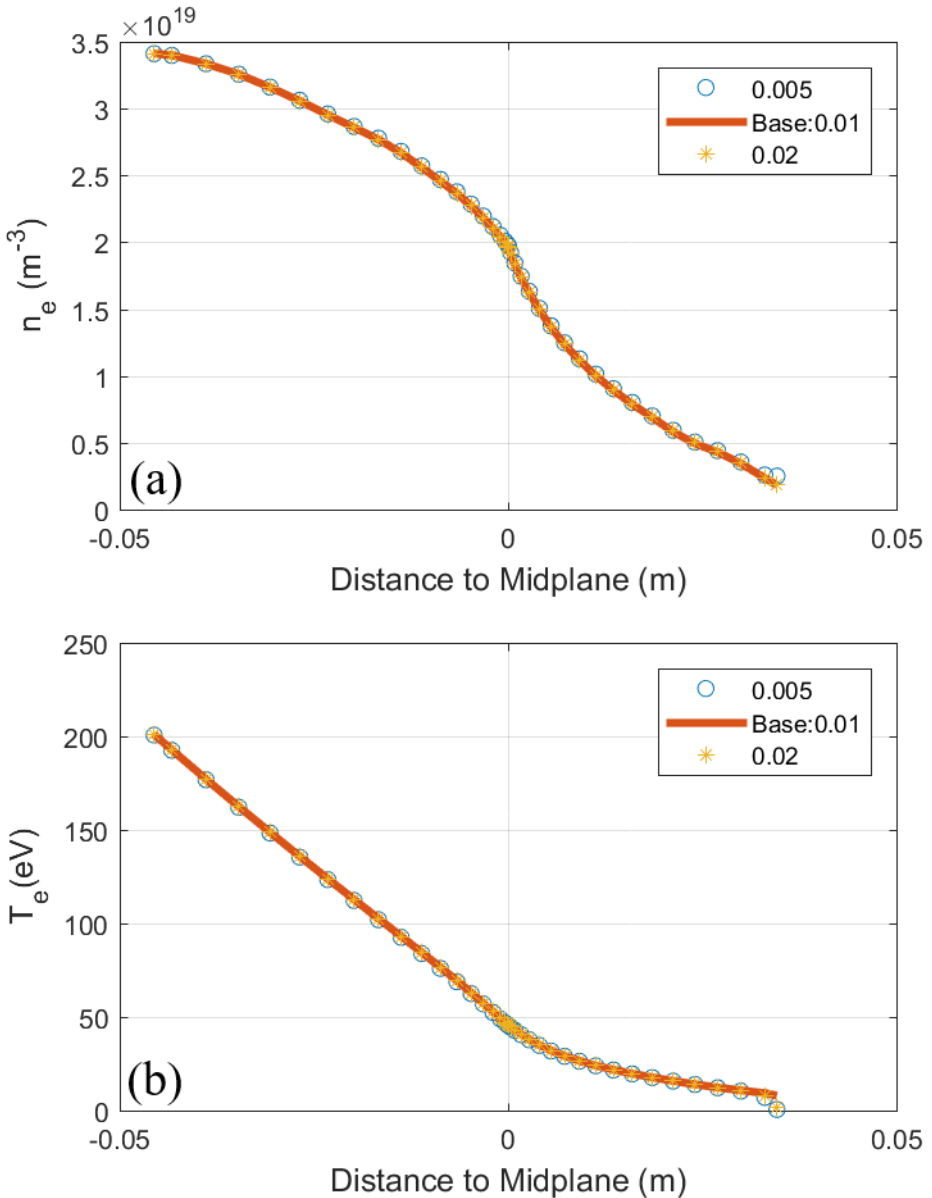
Figure 6.22 Outer mid-plane profiles with different leakage factors of particle boundary condition at wall boundary, (a) electron density n_e profiles at the outer mid-plane, (b) electron temperature T_e profiles at the outer mid-plane.

Figure 6.22 shows the electron dentsity n_e and electron temperature T_e profiles at the outer mid-plane with different values of leakage factor about particle boundary condition at wall boundary. It can be seen that even with different leakage factors, the outer mid-plane profiles are almost the same. For inner and outer targets profiles, the situations are similar: the particle flux Γ_{ion} and electron temperature T_e profiles are almost coincident as shown in Figure 6.23.

For the ion and electron energy leakage boundary conditions at the wall boundary, similar numerical test is performed. The electron density n_e and electron temperature T_e profiles at the outer mid-plane are shown in Figure 6.24, and the particle flux Γ_{ion} and electron temperature T_e profiles at the inner and outer targets are shown in Figure 6.25. Even with different leakage factors, both the outer mid-

plane and targets profiles are almost same. Thus, we belive that compared to input power and particle flux through the core boundary, the particle and ion and electron energy leakge factors are less important.
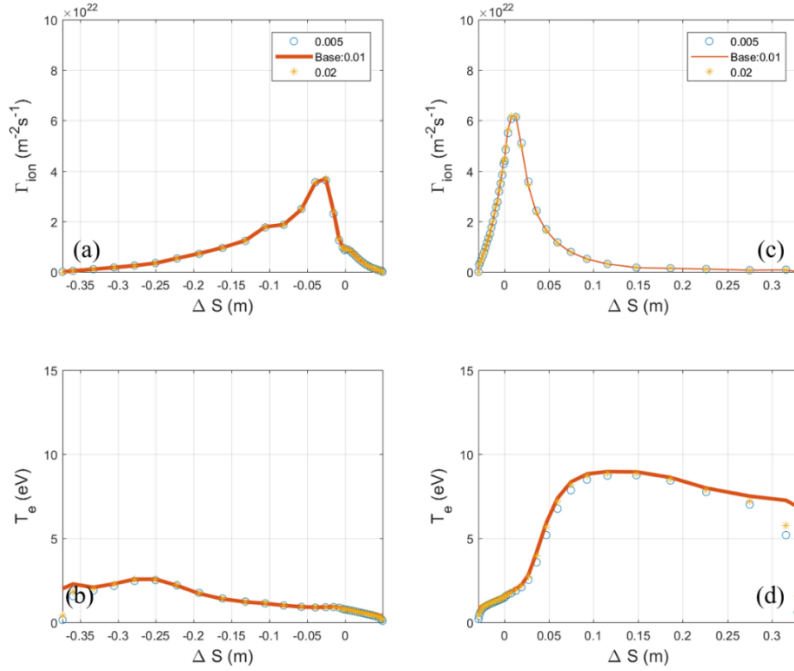
Figure 6.23 Targets profiles with different leakage factors of particle boundary condition at wall boundary (a) Particle flux Γ_{ion} profiles at the inner target, (b) electron temperature T_e profiles at the inner target, (c) particle flux Γ_{ion} profiles at the outer target, (d) electron temperature T_e at the outer target.
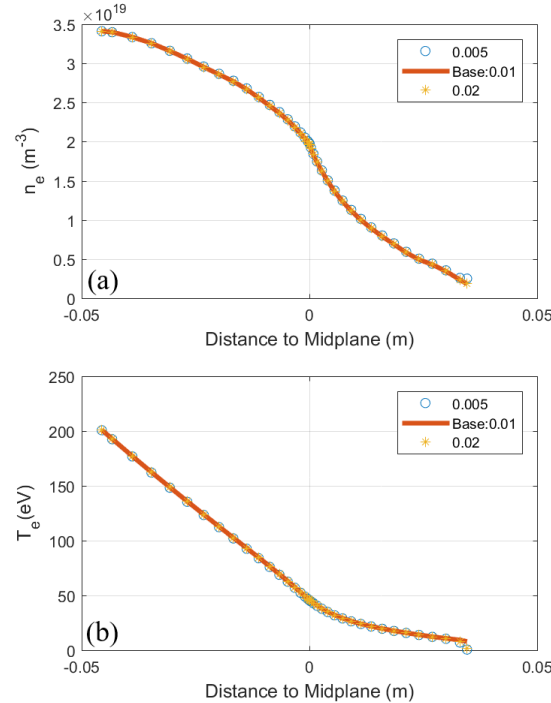
Figure 6.24 Outer mid-plane profiles with different leakage factors of ion&electron boundary conditions at wall boundary, (a) electron density n_e profiles at the outer mid-plane, (b) electron temperature T_e profiles at the outer mid-plane.
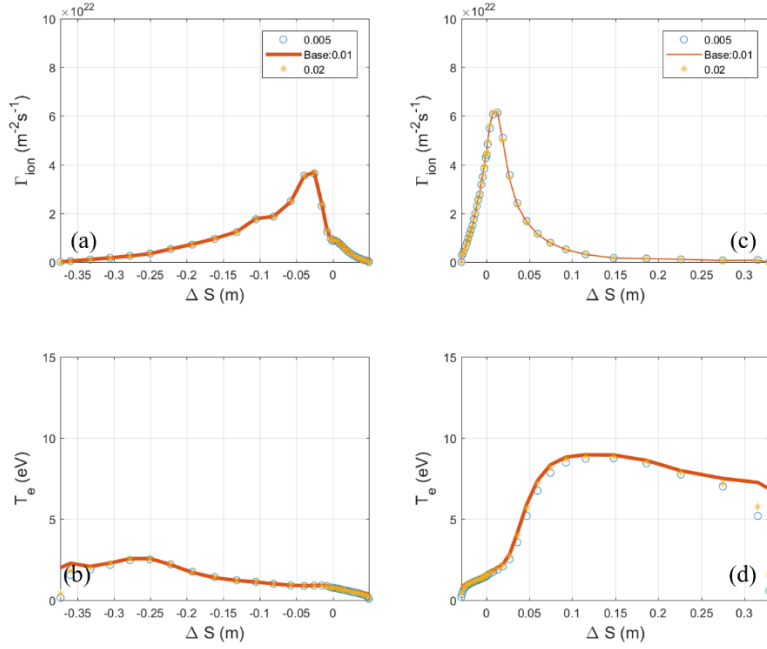
Figure 6.25 Targets profiles with different leakage factors of ion&electron boundary conditions at wall boundary. (a) Particle flux Γ_{ion} profiles at the inner target, (b) electron temperature T_e profiles at the inner target, (c) particle flux Γ_{ion} profiles at the outer target, (d) electron temperature T_e profiles at the outer target.

In this chapter, different valude of boundary conditions are performed. Even with different value of boundary conditions, the discrepancy of particle flux at outer target in the fluctuating detachment state between simulation and experiments still exist. And also the discrepency about volume electron density measured by RIV group of divertor spectroscopy.

Chapter 7

Conclusions and perspectives

The divertor is an important part of a fusion reactor, located at the bottom of the plasma chamber. It controls the exhaust of heat and helium ashes, and protects the core plasma from impurity contamination. Transport along the open magnetic field lines in the SOL is unimpeded, leading to the concentrated deposition of large power over relatively small areas. Since from the engineering point of view there is a limit of a few MW/m^2 on the peak steady-state heat load on the divertor, the divertor target heat load becomes a critical issue for tokamak reactor devices. It has been found that in the divertor detachment regime, the divertor target heat load are significantly decreased.

The SOLPS code package has been widely used for studying edge plasma physics, especially detachment. More recently, the ITER Organization started developing, distributing, and maintaining SOLPS-ITER as the state-of-the-art numerical tool for edge plasma modelling. In order to be confident about SOLPS-ITER predictive modelling results, we validate SOLPS-ITER against ASDEX Upgrage L-mode detachment discharges experimental data.

We firstly compare SOLPS-ITER simulation results with SOLPS5.0 without considering the effect of drifts. This is because SOLPS5.0 has been used for ASDEX Upgrade modelling more than twenty years. For kinetic neutral model, in fixed gas-puff mode, there is ~20% difference in the n_e and T_e target profiles. We trace these discrepancies mostly to the different ion energy sources provided by different versions of EIRENE. In the feedback-controlled mode, with the same n_{sep} the differences of targets profiles are reduced to ~10%.

Then SOLPS-ITER is used to model ASDEX Upgrade L-mode discharge detachment states including the onset of detachment, the fluctuating detachment state and the complete detachment. The convective transport by filaments is mimicked through a radial convective velocity in the low field side. Through adjusting the perpendicular transport coefficients, the outer mid-plane profiles match well the experimental measurements. The large discrepancy of particle flux at inner target between modelling results and experimental data in previous SOLPS5.0 study [63] is reduced. For the electron density at inner divertor volume, which is associated with the HFSHD region, the modeled value also match well with experimental data. A parameter scan of radial convective velocity shows that as the velocity descreases, the inner divertor electron density near inner target decreases and qualitatively matches the experimental data. The current discrepancy between SOLPS-ITER modelling results and experimental data is the peak value of particle flux at outer divertor target. In the onset of detachment state, the measured

value is higher than modelling results by a factor ~2. In fluctuating detachment state, the measured value is higher than modelling results by a factor ~3. In the complete detachment state, there is no such discrepancies. We also explored the effect of drifts, radial convective transport to outer mid-plane and targets profiles. The influence of different boundary conditions is also presented.

In this study, only the deuterium fuelling is considered. In the future, SOLPS-ITER modelling of ASDEX upgrade impurity seeded L-mode discharge need to be studied, because impurities have an important influence on the divertor power exhaust problem. In this study, only the standard atomic reactions are considered. The effect of neutral-neutral collisions needs to be considered in SOLPS-ITER modelling. The EU-DEMO is considered to be the last step before a commercial fusion power plant and is now in the conceptual design phase. In the future, the SOLPS-ITER physical model will be used to predict the detachment scenario of the EU-DEMO.

References

[1] F.F. Chen, Introduction To Plasma Physics and Controlled Fusion, New York: Plenum press, **1984**.

[2] G.Miley, Fusion cross sections and reactivities, No. COO-2218-17. Illinois Univ., Urbana (USA), **1974**.

[3] Goldston, et al, Introduction to plasma physics. CRC Press, **1995**.

[4] J.D. Lawson, Some criteria for a power producing thermonuclear reactor, *Proc. Phys.Soc.*, B70, **1957**.

[5] J.Wesson, et al., Tokamaks 4th, Vol. 149. Oxford university press, **2011**.

[6] P.C. Stangeby, The plasma boundary of magnetic fusion devices, CRC Press, **2000**.

[7] H.Meyer, et al., Overview of physics studies on ASDEX Upgrade, *Nuclear fusion* 59.11 (**2019**): 112014.

[8] Jet Team, Fusion energy production from a deuterium-tritium plasma in the JET tokamak, *Nuclear Fusion* 32.2 (**1992**): 187.

[9] R.A.Pitts, et al., The design of central column protection tiles for the TCV tokamak, *Nucl. Fusion* 39 1433 (**1999**)

[10] J.L.Luxon, et al., Overview of the DIII-D fusion science program, *Fusion Science and Technology* 48.2 (**2005**): 807-827.

[11] H.P. Shirai, et al, Recent progress of the JT-60SA project, *Nuclear Fusion* 57.10 (**2017**): 102002.

[12] J. Li, et al., Recent progress on EAST, *Fusion Science and Technology* 64.3 (**2013**): 417-423.

[13] Q. Li, The component development status of HL-2M tokamak, *Fusion Engineering and Design* 96 (**2015**): 338-342.

[14] K.Ikeda, Progress in the ITER physics basis, *Nuclear Fusion* 47.6 (**2007**).

[15] Y.Wan, et al.，Overview of the present progress and activities on the CFETR, *Nuclear Fusion* 57.10 (**2017**): 102009.

[16] R.Albanese, et al., DTT: a divertor tokamak test facility for the study of the power exhaust issues in view of DEMO, *Nuclear Fusion* 57.1 (**2016**): 016010.

[17] G.Federici, et al., Overview of EU DEMO design and R&D activities, *Fusion Engineering and Design* 89.7-8 (**2014**): 882-889.

[18] R.A. Pitts, Tokamak edge physics and plasma-surface interactions, Hungarian Plasma Physics and Fusion Technology Workshop, **2012**

[19] A. Kallenbach, The ASDEX Upgrade tokamak (**2016**).

[20] F.Wagner, et al., Regime of improved confinement and high beta in neutral-beam-heated divertor discharges of the ASDEX tokamak, *Physical Review Letters* 49.19 (**1982**): 1408.

[21] M. Shimada, et al., Overview and summary, *Nuclear Fusion* 47.6 (**2007**): S1.

[22] K. H. Burrell, Effects of E×B velocity shear and magnetic shear on turbulence and transport in magnetic confinement devices, Physics of Plasmas, 4.5(**1997**):1499–1518.

[23] A. Loarte, et al. *Nuclear Fusion*, 47.6(**2007**):S203–S263.

[24] Y. Ueda, Status of Plasma Facing Material Studies and Issues toward DEMO, *Plasma and Fusion Research*, 5(**2010**):S1009–S1009.

[25] V.S. Chan, V. S., et al., Evaluation of CFETR as a fusion nuclear science facility using multiple system codes, *Nuclear Fusion* 55.2 (**2015**): 023017.

[26] R. Chodura, et al., Physics of Plasma-wall interactions in controlled fusion, New York Plenum Press, **1986**.

[27] R. Schneider, et al., Plasma edge physics with B2-eirene, *Contributions to Plasma Physics* 46.1-2 (**2006**): 3-191.

[28] A. Zito, Simulating the impact of perpendicular scrape-off layer transporton momentum and power dissipationin magnetic fusion devices, Master thesis, **2019**

[29] W.Eckstein, Physical sputtering and reflection processes in plasma-wall interactions, *Journal of Nuclear Materials* 248 (**1997**): 1-8.

[30] A.Kirschner, Erosion and deposition mechanisms in fusion plasmas, *Fusion science and technology* 53.2T (**2008**): 259-277.

[31] J., Wolfgang and J. Roth, Chemical sputtering: *Sputtering by particle bombardment*. Springer, Berlin, Heidelberg, **2007**. 329-400.

[32] F. Reimold, Experimental Studies and Modeling of Divertor Plasma Detachment in H-Mode Discharges in the ASDEX Upgrade Tokamak, Phd thesis, **2015**.

[33] B. Lipschultz, et al., Divertor physics research on Alcator C-Mod, *Fusion science and technology*, 51.3(**2007**):369–389.

[34] A. Loarte, et al., Plasma detachment in JET Mark I divertor experiments, *Nucl. Fusion* 38.3(**1998**)38 331.

[35] S. Potzel, et al., A new experimental classification of divertor detachment in ASDEX Upgrade, *Nuclear Fusion* 54(**2013**):013001.

[36] A. Kallenbach, Arne, et al., Partial detachment of high power discharges in ASDEX Upgrade, *Nuclear Fusion* 55.5 (**2015**): 053026.

[37] F. Reimold, F., et al., Divertor studies in nitrogen induced completely detached H-modes in full tungsten ASDEX Upgrade, *Nuclear Fusion* 55.3 (**2015**): 033004.

[38] S.Potzel, et al., Electron density determination in the divertor volume of ASDEX Upgrade via Stark broadening of the Balmer lines, *Plasma Physics and Controlled Fusion* 56.2 (**2014**): 025010.

[39] S. Potzel, et al., Formation of the high density front in the inner far SOL at ASDEX Upgrade and JET, J*ournal of Nuclear Materials* 463 (**2015**): 541-545.

[40] P.Manz, et al., Stability and propagation of the high field side high density front in the fluctuating state of detachment in ASDEX Upgrade, *Nuclear Materials and Energy* 12 (**2017**): 1152-1156.

[41] S.I. Krasheninnikov, et al., Stability of the detachment front in a tokamak divertor, *Journal of nuclear materials* 266 (**1999**): 251-257.

[42] F.Reimold, et al., The high field side high density region in SOLPS-modeling of nitrogen-seeded H-modes in ASDEX Upgrade *Nuclear Materials and Energy* 12 (**2017**): 193-199.

[43] D. Bohm. In A. Guthrie R. K. Wakerling, editor, The characteristics of electrical discharges in magnetic fields, McGraw-Hill New York, **1949**.

[44] M. Wischmeier, Simulating divertor detachment in the TCV and JET tokamaks, Ph.D thesis (**2004**).

[45] B. LaBombard, et al., Cross-field plasma transport and main-chamber recycling in diverted plasmas on Alcator C-Mod, *Nucl. Fusion*, 40.12(**2000**) 2041.

[46] J.A.Boedo, et al., Transport by intermittent convection in the boundary of the DIII-D tokamak, *Physics of Plasmas* 8.11 (**2001**): 4826-4833.

[47] D.A. D'ippolito,et al., Convective transport by intermittent blob-filaments: Comparison of theory and experiment, *Physics of Plasmas* 18.6 (**2011**): 060501.

[48] M. Kocan, et al., Intermittent transport across the scrape-off layer: latest results from ASDEX Upgrade, *Nuclear Fusion* 53 (**2013**).

[49] O.E. Garcia, et al., Turbulence and intermittent transport at the boundary of magnetized plasmas, *Physics of plasmas* 12.6 (**2005**): 062309.

[50] D. Carralero, et al., Recent progress towards a quantitative description of filamentary SOL transport, *Nuclear Fusion* 57.5 (**2017**): 056044.

[51] G. Birkenmeier, et al., Filament transport, warm ions and erosion in ASDEX Upgrade L-modes, *Nuclear Fusion* 55.3 (**2015**): 033018.

[52] D. Carralero, et al., Implications of high density operation on SOL transport: A multimachine investigation, *Journal of Nuclear Materials* 463 (**2015**): 123-127.

[53] P. Manz, et al., The diffusion limit of ballistic transport in the scrape-off layer, *Physics of Plasmas* 27.2 (**2020**): 022506.

[54] B.J. Braams, A multi-fluid code for simulation of the edge plasma in tokamaks. NET Report 68 (**1987**).

[55] B.J. Braams, Radiative divertor modelling for ITER and TPX, *Contribution Plasma Phys.* 36 (**1996**):276-281.

[56] V.Rozhansky, et al., Simulation of tokamak edge plasma including self-consistent electric fields *Nuclear Fusion* 41.4 (**2001**): 387.

[57] D.Reiter, The EIRENE Code User Manual, **2019**.

[58] X.Bonnin, et al., Code development for ITER edge modelling–SOLPS5. 1, *Journal of Nuclear Materials* 390 (**2009**): 274-277.

[59] W. Dekeyser, X. Bonnin, R. Pitts, General Introduction to SOLPS-ITER, SOLPS-ITER release workshop, **2015**.

[60] M. Wischmeier, et al., The influence of molecular dynamics on divertor detachment in TCV, *Contributions to Plasma Physics* 44.1-3 (**2004**): 268-273.

[61] D.P. Coster, et al., Simulation of the edge plasma in tokamaks，*Physica Scripta* T108 (**2004**): 7.

[62] A.V. Chankin, et al., Simulation of ASDEX Upgrade Ohmic plasmas for SOLPS code validation, *Nuclear fusion* 49.1 (**2008**): 015004.

[63] L. Aho-Mantila, et al, Assessment of SOLPS5. 0 divertor solutions with drifts and currents against L-mode experiments in ASDEX Upgrade and JET, *Plasma Physics and Controlled Fusion* 59.3 (**2017**): 035003.

[64] F. Reimold, M. Wischmeier, S. Potzel, L. Guimarais, D. Reiter,M. Bernert,M. Dunne, T. Lunt, Nuclear Materials and Energy **2017**, 12, 193.

[65] V. Kotov, et al., Numerical study of the ITER divertor plasma with the B2-EIRENE code package (**2007**).

[66] V. Kotov, et al, Numerical modelling of high density JET divertor plasma with the SOLPS4. 2 (B2-EIRENE) code, *Plasma physics and controlled fusion* 50.10 (**2008**): 105012.

[67] A.S. Kukushkin, et al., Consequences of a reduction of the upstream power SOL width in ITER, *Journal of Nuclear Materials* 438 (**2013**): S203-S207.

[68] A.S. Kukushkin, et al., Finalizing the ITER divertor design: the key role of SOLPS modeling, *Fusion engineering and design* 86.12 (**2011**): 2865-2873.

[69] S. Wiesen, Sven, et al., The new SOLPS-ITER code package, *Journal of nuclear materials* 463 (**2015**): 480-484.

[70] X/ Bonnin, Xavier, et al., Presentation of the new SOLPS-ITER code package for tokamak plasma edge modelling, *Plasma and Fusion Research* 11 (**2016**): 1403102-1403102.

[71] V.Rozhansky, et al., New B2SOLPS5. 2 transport code for H-mode regimes in tokamaks, *Nuclear fusion* 49.2 (**2009**): 025007.

[72] E. Sytova, E., et al., Impact of a new general form of friction and thermal forces on SOLPS-ITER modelling results, *Contributions to Plasma Physics* 58.6-8 (**2018**): 622-628.

[73] L. Aho-Mantila, et al., Outer divertor of ASDEX Upgrade in low-density L-mode discharges in forward and reversed magnetic field: I. Comparison between measured plasma conditions and SOLPS5. 0 code calculations, *Nuclear Fusion* 52.10 (**2012**): 103006.

[74] L. Aho-Mantila, Leena, et al., Outer divertor of ASDEX Upgrade in low-density L-mode discharges in forward and reversed magnetic field: II. Analysis of local impurity migration, *Nuclear Fusion* 52.10 (2012): 103007.

[75] L. Aho-Mantila, et al., L-mode radiative plasma edge studies for model validation in ASDEX Upgrade and JET, Journal of Nuclear Materials 438 (**2013**): S321-S325.

[76] A. Kallenbach, A., et al., Divertor power load feedback with nitrogen seeding in ASDEX Upgrade, *Plasma Physics and Controlled Fusion* 52.5 (**2010**): 055002.

[77] G. Meisl, et al., Nitrogen retention in ASDEX Upgrade, *Journal of Nuclear Materials* 463 (**2015**): 668-671.

[78] M. Wensing, et al., SOLPS-ITER simulations of the TCV divertor upgrade, *Plasma Physics and Controlled Fusion* 61.8 (b): 085029.

[79] W. Dekeyser, et al., SOLPS-ITER Study of neutral leakage and drift effects on the alcator C-Mod divertor plasma, *Nuclear Materials and Energy* 12 (**2017**): 899-907.

[80] E.T.Meier, et al., Analysis of drift effects on the tokamak power scrape-off width using SOLPS-ITER, *Plasma Physics and Controlled Fusion* 58.12 (**2016**): 125012.

[81] E.Sytova, et al., Comparing N versus Ne as divertor radiators in ASDEX-upgrade and ITER, *Nuclear Materials and Energy* 19 (**2019**): 72-78.

[82] O. Pan, et al., SOLPS-ITER modeling with activated drifts for a snowflake divertor in ASDEX Upgrade, *Plasma Physics and Controlled Fusion* 62.4 (**2020**): 045005.

[83] P. Pan, et al., SOLPS simulations of detachment in a snowflake configuration for the future upper divertor in ASDEX Upgrade, *Plasma Physics and Controlled Fusion* 60.8 (**2018**): 085005.

[84] I.P. Pérez, et al., Impact of drifts in the ASDEX upgrade upper open divertor using SOLPS-ITER, *Contributions to Plasma Physics* (**2020**).

[85] C. Cao, et al., Predictive modeling of HL-2M divertor operation by SOLPS-ITER, *Fusion Engineering and Design* 136 (**2018**): 822-827.

[86] S.I. Braginskii, Transport processes in a plasma, *Reviews of plasma physics* 1 (**1965**).

[87] R.Balescu, Transport processes in plasmas (**1988**).

[88] ML Zhao, Towards a More Complete Description of Tokamak Edge Plasmas:SOLPS Simulations with Kinetic Electron Effects, Phd thesis, **2018**.

[89] W. Fundamenski, Parallel heat flux limits in the tokamak scrape-off layer, *Plasma physics and controlled fusion* 47.11 (**2005**): R163.

[90] N. Horsten, et al., Hybrid fluid-kinetic model for neutral particles in the plasma edge, *Nuclear Materials and Energy* 18 (**2019**): 201-207.

[91] M. Blommaert, et al., A spatially hybrid fluid-kinetic neutral model for SOLPS-ITER plasma edge simulations, *Nuclear Materials and Energy* 19 (**2019**): 28-33.

[92] M. Baelmans. Code improvements and applications of a two-dimensional edge plasma model for toroidal fusion devices. PhD. thesis, **1993**.

[93] SOLPS-ITER user manual, **2019**.

[94] Y. Feng, et al., Recent Improvements in the EMC3-Eirene Code, *Contributions to Plasma Physics* 54.4-6 (**2014**): 426-431.

[95] J. Rapp, et al, Transport simulations of linear plasma generators with the B2. 5-Eirene and EMC3-Eirene codes, *Journal of Nuclear Materials* 463 (**2015**): 510-514.

[96] D.Harting, et al., Validating the 3D edge code EMC3-EIRENE against 2D simulations with EDGE2D-EIRENE for JET single null configurations, *Journal of nuclear materials* 415.1 (**2011**): S540-S544.

[97] C. Guillemaut, et al., Influence of atomic physics on EDGE2D-EIRENE simulations of JET divertor detachment with carbon and beryllium/tungsten plasma-facing components, *Nuclear fusion* 54.9 (**2014**): 093012.

[98] G. Ciraolo, et al., H-mode WEST tungsten divertor operation: deuterium and nitrogen seeded simulations with SOLEDGE2D-EIRENE, *Nuclear Materials and Energy* 12 (**2017**): 187-192.

[99] J.F. Kaiser, On a simple algorithm to calculate the'energy'of a signal, International conference on acoustics, speech, and signal processing. IEEE, (**1990**).

[100]   S. Wiesen, et al., SOLPS Development for ITER [100]: Upgrading from SOLPS4 to SOLPS5, ITER report (**2013**).

[101]   H. Murmann, et al., The Thomson scattering systems of the ASDEX Upgrade tokamak, *Rev. Sci. Instrum*. 63(**1992**).

[102]   S. Wolfgang, Practical Limitations to Plasma Edge Electron Temperature Measurements by Radiometry of Electron Cyclotron Emission, **1996**.

[103]   IPP internal website.

[104]   S. K. Rathgeber, et al., Review on global migration, fuel retention and modelling after TEXTOR decommission, *EPS 2013*, Helsinki, Sweden.

[105]   R. Fischer, et al., Integrated data analysis of profile diagnostics at ASDEX Upgrade, *Fusion science and technology* 58.2 (**2010**): 675-684.

[106]   S.K. Rathgeber, et al., Estimation of profiles of the effective ion charge at ASDEX Upgrade with Integrated Data Analysis, *Plasma Physics and Controlled Fusion* 52.9 (2010): 095008.

[107]   M. Weinlich and A. Carlson, Introduction to measurements with Langmuir probes, **1998**.

[108]   S. Potzel, Experimental classification of divertor detachment, Phd thesis, **2012**.

[109]   A. Scarabosio, et al., Measurements of neutral gas fluxes under different plasma and divertor regimes in ASDEX Upgrade, *Journal of Nuclear Materials* 390(**2009**):494–497.

[110]   A. Scarabosio, et al., Nuclear Instruments and Methods in Physics Research Section A: Accelerators, Spectrometers, Detectors and Associated Equipment, 623(2):667-671, November **2010**.

[111] X. Bonnin, el al., SOLPS-ITER Physics/numerics model switches: 5.0 vs 5.2, SOLPS-ITER 3rd User Forum (**2015**).

[112]   D. Reiter, New features in EIRENE, SOLPS-ITER workshop (**2015**).

[113]   H.Wu, et al., Comparison of SOLPS5. 0 and SOLPS-ITER simulations for ASDEX upgrade L-mode, *Contributions to Plasma Physics* (**2020**).

[114]   V. Kotov, Numerical modelling of high density JET divertor plasma with the SOLPS4. 2 (B2-EIRENE) code, *Plasma physics and controlled fusion* 50.10 (**2008**): 105012.

[115]   W. Eckstein, et al., Data sets for hydrogen reflection and their use in neutral transport calculations, **1986**.

[116]   G. Bateman, Distribution of neutrals scattered off a wall. Applied Physics Division Physics Report 1. Princeton Univ., NJ (USA). Plasma Physics Lab., **1980**.

[117]   B. Streibl, et al., In-vessel cryo pump for ASDEX Upgrade divertor, *Fusion Technology* 1996, Elsevier, Oxford, **1997**, pp. 427–430.

[118]   M. Baelmans, et al., B2-B2.5 Code Benchmarking Part II: Incorporating Parallel Electrical Currents, **2014**.

[119]   D.P. Coster, Simulation of the edge plasma in tokamaks, *Physica Scripta* 2004.T108 (**2004**): 7.

[120]   A.V. Chankin, et al., Influence of the $E \times B$ drift in high recycling divertors on target asymmetries, *Plasma Physics and Controlled Fusion* 57.9 (**2015**): 095002.

[121]   Coster, D. P., private communication **2018**.

[122]   E. Kaveeva, et al., Speed-up of SOLPS-ITER code for tokamak edge modeling, *Nuclear Fusion* 58.12 (**2018**): 126018.

[123]   S. Voskoboynikov, How to switch on drifts in SOLPS-ITER, SOLPS-ITER workshop (**2015**)

[124]   D. Carralero, et al., On the role of filaments in perpendicular heat transport at the scrape-off layer, *Nuclear Fusion* 58.9 (**2018**): 096015.